A MULTISCALE MODEL FOR PREDICTING DAMAGE EVOLUTION IN HETEROGENEOUS VISCOELASTIC MEDIA

A Dissertation

by

CHAD RANDALL SEARCY

Submitted to the Office of Graduate Studies of
Texas A&M University
in partial fulfillment of the requirements for the degree of

DOCTOR OF PHILOSOPHY

August 2004

Major Subject: Aerospace Engineering

A MULTISCALE MODEL FOR PREDICTING DAMAGE EVOLUTION IN HETEROGENEOUS VISCOELASTIC MEDIA

A Dissertation

by

CHAD RANDALL SEARCY

Submitted to Texas A&M University
in partial fulfillment of the requirements
for the degree of

DOCTOR OF PHILOSOPHY

Approved as to style and content by:

David H. Allen (Chair of Committee)	Vikram K. Kinra (Member)
Dimitris C. Lagoudas (Member)	John C. Slattery (Member)
Jay R. Walton (Member)	Walter E. Haisler (Head of Department)

August 2004

Major Subject: Aerospace Engineering

ABSTRACT

A Multiscale Model for Predicting Damage Evolution in
Heterogeneous Viscoelastic Media. (August 2004)
Chad Randall Searcy, B.S., Baylor University;
M.S., Texas A&M University
Chair of Advisory Committee: Dr. David H. Allen

A multiple scale theory is developed for the prediction of damage evolution in heterogeneous viscoelastic media. Asymptotic expansions of the field variables are used to derive a global scale viscoelastic constitutive equation that includes the effects of local scale damage. Damage, in the form discrete cracks, is allowed to grow according to a micromechanically-based viscoelastic traction-displacement law. Finite element formulations have been developed for both the global and local scale problems. These formulations have been implemented into a two-scale computational model Numerical results are given for several example problems in order to demonstrate the effectiveness of the technique.

To my family, whom I love very much

ACKNOWLEDGEMENTS

I would like to express my sincere gratitude to Dr. David Allen, chair of my graduate advisory committee, for his personal commitment to me and to this project. Dr. Allen's guidance and mentorship are most appreciated. I also wish to thank the members of my graduate advisory committee: Dr. Vikram Kinra, Dr. Dimitris Lagoudas, Dr. John Slattery, and Dr. Jay Walton for their assistance in critiquing this work. They have all contributed greatly to the final form of this work. My appreciation goes to Dr. Mike Arnold for serving as my Graduate Council Representative. I would like to acknowledge the financial support provided by Dr. George Gazonas and the Army Research Office. Special thanks are due to my colleagues Dr. Curtis Berthelot, Dr. Kayleen Helms, and Dr. Jah Noe for their friendship and shared knowledge. Very special thanks are due to my devoted friends and co-workers: Ms. Lisa Biggs, Dr. Pavlin Enchev, Mr. Olivier Godard, Mr. Todd Griffith, Mr. Bjoern Kiefer, Ms. Misty Moon, Mr. James Morrow III, Mr. Peter Popov, Mr. Gary Don Seidel, Mr. Matt Wilkins, Ms. Elizabeth Zapata, for their technical assistance and personal encouragement throughout this effort.

TABLE OF CONTENTS

LIST OF TABLES

TABLE Page

LIST OF FIGURES

FIGURE Page

FIGURE Page

1. INTRODUCTION

Composite materials have become increasingly useful in the construction of many aerospace, mechanical, and civil engineering structures. These materials provide optimal structural-scale properties that the individual constituents cannot provide alone. Since the design and manufacture of composites are often costly in both time and material resources, evaluation methods are needed to predict the future performance of newly proposed materials. Ideally these methods would be capable of modeling every geometric feature and constitutive type within the entire composite structure. Unfortunately, for a proposed composite structure composed of thousands of microscale constituents this ideal places an unreasonable demand on the technology currently available to design engineers. Although significant advances have been made in the areas of analytical theory, experimental testing, and computational methods, attempts to produce such a comprehensive model have come with several inherent limitations:

1) Many closed-form analytical solutions exist for linear elastic composites which exhibit simple, periodic, internal geometries. However, the ability to produce a closed-form solution diminishes greatly when one tries to incorporate inelastic constitutive behavior; irregularly-shaped, randomly-oriented inclusions; and growing internal boundaries.
2) Traditional phenomenological models can provide thorough predictive capabilities for composite systems which exhibit a particular set of constitutive and morphological characteristics. However, too often these models are not general enough to be applied to other composite systems which display a difference in their set of geometric and constitutive characteristics.
3) Computational models, such as the finite element method, have been shown to be extremely versatile in addressing issues such as inelastic constitutive

---

The format of this dissertation follows that of the Journal of the Mechanics and Physics of Solids.

behavior; irregularly-shaped, randomly-oriented inclusions; and growing internal boundaries. However, a composite structure that contains thousands of irregularly-shaped, randomly-oriented inclusions along with thousands of potential crack sites would require a highly refined finite element mesh with possibly tens of millions of degrees of freedom. The solution to such a problem would be extraordinarily time-consuming, if not completely unfeasible, given the state of the computational resources currently available.

Faced with these limitations in modeling, researchers are currently seeking alternative approaches which can retain as much information as possible regarding the composite microstructure without having to model every geometric feature within the composite structure. One such approach, which has been receiving increasing attention from the mechanics community, is that of multiple-scale, or multiscale, modeling. With this approach, a separate continuum-scale analysis is performed at each of the smaller structural scales within the macroscopic body. If statistical homogeneity at any smaller length scale has been satisfied, a homogenization principle may be used to produce the constitutive equations to be used at the next larger length scale. Damage, in the form of discrete cracks, can be modeled explicitly at any length scale by incorporating a type of fracture mechanics model to the analysis. More specifically, models of this type can exhibit several important features:

1) When implemented into a finite element algorithm, multiscale models have few limitations on the number of constituents, the number of constituent types, and the types of geometry that can be modeled within a given composite.
2) Finite element algorithms can offer a high resolution of the geometric details within a well defined representative volume of the larger scale structure.
3) The initiation and growth of multiple cracks at the local scale can be modeled by incorporating an appropriate cohesive zone model into the multiscale finite element algorithm.

4) Multiscale methods can account for the material anisotropy that develops at the global scale due to the damage that develops at the local scale.
5) Although some information, such as smaller-scale stress concentrations, will be averaged out during the homogenization process, multiscale methods can provide a numerically efficient method for modeling multiscale problems.
6) Multiscale models can minimize the need for extensive laboratory experimentation and field investigations since the model will rely strictly upon the fundamental structural properties of each of the constituents.

Although multiscale models do not model every geometric detail within a composite structure, from the above list of features it can be seen that if placed within a finite element context, multiscale methods can still offer high fidelity in modeling composites which exhibit a hierarchical structure. Moreover, if the multiscale analysis is properly administered, any sacrifice in accuracy introduced by the separation of the analyses at different length scales will be negligible. Most importantly, the multiscale method can overcome the computational obstacles presented by other approaches that attempt to model all scales at once.

1.1 Literature Review

Multiscale models, like the method presented in this work, belong to a larger class of constitutive models known as homogenization theories. In general, all homogenization theories share one common objective: to predict the overall behavior of a composite material based on the material behavior and geometric arrangement of its constituents. Some homogenization techniques, like mean-field theories and variational bounding methods, have been a subject of study for decades and continue to inspire new areas of research today. These classical homogenization theories are well described in the works by Christensen (1979), Nemat-Nasser and Hori (1993), and Mura (1987). Other techniques, like asymptotic homogenization, have only recently reached maturity as a subject of study.

Asymptotic homogenization theory was born out of the applied mathematics field in the 1970s and is often referred to as *mathematical homogenization theory*. This theory models the behavior of heterogeneous media made up of infinite periodic arrangements of constituents under the action of far field mechanical loads. A large disparity must exist between the sizes of the global scale structure and the smallest repeatable local scale structure called a *unit cell*. This disparity allows for the expansion of the field variables using asymptotic series, which leads to the separation of the local scale analysis from the global scale analysis. The global scale field variables are often linked to the local scale field variables by a homogenized constitutive relationship. Early forays into asymptotic homogenization focused primarily on linear elastic constitutive relationships. Among the more notable contributions made during this developmental period are the works by Bensoussan, et al., (1978) and Sanchez-Palencia (1980). Later, these techniques were extended to a variety of inelastic media including nonlinear elasticity (Jansson, 1992), plasticity (Suquet, 1987; Fish, et al., 1997), and viscoelasticity (Chung, et al., 2000, Maghous and Creus, 2003; Nadot-Martin, et al., 2002; Yi, et al., 1998; Yu and Fish, 2002).

Jansson (1992) used asymptotic homogenization techniques to study the effective properties of a high volume fraction fiber reinforced metal matrix composites. His investigation explores the influence of both square and hexagonal fiber arrays. Jansson develops his theory and then uses a numerical approach to solve for the stress and strain fields at the local scale. He concludes that the nonlinear transverse and in-plane shear strains for these composites are strongly influenced by the fiber arrangement.

Maghous and Creus expand on some of the work presented in Allen and Yoon (1998). Their main contribution is the incorporation of aging effects which become manifest through the localization tensors. This work uses asymptotic expansions as a means of determining homogenized properties for the Kelvin-Voigt viscoelastic analogue. Strong emphasis is placed on the dissipative corrector that arises from the derivation of the homogenized equations in the time domain. The dissipative corrector relates long-term relaxation to instantaneous viscoelastic behavior. By neglecting this dissipative corrector, uniqueness in the micro-level behavior is not ensured. This method finds a closed form solution for the global scale constitutive equations via a stress concentration factor.

Therefore the finite element procedure is only for global scale analyses; however, local scale effects have been considered in the form of the global constitutive equations.

Yi, et al. (1998) perform a standard asymptotic analysis on a viscoelastic composite. No growing internal boundaries are considered. To achieve an expression for the homogenized viscoelastic properties, they solve the local scale boundary value problem by taking a Carson transform approach. From their analysis they produce an expression for the viscoelastic memory effect. An interesting observation from this work is that if the local relaxation modulus is separable in space and time, then the memory effects do not show up in the homogenized properties. Also, memory effects can be introduced due to the spatial and temporal variation in the viscoelastic moduli. An isotropic viscoelastic medium containing many voids, will not exhibit memory effects. Consequently, media which are comprised of elastic inclusions embedded within a viscoelastic matrix will exhibit memory effects. However, if the stiffness of the inclusions is much larger than that of the viscoelastic matrix, then memory effects are negligible.

Yu and Fish (2002) use double asymptotic expansions in both time and space as a means of determining homogenized properties for a viscoelastic Kelvin-Voigt model. Their temporal expansion is designed to address inertial effects. The authors' model makes use of a dissipative corrector that develops from the derivation of the homogenized equations in the time domain. With this method, Yu and Fish show that the homogenization process in space and time can be obtained by solving a first order initial value problem, as opposed to solving a local boundary value problem over the a unit cell.

Of particular interest to us are several recent works that address the particle-matrix interfaces in term of cohesive surfaces. In the work reported by Lene and Leguillon (1982), a homogenization method is developed for elastic composites, which considers damage in terms of tangential slip at the fiber-matrix interface. A linear elastic cohesive law was used to govern the slip phenomenon. Damage in the form of decohesion was not considered at this time; however Lene (1986) later expands on this work to include damage caused by fiber-matrix debonding for linear elastic composites. A finite element approach was used to determine the necessary strain concentration factors. From their analysis, Lene and Leguillon were able to establish upper and lower bounds on the effect of damage.

These bounds are independent of the fiber-matrix volume fractions and directly related to the elastic modulus of the fiber and of the cohesive layer. In a similar manner, Nadot-Martin et al. (2002) developed a homogenization technique for linear viscoelastic composites with a granulated microstructure. Their work is an extension of the method proposed by Christoffersen (1983) for elastic bonded granulates. In their model, the granulated microstructure is represented by Voronoi polyhedra which are bonded together by cohesive interfaces. The grains are linear elastic in nature while the cohesive interfaces are linear viscoelastic. Interfacial damage in terms of grain/matrix decohesion is not studied in this work; however, this aspect of damage will be presented in a companion paper which is currently in preparation (Nadot-Martin et al, 2003). The authors make significant efforts to craft a macroscale constitutive law that carefully considers all aspects of the local microstructure. Despite these efforts, Nadot-Martin et al. deem the model to be too complex (effectively there are as many macroscopic internal variables as there are viscoelastic interfaces within the representative volume). As an alternative the researchers propose a simplified version of their model (by averaging all interface effects into one internal variable).

In a similar manner, Carrere, et al. (2003) developed a technique that employs: 1) Tvergaard's model (1990) for the interfacial behavior between the fibres and matrix; and 2) a modified version of Dvorak's Transformation Field Analysis model, which is used to predict the nonlinear behavior of unidirectional metal matrix composites. The model incorporates micromechanics, coupling viscoplasticity, damage, and thermal effects. Basically, Dvorak (1992) expanded on classical macroscopic relations for elastic media so that inelasticity can be incorporated. To incorporate damage and thermal effects, they employ a theory from Chaboche et al. (2001) where a generalized eigenstrain accounts for these effects. The strain localization tensor for the representative volume is evaluated only once using the finite element method.

Numerical methods, like the finite element method, play an essential role in multiscale modeling. In fact many researchers have explored the fundamental aspects of finite element code construction for multiscale problems. Among the more notable contributions in this area are the works by Fish and co-workers (Fish and Wagiman, 1993;

Fish and Belsky, 1995; Fish and Shek, 2000). These papers provide strategic approaches regarding: the approximation of the global and local scale displacement fields; the solution method for both global and local scale problems; and information transfer between the scales.

Detailed multiscaling strategies have also been advanced by Feyel and Chaboche. Feyel (1999) outlines what he calls a multilevel finite element (or FE^2) approach. In this approach, constitutive equations are only written on the local scale. Homogenization and localization relationships are used to calculate the global scale strains and stresses based on the local scale problem. Implementation of the FE^2 model is based on the nesting of finite element algorithms. Each Gaussian integration point in the global scale finite element mesh requires a separate local scale finite element computation. Feyel takes advantage of parallel processing to expedite the calculation of all the local scale analyses for a given time step. Feyel and Chaboche (2000) apply this method to the study of long fiber SiC/Ti composites, where interfacial debonding in modeled by Tvergaard's cohesive zone model.

In a series of papers presented by Ghosh and co-workers (Lee, et al., 1999; Ghosh, et al. 2001; Raghavan, et al. 2001) an adaptive multi-level methodology is developed that utilizes computational sub-domains of varying resolution. The Voronoi cell finite element model is used to analyze the microstructural scale, while conventional displacement based finite element methods are used to perform the macroscale analysis. Because of the periodicity assumptions inherent to the theory, asymptotic homogenization techniques have difficulties with the accurate modeling of regions on the global scale which exhibit large stress gradients. To remedy this problem, an adaptive portion of the computational model is used to evaluate "hotspot" regions where localized damage causes a rise in the global stress gradient.

Also in the realm of adaptive finite element modeling, Oden and co-workers developed the Homgenized Dirichlet Projection Method (Oden, et al., 1999; Oden and Zohdi, 1997). This method employs a multiscale approach as an adaptive method for refining finite element solutions of acknowledged highly heterogeneous elastic structures. First, an auxiliary homogenized boundary value problem is solved at the global scale. Next, an *a posteriori* error estimate of the solution is made to the auxiliary problem. For those regions which have an unacceptable error level, a local boundary value problem is constructed by projecting homogenized displacements upon the selected subregion. The local boundary value problem for these subregions are solved for the exact microstructure with the approximate local boundary conditions. Further partitioning and solving of local boundary value problems will continue until the error is below the preselected value. This method is said to be orders of magnitude cheaper than direct large-scale simulations of micromechanical events. Oden admits that there is error introduced by approximating the local boundary data. Also, the local boundary conditions are sensitive to the homogenized material properties used in the global problem. He assumes that the exact topology and mechanical properties of the microstructure are a priori known exactly. Oden uses a multiple scale expansion to register the local perturbations in the global field variables. In so doing, he replaces the fine-scale boundary values on the local subdomain boundaties by smoother kinematically admissible function

1.2 Research Objective

The objective of this work is to develop a two-scale model to address the mechanical response of heterogeneous viscoelastic structures with growing local scale cracks. The development of this model will require a specific plan of action, a summary of which is outlined below.

1) We will derive a two-scale constitutive equation that relates the local scale responses to the global scale.

To assist us in the derivation of this constitutive equation, we will employ an approach known as *asymptotic homogenization*. By choosing this type of approach we are assuming that the representative microstructure of our medium is spatially periodic at the local scale. In the end, this periodic microstructure assumption may be too restrictive for the modeling of composites possessing spatially non-periodic microstructures. For cases where it is necessary, we will outline how we can relax this criterion and still preserve the integrity of the two-scale method we derive.

2) We will recast the two-scale constitutive equation into a form amenable to the finite element formulation.

While this incrementalized version of the multiscale constitutive equation will be placed into a finite element formulation for the global scale problem, a similar finite element formulation will be constructed for the local scale problem. Together, these formulations will be used to construct a two-scale finite element program designed for the calculation of stresses and strains in heterogeneous viscoelastic structures with growing local scale cracks.

3) We will demonstrate the effectiveness of the two-scale model through the evaluation of several example problems.

These example problems are designed to not only show several aspects to the two scale model including elasticity and fully cohesive internal boundaries, as special cases.

As with any model; asymptotic homogenization has its advantages and disadvantages. One attractive feature to such an approach is that the mathematical architecture associated with the homogenization of periodic structures allows us to track all the independent variables in a multiscale problem. This type of analysis also allows us to use a detailed description of the local scale structure, which is particularly useful for the study of local scale damage initiation. However, because crack growth is confined to the unit cell, this technique is not well suited for investigating phenomena such as crack coalescence which leads to the formation of global scale cracks. One drawback is that asymptotic homogenization techniques tend to be computationally expensive. Imposing periodic boundary conditions can require large amounts of computing time and memory allocation. Multipoint constraints used to implement periodic boundary conditions tend to degrade the band structure of the local stiffness matrix.

1.3 Layout of Dissertation

Section 1 introduces the background, objective, and methodology of this research. Section 2 shows the development the field equations associated with the initial boundary value problem for a generalized two-scale viscoelastic medium with moving internal boundaries at the local scale. Section 3 demonstrates the incrementalization of the multiscale constitutive equations developed in Section 2. Section 4 features the finite element formulations for both the global and local scale problems which lead to the construction of the multiscale finite element program. Section 5 illustrates the effectiveness of this method through the presentation of several example problems. Section 6 presents the summary, conclusions, and limitations of this research, as well as potential future research that will extend the findings presented herein.

2. GENERALIZED MULTISCALE PROBLEM DESCRIPTION

In this section we outline the development of our two-scale model. The works reported by Lene and Leguillon (1982) and Jansson (1992) have been influential in the development of this method. Starting from first principles, we develop a homogenization method based on the asymptotic expansion of the field variables of interest. Our derivation ultimately leads to a nonlinear viscoelastic constitutive equation for the global scale that is dependent on the movement and growth of internal boundaries at the local scale. Throughout this section, we will address important issues regarding the underlying theory of asymptotic expansions and homogenization. As with any new theory, new notational conventions will be introduced, and we will carefully address the meaning and context of these notational conventions.

2.1 Single Scale Approach

Consider the inhomogeneous viscoelastic body X depicted in Figure 2.1. This global-scale body consists of at least two distinct constituents and features growing internal boundaries. Body X is endowed with a three-dimensional orthonormal basis from which the position of each material point $\mathbf{x}$ may be expressed. The set of material points which define the external boundary ∂X consists of two separate and distinct subsets: ∂X_u, which defines that portion of the external boundary where displacements $\hat{u}_i\left(\mathbf{x},\, t\right)$ are applied; and ∂X_T, which defines that portion of the external boundary where tractions $\hat{T}_i\left(\mathbf{x},\, t\right)$ are applied. The circumflex notation indicates that these quantities are known *a priori*. No intersection exists between these two subsets, and their union defines the external boundary of the global body, ∂X. The global-scale body possesses a periodic local scale structure formed by a tessellation by the smallest repeatable volume known as the *unit cell*. The characteristic length-scale associated with this unit cell ℓ is much smaller than the length-scale associated with the global body L, so that

$$\delta = \frac{\ell}{L} \ll 1 \tag{2.1}$$

where δ is called the *scaling ratio* between the two length-scales.

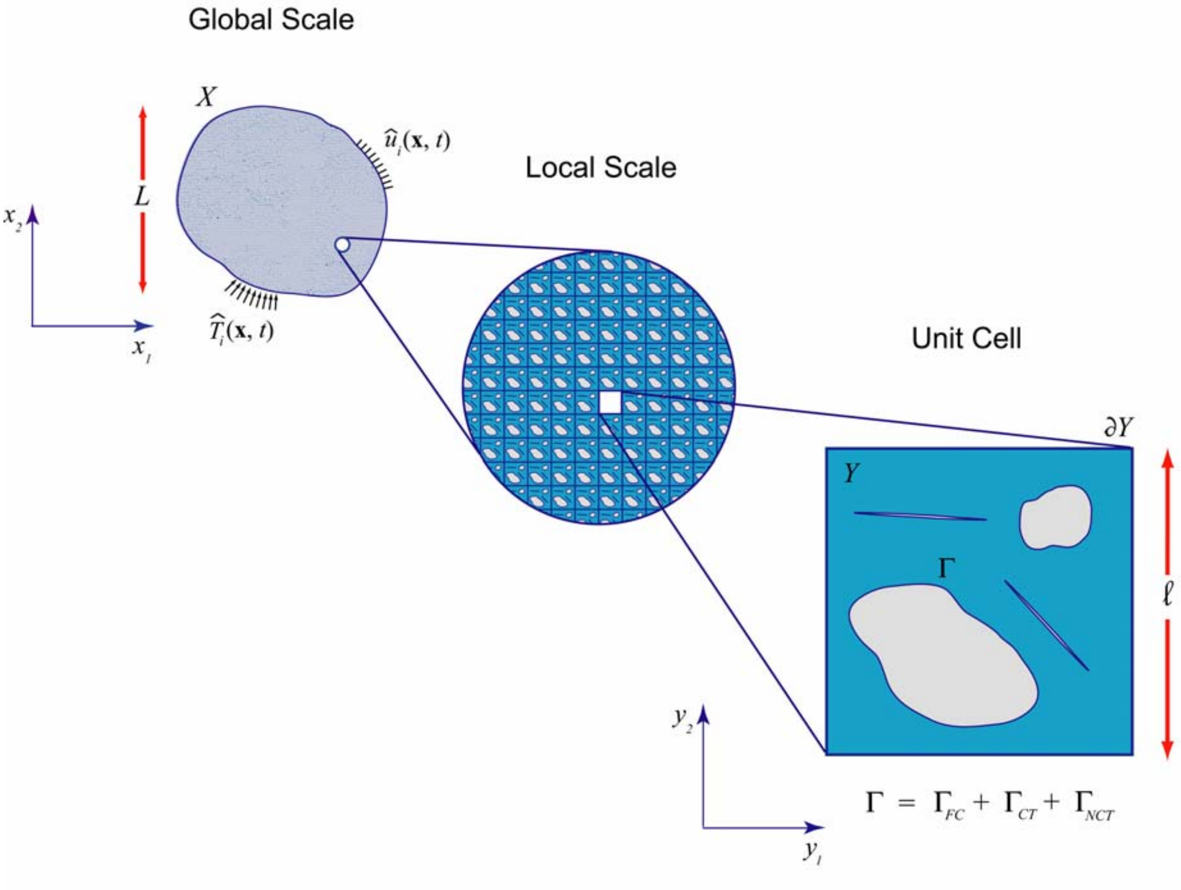

Figure 2.1 Global, Local, and Unit Cell Geometries.

A generalized representation of a unit cell is shown Figure 2.1. This unit cell consists of an interior Y, an external boundary ∂Y, and a set of internal boundaries Γ. Within the unit cell there exists a spatial distribution of randomly-oriented, irregularly-shaped inclusions. Each of the unit cell's constituents is endowed with its own set of viscoelastic material properties. Because of the spatial distribution of the constituents, as well as the distribution of the growing internal boundaries, the viscoelastic relaxation moduli for the unit cell $C_{ijkl}(\mathbf{y}, t)$ are functions of the local position $\mathbf{y}$ and time t. The set of material points which define the internal boundaries of the unit cell is comprised of three subsets: Γ_{FC}, which denotes the set of fully cohesive boundaries that exist between two separate constituents; Γ_{CT}, which denotes the internal crack faces upon which damage-dependent cohesive tractions are applied; and Γ_{NCT}, denotes the internal crack faces upon which no cohesive tractions are applied. No intersection exists between these three subsets, and their union defines the internal boundary of the unit cell, Γ. In general, both Γ_{CT} and Γ_{NCT} are time dependent quantities.

The relationship between the global coordinate system $\mathbf{x}$ and the local coordinate system for the unit cell $\mathbf{y}$ can be written as

$$\mathbf{y} = \frac{\mathbf{x}}{\delta}. \tag{2.2}$$

At this point we will pose the initial boundary value problem for the entire body. The variables of state for this analysis are the displacement vector $u_i^{\delta}(\mathbf{x}, t)$, the linearized strain tensor $\varepsilon_{ij}^{\delta}(\mathbf{x}, t)$, and the Cauchy stress tensor $\sigma_{ij}^{\delta}(\mathbf{x}, t)$. The superscript δ emphasizes that the corresponding field variables are periodic in the local coordinate.

In the absence of global body forces and inertial effects, the conservation of linear momentum may be expressed by

$$\frac{\partial \sigma_{ji}^{\delta}(\mathbf{x}, t)}{\partial x_j} = 0 \qquad \text{in } X. \tag{2.3}$$

In our analysis, displacement gradients are considered to be small; thus, a linearized form of the global strain tensor may be permitted

$$\varepsilon_{ij}^{\delta}\left(\mathbf{u}^{\delta}(\mathbf{x}, t)\right) = \frac{1}{2}\left(\frac{\partial u_i^{\delta}(\mathbf{x}, t)}{\partial x_j} + \frac{\partial u_j^{\delta}(\mathbf{x}, t)}{\partial x_i}\right) \qquad \text{on } X. \tag{2.4}$$

The linear viscoelastic behavior of the constituents may be represented by the convolution-type single integral equation

$$\sigma_{ij}^{\delta}(\mathbf{x},t)=\int_{0}^{t} C_{ijkl}^{\delta}\left(\mathbf{x},\ t-\tau\right)\frac{\partial\varepsilon_{kl}^{\delta}\left(\mathbf{u}^{\delta}(\mathbf{x},\tau)\right)}{\partial\tau}\ \mathrm{d}\tau \qquad \text{on } X \qquad (2.5)$$

where $C_{ijkl}^{\delta}\left(\mathbf{x},\ t\right)$ is the relaxation modulus tensor. The stress $\sigma_{ij}^{\delta}(\mathbf{x},t)$ in (2.5) is dependent upon the entire history of the strain $\varepsilon_{ij}^{\delta}(\mathbf{x},t)$.

A rate-dependent traction-displacement law may be used to model the opening and extension of cracks. This behavior may be expressed by the traction-displacement relationship developed by Allen and Searcy (2001a)

$$\sigma_{ij}^{\delta}\left(\mathbf{x},t\right)n_j=\frac{\left[u_j^{\delta}\left(\mathbf{x},t\right)\right]}{\lambda\left(\mathbf{x},t\right)}\left(1-\alpha\left(\mathbf{x},t\right)\right)\int_{0}^{t}E^{cz}(\mathbf{x},t-\tau)\frac{\partial\lambda\left(\mathbf{x},\tau\right)}{\partial\tau}\mathrm{d}\tau \qquad \text{on } \Gamma_{CT}^{\delta} \qquad (2.6)$$

where

$$\lambda\left(\mathbf{x},t\right)=\left(\left(\frac{\left[u_1^{\delta}(\mathbf{x},t)\right]}{\delta_1}\right)^2+\left(\frac{\left[u_2^{\delta}(\mathbf{x},t)\right]}{\delta_2}\right)^2+\left(\frac{\left[u_3^{\delta}(\mathbf{x},t)\right]}{\delta_3}\right)^2\right)^{1/2}. \qquad (2.7)$$

The brackets $[\bullet]$ indicate the jump of a function across opposing crack faces. Variables $\lambda\left(\mathbf{x},t\right)$, $\alpha\left(\mathbf{x},t\right)$, $E^{cz}(\mathbf{x},t)$, δ_1, δ_2, and δ_3 are parameters associated with the rate-dependent cohesive zone model that is outlined in Appendix A.

Tractions and displacements are specified on the external boundary of the global body. These mixed boundary conditions are:

$$\sigma_{ij}^{\delta}(\mathbf{x},t)n_j=\hat{T}_i\left(\mathbf{x},t\right) \qquad \text{on } \partial X_T \qquad (2.8)$$

$$u_i^{\delta}\left(\mathbf{x},t\right)=\hat{u}_i\left(\mathbf{x},t\right) \qquad \text{on } \partial X_u \tag{2.9}$$

where $\hat{T}_i\left(\mathbf{x},t\right)$ and $\hat{u}_i\left(\mathbf{x},t\right)$ are the specified boundary tractions and boundary displacements, respectively.

The initial values for all the state variables are assumed to be zero.

With equations (2.3) through (2.9), the above boundary value problem is considered to be well-posed.

Because of the spatially oscillating material properties, it would be difficult to solve this global scale boundary value problem using conventional methods. Therefore, we must rely on another methodology in order to capture the effects of the rapidly varying material properties.

2.2 Asymptotic Expansion Approach

Let us assume the displacement field may be expressed in terms of an asymptotic expansion of the form

$$u_i^{\delta}\left(\mathbf{x},\,t\right)=u_i^0\left(\mathbf{x},\mathbf{y},t\right)+\delta u_i^1\left(\mathbf{x},\mathbf{y},t\right)+\delta^2 u_i^2\left(\mathbf{x},\mathbf{y},t\right)+\,\cdots \tag{2.10}$$

where each of the individual expansion terms $u_i^a\left(\mathbf{x},\mathbf{y},t\right)$ are functions of the two spatial variables ($\mathbf{x}$ and $\mathbf{y}$) and time (t). The displacement field is considered to be periodic in the local coordinate $\mathbf{y}$, i.e.

$$u_i^a\left(\mathbf{x},\mathbf{y},t\right)=u_i^a\left(\mathbf{x},\mathbf{y}+\mathbf{d},\,t\right) \qquad \text{for } \; a=0,1,\,2,\ldots \tag{2.11}$$

where $\mathbf{d}$ is the vector of periodicity for the local microstructure.

Because of the coexistence of the two scales, spatial derivatives must be expanded via the chain-rule to account for the effects of the two length scales. Thus, for any field variable $g^{\delta}(\mathbf{x},\, t)$, the spatial derivative may be expressed in the following manner

$$\frac{\partial g^{\delta}(\mathbf{x},\, t)}{\partial x_j} = \frac{\partial g(\mathbf{x},\mathbf{y},\, t)}{\partial x_j} + \frac{1}{\delta}\frac{\partial g(\mathbf{x},\mathbf{y},\, t)}{\partial y_j}\,. \tag{2.12}$$

Consequently, by applying (2.12) to (2.10) we achieve the following asymptotic expansion for the linearized strain tensor

$$\begin{aligned}\varepsilon_{ij}^{\delta}(\mathbf{x},t) &= \varepsilon_{ij}^{0}\left(\mathbf{u}^{0}(\mathbf{x},\mathbf{y},t)\right) + \frac{1}{\delta}e_{ij}^{0}\left(\mathbf{u}^{0}(\mathbf{x},\mathbf{y},t)\right)\\ &\quad + \delta\varepsilon_{ij}^{1}\left(\mathbf{u}^{1}(\mathbf{x},\mathbf{y},t)\right) + e_{ij}^{1}\left(\mathbf{u}^{1}(\mathbf{x},\mathbf{y},t)\right)\\ &\quad + \delta^{2}\varepsilon_{ij}^{2}\left(\mathbf{u}^{2}(\mathbf{x},\mathbf{y},t)\right) + \delta e_{ij}^{2}\left(\mathbf{u}^{2}(\mathbf{x},\mathbf{y},t)\right) + \cdots\end{aligned} \tag{2.13}$$

where

$$\varepsilon_{ij}^{a}\left(\mathbf{u}(\mathbf{x},\mathbf{y},t)\right) = \frac{1}{2}\left(\frac{\partial u_i^a(\mathbf{x},\mathbf{y},t)}{\partial x_j} + \frac{\partial u_j^a(\mathbf{x},\mathbf{y},t)}{\partial x_i}\right) \qquad \text{for} \quad a = 0, 1, 2, \ldots \tag{2.14}$$

are measures of the strain with respect to the global coordinate $\mathbf{x}$, while

$$e_{ij}^{a}\left(\mathbf{u}(\mathbf{x},\mathbf{y},t)\right) = \frac{1}{2}\left(\frac{\partial u_i^a(\mathbf{x},\mathbf{y},t)}{\partial y_j} + \frac{\partial u_j^a(\mathbf{x},\mathbf{y},t)}{\partial y_i}\right) \qquad \text{for} \quad a = 0, 1, 2, \ldots \tag{2.15}$$

are measures of the strain with respect to the local coordinate $\mathbf{y}$.

A corresponding asymptotic expansion for the stress tensor can be achieved by introducing the expression for the strain (2.13) into the viscoelastic constitutive relationship (2.5). A generalized expression for this expansion in the stress is

$$\begin{aligned}\sigma_{ij}^{\delta}\left(\mathbf{x},t\right)=\frac{1}{\delta}\sigma_{ij}^{0}&\left\{e_{kl}^{0}\left(\mathbf{u}^{0}\left(\mathbf{x},\mathbf{y},t\right)\right)\right\}\\ &+\ \sigma_{ij}^{1}\left\{\varepsilon_{kl}^{0}\left(\mathbf{u}^{0}\left(\mathbf{x},\mathbf{y},t\right)\right),\ e_{kl}^{1}\left(\mathbf{u}^{1}\left(\mathbf{x},\mathbf{y},t\right)\right)\right\}\\ &+\ \delta\sigma_{ij}^{2}\left\{\varepsilon_{kl}^{1}\left(\mathbf{u}^{1}\left(\mathbf{x},\mathbf{y},t\right)\right),\ e_{kl}^{2}\left(\mathbf{u}^{2}\left(\mathbf{x},\mathbf{y},t\right)\right)\right\}+\cdots\end{aligned}\tag{2.16}$$

where the brackets $\left\{\bullet\right\}$ emphasize that the stresses have a functional dependence on the strains. Each term in the expansion (2.16) can be expressed as a convolution-type constitutive relationship. For the first three terms of this expansion these constitutive relationships are

$$\sigma_{ij}^{0}\left(\mathbf{x},\mathbf{y},t\right)=\int_{0}^{t}C_{ijkl}\left(\mathbf{y},\ t-\tau\right)\frac{\partial e_{ij}^{0}\left(\mathbf{u}^{0}\left(\mathbf{x},\mathbf{y},\tau\right)\right)}{\partial\tau}\ \mathrm{d}\tau\tag{2.17}$$

$$\begin{aligned}\sigma_{ij}^{1}\left(\mathbf{x},\mathbf{y},t\right)&=\int_{0}^{t}C_{ijkl}\left(\mathbf{y},\ t-\tau\right)\frac{\partial \varepsilon_{ij}^{0}\left(\mathbf{u}^{0}\left(\mathbf{x},\mathbf{y},\tau\right)\right)}{\partial\tau}\ \mathrm{d}\tau\\ &+\int_{0}^{t}C_{ijkl}\left(\mathbf{y},\ t-\tau\right)\frac{\partial e_{ij}^{1}\left(\mathbf{u}^{1}\left(\mathbf{x},\mathbf{y},\tau\right)\right)}{\partial\tau}\ \mathrm{d}\tau\end{aligned}\tag{2.18}$$

and

$$\begin{aligned}\sigma_{ij}^{2}\left(\mathbf{x},\mathbf{y},t\right)&=\int_{0}^{t}C_{ijkl}\left(\mathbf{y},\ t-\tau\right)\frac{\partial \varepsilon_{ij}^{1}\left(\mathbf{u}^{1}\left(\mathbf{x},\mathbf{y},\tau\right)\right)}{\partial\tau}\ \mathrm{d}\tau\\ &+\int_{0}^{t}C_{ijkl}\left(\mathbf{y},\ t-\tau\right)\frac{\partial e_{ij}^{2}\left(\mathbf{u}^{2}\left(\mathbf{x},\mathbf{y},\tau\right)\right)}{\partial\tau}\ \mathrm{d}\tau\end{aligned}\tag{2.19}$$

By introducing our asymptotic expansion for the stress (2.16) into the conservation of linear momentum (2.3), we achieve the following

$$\begin{aligned}&\frac{1}{\delta}\frac{\partial\sigma_{ij}^{0}\left(\mathbf{x},\mathbf{y},t\right)}{\partial x_j}+\frac{1}{\delta^2}\frac{\partial\sigma_{ij}^{0}\left(\mathbf{x},\mathbf{y},t\right)}{\partial y_j}\ +\\ &\frac{\partial\sigma_{ij}^{1}\left(\mathbf{x},\mathbf{y},t\right)}{\partial x_j}+\frac{1}{\delta}\frac{\partial\sigma_{ij}^{1}\left(\mathbf{x},\mathbf{y},t\right)}{\partial y_j}\ +\\ &\delta\frac{\partial\sigma_{ij}^{2}\left(\mathbf{x},\mathbf{y},t\right)}{\partial x_j}+\frac{\partial\sigma_{ij}^{2}\left(\mathbf{x},\mathbf{y},t\right)}{\partial y_j}\ +\ \cdots\ =\ 0\,.\end{aligned}\tag{2.20}$$

At this point we choose to separate terms in (2.20) according to the order of their scaling ratio δ . This action leads to a series of expressions for the conservation of linear momentum**.**

The first three expressions in this series are

$$\mathrm{O}\left(\delta^{-2}\right)\qquad\frac{\partial\sigma_{ij}^{0}\left(\mathbf{x},\mathbf{y},t\right)}{\partial y_j}=0\tag{2.21}$$

$$\mathrm{O}\left(\delta^{-1}\right)\qquad\frac{\partial\sigma_{ij}^{1}\left(\mathbf{x},\mathbf{y},t\right)}{\partial y_j}+\frac{\partial\sigma_{ij}^{0}\left(\mathbf{x},\mathbf{y},t\right)}{\partial x_j}=0\tag{2.22}$$

$$\mathrm{O}\left(\delta^{0}\right)\qquad\frac{\partial\sigma_{ij}^{2}\left(\mathbf{x},\mathbf{y},t\right)}{\partial y_j}+\frac{\partial\sigma_{ij}^{1}\left(\mathbf{x},\mathbf{y},t\right)}{\partial x_j}=0\,.\tag{2.23}$$

Using equations (2.21), (2.22), and (2.23), we will now pose three separate initial boundary value problems. Each boundary value problem will correspond to a different order of the scaling ratio δ. The solutions to these boundary value problems will yield a two-scale constitutive equation for heterogeneous viscoelastic media with growing cracks.

With proper constitution and kinematics, equation (2.21) can be used to pose an initial boundary value problem for the order δ^{-2} . In this boundary value problem, the volume of interest is the unit cell. The equations associated with this boundary value problem are

$$\frac{\partial}{\partial y_j}\left(\int_0^t C_{ijkl}\left(\mathbf{y},\, t-\tau\right)\frac{\partial}{\partial \tau}\left(\frac{\partial u_k^0(\mathbf{x},\mathbf{y},\tau)}{\partial y_l}\right)\mathrm{d}\tau\right)=0 \qquad \text{in } Y \qquad (2.24)$$

$$u_i^0(\mathbf{x},\mathbf{y},t)=u_i^0(\mathbf{x},\mathbf{y}+\mathbf{d},\, t) \qquad \text{on } \partial Y \qquad (2.25)$$

$$\sigma_{ij}^0(\mathbf{x},\mathbf{y},t)\,n_j = -\sigma_{ij}^0(\mathbf{x},\mathbf{y}+\mathbf{d},t)\,n_j \qquad \text{on } \partial Y \qquad (2.26)$$

$$\sigma_{ij}^0\left(\mathbf{x},\mathbf{y},t\right)n_j = \frac{\left[u_j^0\left(\mathbf{x},\mathbf{y},t\right)\right]}{\lambda\left(\mathbf{x},\mathbf{y},t\right)}\left(1-\alpha\left(\mathbf{x},\mathbf{y},t\right)\right)\int_0^t E^{cz}(\mathbf{x},\mathbf{y},t-\tau)\frac{\partial\lambda\left(\mathbf{x},\mathbf{y},\tau\right)}{\partial\tau}\mathrm{d}\tau \qquad \text{on } \Gamma_{CT}\,. \qquad (2.27)$$

The initial values for all the state variables are assumed to be zero.

Equations (2.24) through (2.27) define the δ^{-2} order boundary value problem. However as Jansson (1992) observed, boundary value problems of this type are ill-posed. No boundary conditions or body-type forces are being imposed on the unit cell. As a result, no unique solution exists to this problem. A solution may be reached by allowing the leading term in the displacements to be strictly a function of the global coordinate and time, i.e $u_i^0 = u_i^0\left(\mathbf{x},t\right)$. It is worth noting that this solution prevents the possibility of a singularity in the strain (2.16). Consequently, the unit cell in this boundary value problem is free from any stress: $\sigma_i^0\left(\mathbf{x},\mathbf{y},t\right)=0$.

With proper constitutive and kinematic relationships, equation (2.22) can be used to pose an initial boundary value problem on the order δ^{-1} . In this boundary value problem, as with the last, the volume of interest is the unit cell. The equations associated with this boundary value problem are

$$\begin{aligned}&\frac{\partial}{\partial y_j}\left(\int_0^t C_{ijkl}\left(\mathbf{y},\ t-\tau\right)\frac{\partial}{\partial\tau}\left(\frac{\partial u_k^1(\mathbf{x},\mathbf{y},\tau)}{\partial y_l}\right)d\tau\right)\\&+\frac{\partial}{\partial y_j}\left(\int_0^t C_{ijkl}\left(\mathbf{y},\ t-\tau\right)\frac{\partial}{\partial\tau}\left(\frac{\partial u_k^0(\mathbf{x},\mathbf{y},\tau)}{\partial x_l}\right)d\tau\right)=0\qquad \text{in } Y \qquad (2.28)\end{aligned}$$

$$u_i^1(\mathbf{x},\mathbf{y},t)=u_i^1(\mathbf{x},\mathbf{y}+\mathbf{d},\,t)\qquad \text{on } \partial Y \qquad (2.29)$$

$$\sigma_{ij}^1(\mathbf{x},\mathbf{y},t)\,n_j=-\sigma_{ij}^1(\mathbf{x},\mathbf{y}+\mathbf{d},t)\,n_j\qquad \text{on } \partial Y \qquad (2.30)$$

$$\begin{aligned}&\sigma_{ij}^1\left(\mathbf{x},\mathbf{y},t\right)n_j=\\&\frac{\left[u_j^1\left(\mathbf{x},\mathbf{y},t\right)\right]}{\lambda\left(\mathbf{x},\mathbf{y},t\right)}\left(1-\alpha\left(\mathbf{x},\mathbf{y},t\right)\right)\int_0^t E^{cz}(\mathbf{x},\mathbf{y},t-\tau)\frac{\partial\lambda^1\left(\mathbf{x},\mathbf{y},\tau\right)}{\partial\tau}\mathrm{d}\tau\qquad \text{on } \Gamma_{CT} \qquad (2.31)\end{aligned}$$

Equations (2.28) through (2.31) define our local scale boundary value problem. Unlike its predecessor, this boundary value problem is well-posed. The unit cell receives its loads via the body forces represented by the second term in (2.28). We have chosen to solve this local scale boundary value problem numerically using the finite element method. After the local stress $\left(\sigma_{ij}^1(\mathbf{x},\mathbf{y},t)\right)$ and strain $\left(\varepsilon_{ij}^0(\mathbf{x},\mathbf{y},t)+e_{ij}^1(\mathbf{x},\mathbf{y},t)\right)$ fields have been calculated, the goal is to utilize volume averaging techniques to convey local scale information to the global scale problem.

For this homogenization process, we define the following mean operator $\langle\,\bullet\,\rangle$ on Y:

$$\langle\,\bullet\,\rangle\equiv\frac{1}{|\,Y\,|}\int_Y\bullet\ \mathrm{d}Y \qquad (2.32)$$

where the angle brackets indicate the action of taking the volume average of the enclosed quantity. A quantity that has been volume averaged no longer has a dependence on the local coordinate $\mathbf{y}$. To indicate that this quantity has been volume averaged, we will place a bar over the field variable. To illustrate these new notations, consider the volume average of the local stress $\sigma_{ij}^{1}\left(\mathbf{x},\mathbf{y},t\right)$, which may be expressed in one of the following ways:

$$\bar{\sigma}_{ij}^{1}\left(\mathbf{x},t\right)=\left\langle \sigma_{ij}^{1}\left(\mathbf{x},\mathbf{y},t\right)\right\rangle =\frac{1}{\left|Y\right|}\int_{Y}\sigma_{ij}^{1}\left(\mathbf{x},\mathbf{y},t\right)\mathrm{d}Y\,. \tag{2.33}$$

We can insert our constitutive relationship (2.18) into (2.33) to produce the volume averaged constitutive relationship

$$\bar{\sigma}_{ij}^{1}\left(\mathbf{x},t\right)=\left\langle \int_{0}^{t}C_{ijkl}\left(\mathbf{y},\,t-\tau\right)\frac{\partial\varepsilon_{ij}^{0}\left(\mathbf{x},\tau\right)}{\partial\tau}\mathrm{d}\tau\right\rangle +\left\langle \int_{0}^{t}C_{ijkl}\left(\mathbf{y},\,t-\tau\right)\frac{\partial e_{ij}^{1}\left(\mathbf{x},\mathbf{y},\tau\right)}{\partial\tau}\mathrm{d}\tau\right\rangle . \tag{2.34}$$

From relationship (2.34) we can derive a constitutive equation that will have validity on the global scale problem.

Since $u_{i}^{0}\left(\mathbf{x},t\right)$ is independent of the local coordinate $\mathbf{y}$, (2.14) shows us that the leading term in the strains is as well: $\varepsilon_{ij}^{0}=\varepsilon_{ij}^{0}\left(\mathbf{x},t\right)$. Therefore, this global scale strain can be pulled outside of the volume averaging integral. By employing the definition of the strain given by (2.15), we produce the following:

$$\begin{aligned}\bar{\sigma}_{ij}^{1}\left(\mathbf{x},t\right)= & \int_{0}^{t}\left\langle C_{ijkl}\left(\mathbf{y},\,t-\tau\right)\right\rangle \frac{\partial\varepsilon_{k}^{0}\left(\mathbf{x},\tau\right)}{\partial\tau}\mathrm{d}\tau\\ & +\left\langle \int_{0}^{t}C_{ijkl}\left(\mathbf{y},\,t-\tau\right)\frac{\partial}{\partial\tau}\left(\frac{\partial u_{k}^{1}\left(\mathbf{x},\mathbf{y},\tau\right)}{\partial y_{l}}\right)\mathrm{d}\tau\right\rangle .\end{aligned} \tag{2.35}$$

We now apply the product rule to the second term on the right-hand side of (2.35). This action will yield

$$\begin{aligned}\bar{\sigma}_{ij}^{1}(\mathbf{x},t) &= \int_0^t \left\langle C_{ijkl}\left(\mathbf{y},\, t-\tau\right)\right\rangle \frac{\partial \varepsilon_k^0\left(\mathbf{x},\tau\right)}{\partial \tau}\mathrm{d}\tau \\ &+ \left\langle \int_0^t \frac{\partial}{\partial y_l}\left(C_{ijkl}\left(\mathbf{y},\, t-\tau\right)\frac{\partial u_k^1\left(\mathbf{x},\mathbf{y},\tau\right)}{\partial \tau}\right)\mathrm{d}\tau \right\rangle \\ &- \left\langle \int_0^t \frac{\partial}{\partial y_l}\left(C_{ijkl}\left(\mathbf{y},\, t-\tau\right)\right)\frac{\partial u_k^1\left(\mathbf{x},\mathbf{y},\tau\right)}{\partial \tau}\mathrm{d}\tau \right\rangle.\end{aligned} \tag{2.36}$$

Using the divergence theorem, we may convert the volume integral belonging to the second term on the right-hand side of (2.36) into two boundary integrals: one along the internal boundaries Γ and one along the external boundary ∂Y. This action will produce the following:

$$\begin{aligned}\bar{\sigma}_{ij}^{1}(\mathbf{x},t) &= \int_0^t \left\langle C_{ijkl}\left(\mathbf{y},\, t-\tau\right)\right\rangle \frac{\partial \varepsilon_k^0\left(\mathbf{x},\tau\right)}{\partial \tau}\mathrm{d}\tau \\ &+ \frac{1}{|Y|}\int_{\partial Y}\left\{\int_0^t C_{ijkl}\left(\mathbf{y},\, t-\tau\right) n_l\,\frac{\partial u_k^1\left(\mathbf{x},\mathbf{y},\tau\right)}{\partial \tau}\,\mathrm{d}\tau\right\}\mathrm{d}S \\ &+ \frac{1}{|Y|}\int_{\Gamma}\left\{\int_0^t C_{ijkl}\left(\mathbf{y},\, t-\tau\right) n_l\,\frac{\partial u_k^1\left(\mathbf{x},\mathbf{y},\tau\right)}{\partial \tau}\,\mathrm{d}\tau\right\}\mathrm{d}S \\ &- \left\langle \int_0^t \frac{\partial}{\partial y_l}\left(C_{ijkl}\left(\mathbf{y},\, t-\tau\right)\right)\frac{\partial u_k^1\left(\mathbf{x},\mathbf{y},\tau\right)}{\partial \tau}\mathrm{d}\tau \right\rangle.\end{aligned} \tag{2.37}$$

The integral over the external boundary of the unit cell is zero if we can assume symmetry in the material properties along the external boundary ∂Y. We must also assume that the displacements are continuous along the shared boundary between one unit cell and the next.

The last term on the right-hand side of (2.37) represents the volume average of stiffness gradient against the entire history of the displacements $u_k^1\left(\mathbf{x},\mathbf{y},t\right)$. Here we require that the relaxation moduli $C_{ijkl}(\mathbf{y},t)$ must be piecewise constant over the volume Y. Therefore the stiffness gradient appears as a distribution of delta functions along the internal boundaries between the constituents Γ. Since these internal surfaces occupy no volume, the volume average of stiffness gradient against the entire history of the displacements will also be zero.

Equation (2.37) can now be expressed as

$$\begin{aligned}\bar{\sigma}_{ij}^{1}\left(\mathbf{x},\, t\right) &= \int_{0}^{t} \left\langle C_{ijkl}\left(\mathbf{y},\, t-\tau\right)\right\rangle \frac{\partial \varepsilon_{k}^{0}\left(\mathbf{x},\tau\right)}{\partial \tau}\,\mathrm{d}\tau \\ &\quad + \frac{1}{|Y|}\int_{\Gamma}\left\{\int_{0}^{t} C_{ijkl}\left(\mathbf{y},\, t-\tau\right) n_{l}\,\frac{\partial u_{k}^{1}\left(\mathbf{x},\mathbf{y},\tau\right)}{\partial \tau}\,\mathrm{d}\tau\right\}\mathrm{d}S.\end{aligned} \qquad (2.38)$$

Equation (2.38) represents our candidate for the global-local constitutive equation. To confirm that this equation is a valid multiscale constitutive equation, we must prove that the global scale stress is equal to the volume average of the local scale stress field $\bar{\sigma}_{ij}^{1}\left(\mathbf{x},t\right)$. Our proof begins with the initial boundary value problem on the order δ^{0} .

With proper constitutive and kinematic relationships, equation (2.23) can be used to pose an initial boundary value problem on the order δ^{0} . In this boundary value problem, as with the last, the volume of interest is the unit cell. The equations associated with this boundary value problem are

$$\begin{aligned}&\frac{\partial}{\partial x_{j}}\left(\int_{0}^{t} C_{ijkl}\left(\mathbf{y};\; t-\tau\right)\frac{\partial}{\partial \tau}\left(\frac{\partial u_{k}^{0}(\mathbf{x},\tau)}{\partial x_{l}}\right) d\tau\right) \\ &+\frac{\partial}{\partial y_{j}}\left(\int_{0}^{t} C_{ijkl}\left(\mathbf{y};\; t-\tau\right)\frac{\partial}{\partial \tau}\left(\frac{\partial u_{k}^{1}(\mathbf{x},\mathbf{y},\tau)}{\partial x_{l}}\right) d\tau\right) \\ &+\frac{\partial}{\partial x_{j}}\left(\int_{0}^{t} C_{ijkl}\left(\mathbf{y};\; t-\tau\right)\frac{\partial}{\partial \tau}\left(\frac{\partial u_{k}^{1}(\mathbf{x},\mathbf{y},\tau)}{\partial y_{l}}\right) d\tau\right) \\ &+\frac{\partial}{\partial y_{j}}\left(\int_{0}^{t} C_{ijkl}\left(\mathbf{y};\; t-\tau\right)\frac{\partial}{\partial \tau}\left(\frac{\partial u_{k}^{2}(\mathbf{x},\mathbf{y},\tau)}{\partial y_{l}}\right) d\tau\right)\end{aligned} \quad = \quad 0 \qquad \text{in } Y \qquad (2.39)$$

$$u_i^1(\mathbf{x},\mathbf{y},t)=u_i^1(\mathbf{x},\mathbf{y}+\mathbf{d},\,t) \quad \text{and} \quad u_i^2(\mathbf{x},\mathbf{y},t)=u_i^2(\mathbf{x},\mathbf{y}+\mathbf{d},\,t) \qquad \text{on } \partial Y \qquad (2.40)$$

$$\begin{aligned}\sigma_{ij}^1(\mathbf{x},\mathbf{y},t)n_j &= -\sigma_{ij}^1(\mathbf{x},\mathbf{y}+\mathbf{d},t)n_j\\ \sigma_{ij}^2(\mathbf{x},\mathbf{y},t)n_j &= -\sigma_{ij}^2(\mathbf{x},\mathbf{y}+\mathbf{d},t)n_j\end{aligned} \qquad \text{on } \partial Y \qquad (2.41)$$

$$\sigma_{ij}^2(\mathbf{x},\mathbf{y},t)n_j = \frac{\left[u_j^2(\mathbf{x},\mathbf{y},t)\right]}{\lambda(\mathbf{x},\mathbf{y},t)}\left(1-\alpha(\mathbf{x},\mathbf{y},t)\right)\int_0^t E^{cz}(\mathbf{x},\mathbf{y},t-\tau)\frac{\partial\lambda(\mathbf{x},\mathbf{y},\tau)}{\partial\tau}\mathrm{d}\tau \qquad \text{on } \Gamma_{CT}\,. \qquad (2.42)$$

Equations (2.39) through (2.42) define the δ^0 boundary value problem. This boundary value problem is well-posed.

We now consider taking a volume average over the unit cell of the equilibrium equation (2.39). This action will yield the following

$$\begin{aligned}&\left\langle \frac{\partial}{\partial x_j}\left(\int_0^t C_{ijkl}(\mathbf{y},\ t-\tau)\frac{\partial}{\partial\tau}\left(\frac{\partial u_k^0(\mathbf{x},\tau)}{\partial x_l}\right)d\tau\right)\right\rangle\\ &+\left\langle \frac{\partial}{\partial y_j}\left(\int_0^t C_{ijkl}(\mathbf{y},\ t-\tau)\frac{\partial}{\partial\tau}\left(\frac{\partial u_k^1(\mathbf{x},\mathbf{y},\tau)}{\partial x_l}\right)d\tau\right)\right\rangle\\ &+\left\langle \frac{\partial}{\partial x_j}\left(\int_0^t C_{ijkl}(\mathbf{y},\ t-\tau)\frac{\partial}{\partial\tau}\left(\frac{\partial u_k^1(\mathbf{x},\mathbf{y},\tau)}{\partial y_l}\right)d\tau\right)\right\rangle\\ &+\left\langle \frac{\partial}{\partial y_j}\left(\int_0^t C_{ijkl}(\mathbf{y},\ t-\tau)\frac{\partial}{\partial\tau}\left(\frac{\partial u_k^2(\mathbf{x},\mathbf{y},\tau)}{\partial y_l}\right)d\tau\right)\right\rangle\end{aligned} = 0 \qquad \text{in } Y\,. \qquad (2.43)$$

For the first term in (2.43) we can draw outside the volume integral both the differentiation with respect to the global coordinate $\mathbf{x}$ and the leading displacement contribution $u_k^0(\mathbf{x},\,t)$. Similarly, for the third term in (2.43) we can also draw outside the volume integral the differentiation with respect to the global coordinate $\mathbf{x}$. For the second and fourth terms in (2.43), we can apply the divergence theorem in order to convert the volume integral into an integral over the surface of Y. These actions will yield the following result

$$\begin{aligned}&\frac{\partial}{\partial x_j}\left(\int_0^t \left\langle C_{ijkl}\left(\mathbf{y},\ t-\tau\right)\right\rangle \frac{\partial \varepsilon_k^0(\mathbf{x},\tau)}{\partial \tau}\mathrm{d}\tau\right)\\ &+\frac{1}{\left|Y\right|}\int_{\partial Y+\Gamma}\left(\int_0^t C_{ijkl}\left(\mathbf{y},\ t-\tau\right)n_j\frac{\partial}{\partial \tau}\left(\frac{\partial u_k^1(\mathbf{x},\mathbf{y},\tau)}{\partial x_l}\right)\mathrm{d}\tau\right)\mathrm{d}S\\ &+\frac{\partial}{\partial x_j}\left\langle\int_0^t C_{ijkl}\left(\mathbf{y},\ t-\tau\right)\frac{\partial}{\partial \tau}\left(\frac{\partial u_k^1(\mathbf{x},\mathbf{y},\tau)}{\partial y_l}\right)\mathrm{d}\tau\right\rangle\\ &+\frac{1}{\left|Y\right|}\int_{\partial Y+\Gamma}\left(\int_0^t C_{ijkl}\left(\mathbf{y},\ t-\tau\right)n_j\frac{\partial}{\partial \tau}\left(\frac{\partial u_k^2(\mathbf{x},\mathbf{y},\tau)}{\partial y_l}\right)\mathrm{d}\tau\right)\mathrm{d}S\end{aligned} \quad = \quad 0 \qquad \text{in } Y. \qquad (2.44)$$

For the second and fourth terms in (2.44), we recognize that because of the periodicity of the stress field, that the contributions made by the surface integrals along the external boundaries ∂Y are zero. Furthermore, since all internal boundaries are assumed to be self-equilibrated, the contributions made by the surface integrals along the internal boundaries Γ are also zero. For the third term in (2.44) we can apply the product rule and the divergence theorem in the same manner as we did to produce (2.36), (2.37), and (2.38). The resulting expression is as follows:

$$\begin{aligned}&\frac{\partial}{\partial x_j}\left(\int_0^t \left\langle C_{ijkl}\left(\mathbf{y},\ t-\tau\right)\right\rangle \frac{\partial \varepsilon_k^0(\mathbf{x},\tau)}{\partial \tau}\mathrm{d}\tau\right)\\ &+\frac{\partial}{\partial x_j}\left(\frac{1}{\left|Y\right|}\int_{\partial Y+\Gamma}\left(\int_0^t C_{ijkl}\left(\mathbf{y},\ t-\tau\right)n_l\frac{\partial u_k^1(\mathbf{x},\mathbf{y},\tau)}{\partial \tau}\,\mathrm{d}\tau\right)\mathrm{d}S\right)\end{aligned} = 0 \qquad \text{in } Y. \qquad (2.45)$$

It should be pointed out that equation (2.45) contains a surface integral over the external boundary of the unit cell ∂Y. Periodicity arguments cannot be used to get rid of these contributions because the integrand is not a traction. However, if we assume material symmetry along the external boundary, then this external boundary integral will be zero. Thus (2.45) becomes

$$\begin{aligned}&\frac{\partial}{\partial x_j}\left(\int_0^t \left\langle C_{ijkl}\left(\mathbf{y},\ t-\tau\right)\right\rangle \frac{\partial \varepsilon_k^0(\mathbf{x},\tau)}{\partial \tau}\mathrm{d}\tau\right)\\ &+\frac{\partial}{\partial x_j}\left(\frac{1}{|Y|}\int_\Gamma\left(\int_0^t C_{ijkl}\left(\mathbf{y},\ t-\tau\right)n_l\frac{\partial u_k^1(\mathbf{x},\mathbf{y},\tau)}{\partial \tau}\ \mathrm{d}\tau\right)\mathrm{d}S\right) = 0 \qquad \text{in } Y. \qquad (2.46)\end{aligned}$$

By using our candidate multiscale constitutive equation (2.38) we can write (2.46) more concisely as

$$\frac{\partial \bar{\sigma}_{ij}^1(\mathbf{x},\ t)}{\partial x_j} = 0 \qquad \text{in } Y. \qquad (2.47)$$

Because the leading order term of the displacements $u_i^0(\mathbf{x},\ t)$ is independent of the local coordinate $\mathbf{y}$, the leading order terms in the series expansions of the boundary conditions (2.8) and (2.9) are also independent of the local coordinate. Consequently, all the leading order terms are equal to the average of the field variables over the unit cell Y. The global scale stress is equal to the volume average of the local scale stress field $\bar{\sigma}_{ij}^1(\mathbf{x},t)$, and (2.38) is a valid expression of the multiscale constitutive behavior.

2.3 Multiscale Boundary Value Problem Summary

The global scale boundary value problem for the averages of the field variables over the unit cell is defined by the following:

$$\frac{\partial \bar{\sigma}_{ij}^1(\mathbf{x},\ t)}{\partial x_j} = 0 \qquad \text{in } X$$

$$\varepsilon_{ij}^{0}(\mathbf{x},\ t)=\frac{1}{2}\left(\frac{\partial u_i^0(\mathbf{x},\ t)}{\partial x_j}+\frac{\partial u_j^0(\mathbf{x},\ t)}{\partial x_i}\right) \qquad \text{in } X$$

$$\begin{aligned}\bar{\sigma}_{ij}^{1}(\mathbf{x},t)=&\int_0^t \left\langle C_{ijkl}(\mathbf{y},\ t-\tau)\right\rangle \frac{\partial \varepsilon_k^0(\mathbf{x},\tau)}{\partial \tau}\,\mathrm{d}\tau \\ &+\frac{1}{|Y|}\int_\Gamma \left\{\int_0^t C_{ijkl}(\mathbf{y},\ t-\tau)\, n_l\, \frac{\partial u_k^1(\mathbf{x},\mathbf{y},\tau)}{\partial \tau}\,\mathrm{d}\tau\right\}\mathrm{d}S\end{aligned} \qquad \text{in } X$$

$$\bar{\sigma}_{ij}^{1}(\mathbf{x},t)\,n_j = \hat{T}_i^{\,0}(\mathbf{x},t) \qquad \text{on } \partial X_T$$

$$u_i^0(\mathbf{x},t) = \hat{u}_i^0(\mathbf{x},t) \qquad \text{on } \partial X_u\,.$$

The local scale boundary value problem over the unit cell is defined by the following:

$$\begin{aligned}&\frac{\partial}{\partial y_j}\left(\int_0^t C_{ijkl}(\mathbf{y},\ t-\tau)\frac{\partial}{\partial \tau}\left(\frac{\partial u_k^1(\mathbf{x},\mathbf{y},\tau)}{\partial y_l}\right) d\tau\right) \\ &+\frac{\partial}{\partial y_j}\left(\int_0^t C_{ijkl}(\mathbf{y},\ t-\tau)\frac{\partial}{\partial \tau}\left(\frac{\partial u_k^0(\mathbf{x},\ \tau)}{\partial x_l}\right) d\tau\right)=0\end{aligned} \qquad \text{in } Y$$

$$u_i^1(\mathbf{x},\mathbf{y},t)=u_i^1(\mathbf{x},\mathbf{y}+\mathbf{d},\ t) \qquad \text{on } \partial Y$$

$$\sigma_{ij}^1(\mathbf{x},\mathbf{y},t)\,n_j=-\sigma_{ij}^1(\mathbf{x},\mathbf{y}+\mathbf{d},t)\,n_j \qquad \text{on } \partial Y$$

$$\sigma_{ij}^{1}\left(\mathbf{x},\mathbf{y},t\right)n_j = \frac{\left[u_j^{1}\left(\mathbf{x},\mathbf{y},t\right)\right]}{\lambda\left(\mathbf{x},\mathbf{y},t\right)}\left(1-\alpha\left(\mathbf{x},\mathbf{y},t\right)\right)\int_0^t E^{cz}\left(\mathbf{x},\mathbf{y},t-\tau\right)\frac{\partial\lambda^{1}\left(\mathbf{x},\mathbf{y},\tau\right)}{\partial\tau}\mathrm{d}\tau \qquad \text{on } \Gamma_{CT}\,.$$

Both global and local scale problems are cast into separate finite element formulations. These formulations are developed in Section 4. The resulting finite element codes are then joined together by a numerical interface which allows the transfer of global scale strains $\varepsilon_{ij}^{0}\left(\mathbf{x},t\right)$ to the local scale problem and averaged local stresses $\bar{\sigma}_{ij}^{1}\left(\mathbf{x},t\right)$ to the global scale problem.

3. INCREMENTALIZATION OF MULTISCALE CONSTITUTIVE EQUATIONS

In the work reported by Zocher, et al. (1997), it has been demonstrated that hereditary integrals of the type shown in (2.5) can be cast into an incrementalized form. This form may then be easily placed into a finite element code. The goal of this chapter is to extend the incrementalization procedure outlined by Zocher, et al., to the multiscale constitutive relationship (2.38) we developed in Section 2. Once in an incrementalized form, we can use these constitutive equations to construct a finite element code that can model the effects of multiscale damage in viscoelastic composites.

To start, we must permit our time line to be expressed in terms of discrete intervals Δt. Whereas Zocher, et al. addresses their incrementalization procedure in terms of reduced time, we will dispense with this convention since the effects of temperature changes have been excluded from this theory. The key expression found in this incrementalization procedure is the definition for the global scale stress increment

$$\Delta\bar{\sigma}_{ij}^{1} \equiv \bar{\sigma}_{ij}^{1}\left(\mathbf{x},\ t+\Delta t\right)-\bar{\sigma}_{ij}^{1}\left(\mathbf{x},\ t\right) \tag{3.1}$$

where $\Delta\bar{\sigma}_{ij}^{1}$ is the increment in the global scale stress; Δt is the increment in time; $\bar{\sigma}_{ij}^{1}\left(\mathbf{x},\ t\right)$ is the value of the global scale stress at time t; and $\bar{\sigma}_{ij}^{1}\left(\mathbf{x},\ t+\Delta t\right)$ is the value of the global scale stress at time $t+\Delta t$.

It will be assumed that the global scale stress $\bar{\sigma}_{ij}^{1}\left(\mathbf{x},\ t\right)$ is a known quantity at time t. Thus, the value of stress at time t is given by the following

$$\begin{aligned}\bar{\sigma}_{ij}^{1}\left(\mathbf{x},t\right)=&\int_{0}^{t}\left\langle C_{ijkl}\left(\mathbf{y},t-\tau\right)\right\rangle\frac{\partial\varepsilon_{kl}^{0}\left(\mathbf{x},\tau\right)}{\partial\tau}d\tau\\&+\frac{1}{\left|Y\right|}\int_{\Gamma}\left\{\int_{0}^{t}C_{ijkl}\left(\mathbf{y},t-\tau\right)n_{l}\ \frac{\partial u_{k}^{1}\left(\mathbf{x},\mathbf{y},\tau\right)}{\partial\tau}d\tau\right\}dS.\end{aligned} \tag{3.2}$$

We now seek an expression for the global stress at the subsequent time $t+\Delta t$. This value of the stress is expressed by

$$\begin{aligned}\bar{\sigma}_{ij}^{1}\left(\mathbf{x},\ t+\Delta t\right) = &\int_{0}^{t+\Delta t} \left\langle C_{ijkl}\left(\mathbf{y}, t+\Delta t-\tau\right)\right\rangle \frac{\partial \varepsilon_{kl}^{0}\left(\mathbf{x}, \tau\right)}{\partial \tau} d\tau \\ &+\frac{1}{\left|Y\right|}\int_{\Gamma}\left\{\int_{0}^{t+\Delta t} C_{ijkl}\left(\mathbf{y}, t+\Delta t-\tau\right) n_l \ \frac{\partial u_k^{1}\left(\mathbf{x},\mathbf{y},\tau\right)}{\partial \tau} d\tau\right\} dS.\end{aligned} \tag{3.3}$$

To proceed, let us define the increment in the local stiffness ΔC_{ijkl}. This increment will be defined by the following expression:

$$\Delta C_{ijkl} \equiv C_{ijkl}\left(\mathbf{y}, t+\Delta t\right) - C_{ijkl}\left(\mathbf{y}, t\right). \tag{3.4}$$

Applying this definition to (3.3) yields:

$$\begin{aligned}\bar{\sigma}_{ij}^{1}\left(\mathbf{x}, t\right) = &\int_{0}^{t+\Delta t} \left\langle C_{ijkl}\left(\mathbf{y}, t-\tau\right)\right\rangle \frac{\partial \varepsilon_{kl}^{0}\left(\mathbf{x}, \tau\right)}{\partial \tau} d\tau \\ &+\int_{0}^{t+\Delta t} \left\langle \Delta C_{ijkl}\right\rangle \frac{\partial \varepsilon_{kl}^{0}\left(\mathbf{x}, \tau\right)}{\partial \tau} d\tau \\ &+\frac{1}{\left|Y\right|}\int_{\Gamma}\left\{\int_{0}^{t+\Delta t} C_{ijkl}\left(\mathbf{y}, t-\tau\right) n_l \ \frac{\partial u_k^{1}\left(\mathbf{x},\mathbf{y},\tau\right)}{\partial \tau} d\tau\right\} dS \\ &+\frac{1}{\left|Y\right|}\int_{\Gamma}\left\{\int_{0}^{t+\Delta t} \Delta C_{ijkl} n_l \ \frac{\partial u_k^{1}\left(\mathbf{x},\mathbf{y},\tau\right)}{\partial \tau} d\tau\right\} dS.\end{aligned} \tag{3.5}$$

Expression (3.5) may be separated into two parts: 1) those contributions made during the current time step, and 2) those contributions attributed to all events prior to the current time step. Therefore,

$$
\begin{aligned}
\bar{\sigma}_{ij}^{1}(\mathbf{x},t) = & \int_{0}^{t} \left\langle C_{ijkl}(\mathbf{y},t-\tau) \right\rangle \frac{\partial \varepsilon_{kl}^{0}(\mathbf{x},\tau)}{\partial \tau} d\tau + \int_{t}^{t+\Delta t} \left\langle C_{ijkl}(\mathbf{y},t-\tau) \right\rangle \frac{\partial \varepsilon_{kl}^{0}(\mathbf{x},\tau)}{\partial \tau} d\tau \\
& + \int_{0}^{t} \left\langle \Delta C_{ijkl} \right\rangle \frac{\partial \varepsilon_{kl}^{0}(\mathbf{x},\tau)}{\partial \tau} d\tau + \int_{t}^{t+\Delta t} \left\langle \Delta C_{ijkl} \right\rangle \frac{\partial \varepsilon_{kl}^{0}(\mathbf{x},\tau)}{\partial \tau} d\tau \\
& + \frac{1}{|Y|} \int_{\Gamma} \left\{ \int_{0}^{t} C_{ijkl}(\mathbf{y},t-\tau)\, n_l \, \frac{\partial u_k^{1}(\mathbf{x},\mathbf{y},\tau)}{\partial \tau} d\tau \right\} dS \\
& + \frac{1}{|Y|} \int_{\Gamma} \left\{ \int_{t}^{t+\Delta t} C_{ijkl}(\mathbf{y},t-\tau)\, n_l \, \frac{\partial u_k^{1}(\mathbf{x},\mathbf{y},\tau)}{\partial \tau} d\tau \right\} dS \\
& + \frac{1}{|Y|} \int_{\Gamma} \left\{ \int_{0}^{t} \Delta C_{ijkl} n_l \, \frac{\partial u_k^{1}(\mathbf{x},\mathbf{y},\tau)}{\partial \tau} d\tau \right\} dS \\
& + \frac{1}{|Y|} \int_{\Gamma} \left\{ \int_{t}^{t+\Delta t} \Delta C_{ijkl} n_l \, \frac{\partial u_k^{1}(\mathbf{x},\mathbf{y},\tau)}{\partial \tau} d\tau \right\} dS.
\end{aligned}
\tag{3.6}
$$

Now the increment in the stress $\Delta\bar{\sigma}_{ij}^{1}$ may be directly expressed by subtracting (3.6) from (3.2), which gives

$$
\begin{aligned}
\Delta\bar{\sigma}_{ij}^{1} = & \int_{0}^{t} \left\langle C_{ijkl}(\mathbf{y},t-\tau) \right\rangle \frac{\partial \varepsilon_{kl}^{0}(\mathbf{x},\tau)}{\partial \tau} d\tau \\
& + \int_{0}^{t} \left\langle \Delta C_{ijkl} \right\rangle \frac{\partial \varepsilon_{kl}^{0}(\mathbf{x},\tau)}{\partial \tau} d\tau + \int_{t}^{t+\Delta t} \left\langle \Delta C_{ijkl} \right\rangle \frac{\partial \varepsilon_{kl}^{0}(\mathbf{x},\tau)}{\partial \tau} d\tau \\
& + \frac{1}{|Y|} \int_{\Gamma} \left\{ \int_{0}^{t} C_{ijkl}(\mathbf{y},t-\tau)\, n_l \, \frac{\partial u_k^{1}(\mathbf{x},\mathbf{y},\tau)}{\partial \tau} d\tau \right\} dS \\
& + \frac{1}{|Y|} \int_{\Gamma} \left\{ \int_{t}^{t+\Delta t} C_{ijkl}(\mathbf{y},t-\tau)\, n_l \, \frac{\partial u_k^{1}(\mathbf{x},\mathbf{y},\tau)}{\partial \tau} d\tau \right\} dS \\
& + \frac{1}{|Y|} \int_{\Gamma} \left\{ \int_{0}^{t} \Delta C_{ijkl} n_l \, \frac{\partial u_k^{1}(\mathbf{x},\mathbf{y},\tau)}{\partial \tau} d\tau \right\} dS \\
& + \frac{1}{|Y|} \int_{\Gamma} \left\{ \int_{t}^{t+\Delta t} \Delta C_{ijkl} n_l \, \frac{\partial u_k^{1}(\mathbf{x},\mathbf{y},\tau)}{\partial \tau} d\tau \right\} dS.
\end{aligned}
\tag{3.7}
$$

At this point, we will assume that the viscoelastic kernel function $C_{ijkl}\left(\mathbf{y},t\right)$ for the constituents in the unit cell may be represented by a generalized Maxwell model via the expression

$$C_{ijkl}\left(\mathbf{y},\,t\right) \;=\; C_{ijkl_{\infty}}\left(\mathbf{y}\right) + \sum_{q=1}^{M_{ijkl}} C_{ijkl_q}\left(\mathbf{y}\right)\,\exp\left(-t\big/\rho_{ijkl_q}\left(\mathbf{y}\right)\right) \qquad \text{no sum on } ijkl \qquad (3.8)$$

where

$$\rho_{ijkl_q}\left(\mathbf{y}\right) \;=\; \eta_{ijkl_q}\left(\mathbf{y}\right)\big/C_{ijkl_q}\left(\mathbf{y}\right) \qquad \text{no sum on } ijkl \qquad (3.9)$$

are known as the time relaxation constants.

In the above equations, the $C_{ijkl_q}\left(\mathbf{y}\right)$ represent Hookean spring coefficient values while the $\eta_{ijkl_q}\left(\mathbf{y}\right)$ represent Newtonian dashpot values. This type of spring-dashpot model is a well-accepted form for the expression of linear viscoelastic constitutive properties. As a direct consequence of the assumed form of the viscoelastic stiffness, the expression for ΔC_{ijkl} is given by

$$\Delta C_{ijkl} \;=\; -\sum_{q=1}^{M_{ijkl}} C_{ijkl_q}\left(\mathbf{y}\right)\,\exp\left(-t\big/\rho_{ijkl_q}\left(\mathbf{y}\right)\right)\cdot\left(1-\exp\left(-\Delta t\big/\rho_{ijkl_q}\left(\mathbf{y}\right)\right)\right) \qquad (3.10)$$

where there is no sum on *ijkl*.

It will also be assumed that the global strain increment $\varepsilon_{kl}^{0}\left(\mathbf{x},\,t\right)$ and the local displacement increment $u_k^1\left(\mathbf{x},\mathbf{y},\,t\right)$ will vary linearly over any time interval Δt. These assumptions may be expressed by the following

$$\varepsilon_{kl}^{0}\left(\mathbf{x},\, t\right)=\varepsilon_{kl}^{0}\left(\mathbf{x},\, \tau\right)+\, \dot{\varepsilon}_{kl}^{0}\left(\mathbf{x},\, \tau\right)\cdot\left(t-\tau\right)\cdot H\left(t-\tau\right) \tag{3.11}$$

$$u_{k}^{1}\left(\mathbf{x},\mathbf{y},\, t\right)=u_{k}^{1}\left(\mathbf{x},\mathbf{y},\, \tau\right)+\, \dot{u}_{k}^{1}\left(\mathbf{x},\mathbf{y},\tau\right)\cdot\left(t-\tau\right)\cdot H\left(t-\tau\right) \tag{3.12}$$

where τ is the time at the beginning of the interval; $\varepsilon_{kl}^{0}\left(\mathbf{x},\, \tau\right)$ represents the value of the global strain at the beginning of the time interval; $\dot{\varepsilon}_{kl}^{0}\left(\mathbf{x},\, \tau\right)$ represents the strain rate during the time interval; $u_{k}^{1}\left(\mathbf{x},\mathbf{y},\tau\right)$ represents the value of the local displacement at the beginning of the time interval; $\dot{u}_{k}^{1}\left(\mathbf{x},\mathbf{y},\tau\right)$ represents the local scale displacement rate during the time interval and $H\left(t-\tau\right)$ is the Heaviside step function.

With these two approximations, the hereditary integrals within equation (3.7) may be integrated in closed form to produce the following expression:

$$\begin{aligned}\Delta\bar{\sigma}_{ij}^{1} &= \left\langle C'_{ijkl}\left(\mathbf{y}\right)\right\rangle \Delta\varepsilon_{kl}^{0} + \left\langle \Delta\sigma_{ij}^{R}\right\rangle \\ &+\frac{1}{\left|Y\right|}\int_{\Gamma} C'_{ijkl}\left(\mathbf{y}\right)\, n_{l}\, \Delta u_{k}^{1}\, dS \\ &+\frac{1}{\left|Y\right|}\int_{\Gamma} \Delta\tilde{\sigma}_{ij}^{R}\, dS\end{aligned} \tag{3.13}$$

where $C'_{ijkl}\left(\mathbf{y}\right)$ represents the local scale viscoelastic stiffness during the time between t and $t+\Delta t$:

$$C'_{ijkl}\left(\mathbf{y}\right) \equiv C_{ijkl_{\infty}}\left(\mathbf{y}\right)+\frac{1}{\Delta t}\sum_{q=1}^{M_{ijkl}} \eta_{ijkl_{q}}\left(\mathbf{y}\right)\cdot\left(1-\exp\left(-\Delta t\big/\rho_{ijkl_{q}}\left(\mathbf{y}\right)\right)\right) \tag{3.14}$$

and where $\Delta\varepsilon_{kl}^{0}$ and Δu_{k}^{1} are given by the following:

$$\Delta\varepsilon_{kl}^{0} \equiv \dot{\varepsilon}_{kl}^{0}\left(\mathbf{x},\ t\right)\Delta t \tag{3.15}$$

$$\Delta u_{k}^{1} \equiv \dot{u}_{k}^{1}\left(\mathbf{x},\mathbf{y},t\right)\Delta t\ . \tag{3.16}$$

For constant time intervals Δt, the value of $C'_{ijkl}\left(\mathbf{y}\right)$ also remains constant.

Also in equation (3.13), are two residual terms, $\Delta\sigma_{ij}^{R}$ and $\Delta\tilde{\sigma}_{ij}^{R}$, which represent residual effects on the global stress due to the history of the strain. These residual terms may be expressed by the following

$$\Delta\sigma_{ij}^{R} = -\sum_{k=1}^{3}\sum_{m=1}^{3} A_{ijkl_q}\left(\mathbf{x},\mathbf{y},t\right) \tag{3.17}$$

$$\Delta\tilde{\sigma}_{ij}^{R} = -\sum_{k=1}^{3}\sum_{m=1}^{3} \tilde{A}_{ijkl_q}\left(\mathbf{x},\mathbf{y},t\right) \tag{3.18}$$

where

$$A_{ijkl_q}\left(\mathbf{x},\mathbf{y},t\right)=\sum_{q=1}^{M_{ijkl}}\left[1-\exp\left(-\Delta t\big/\rho_{ijkl_q}\left(\mathbf{y}\right)\right)\right]\cdot S_{ijkl_q}\left(\mathbf{x},\mathbf{y},t\right) \quad \text{no sum on } ijkl \tag{3.19}$$

$$\tilde{A}_{ijkl_q}\left(\mathbf{x},\mathbf{y},t\right)=\sum_{q=1}^{M_{ijkl}}\left[1-\exp\left(-\Delta t\big/\tilde{\rho}_{ijkl_q}\left(\mathbf{y}\right)\right)\right]\cdot \tilde{S}_{ijkl_q}\left(\mathbf{x},\mathbf{y},t\right) \quad \text{no sum on } ijkl \tag{3.20}$$

and

$$\begin{aligned} S_{ijkl_q}\left(\mathbf{x},\mathbf{y},t\right) \equiv{}& \exp\left(-\Delta t\big/\rho_{ijkl_q}\left(\mathbf{y}\right)\right)\cdot\left[S_{ijkl_q}\left(\mathbf{x},\mathbf{y},t-\Delta t\right)\right] \\ &-\eta_{ijkl_q}\left(\mathbf{y}\right)\cdot\frac{\Delta\varepsilon_{kl}^{0}}{\Delta t}\cdot\left[1-\exp\left(-\Delta t\big/\rho_{ijkl_q}\left(\mathbf{y}\right)\right)\right] \end{aligned} \quad \text{no sum on } ijkl \tag{3.21}$$

$$\tilde{S}_{ijkl_q}\left(\mathbf{x},\mathbf{y},t\right) \equiv \exp\left(-\Delta t \big/ \rho_{ijkl_q}(\mathbf{y})\right)\cdot\left[\tilde{S}_{ijkl_q}\left(\mathbf{x},\mathbf{y},t-\Delta t\right)\right] - \eta_{ijkl_q}(\mathbf{y})\cdot\frac{\Delta u_k^1}{\Delta t} n_l \cdot\left[1-\exp\left(-\Delta t\big/\rho_{ijkl_q}(\mathbf{y})\right)\right] \qquad \text{no sum on } ijkl. \tag{3.22}$$

Equations (3.21) and (3.22) are the centerpiece of this recursive algorithm.

For further simplicity, we have chosen to rewrite (3.13) as follows

$$\Delta\bar{\sigma}_{ij}^1 = \bar{C}'_{ijkl}\Delta\varepsilon_{kl}^0 + \Delta\bar{\sigma}_{ij}^R + \Delta\sigma_{ij}^D \tag{3.23}$$

where the component of the global stress due to local scale damage is

$$\Delta\sigma_{ij}^D = \frac{1}{|Y|}\int_\Gamma C'_{ijkl}\left(\mathbf{y}\right) n_l \,\Delta u_k^1 \, dS + \frac{1}{|Y|}\int_\Gamma \Delta\tilde{\sigma}_{ij}^R \, dS \, . \tag{3.24}$$

4. MULTISCALE FINITE ELEMENT CODE CONSTRUCTION

In this section we develop the finite element formulations for both the global and local scales. Using these formulations we have been able to construct a multiscale finite element program that is capable of solving multiscale initial boundary value problems featuring viscoelastic constitutive behavior and local scale crack growth.

4.1 Global Scale Formulation

In Section 3 we demonstrated how the multiscale constitutive equation (2.38) can be rewritten in an incrementalized form (3.23). We now use this incrementalized constitutive equation as the basis for our global scale finite element formulation.

We begin with the expression for the global scale conservation of linear momentum evaluated at time $t+\Delta t$

$$\frac{\partial \bar{\sigma}_{ij}^{1}\left(\mathbf{x},\, t+\Delta t\right)}{\partial x_j} = 0 . \tag{4.1}$$

To obtain the statement of virtual work, we multiply the conservation of linear momentum by an arbitrary virtual displacement field $\delta u_i^0\left(\mathbf{x},\, t+\Delta t\right)$ and integrate the product over the global domain X

$$\int_X \frac{\partial \bar{\sigma}_{ij}^{1}\left(\mathbf{x},\, t+\Delta t\right)}{\partial x_j} \delta u_i^0\left(\mathbf{x},\, t+\Delta t\right) \mathrm{d}X = 0 \ . \tag{4.2}$$

We then apply the product rule to yield

$$\begin{aligned}&\int_X \left(\bar{\sigma}_{ij}^1(\mathbf{x}, t+\Delta t) \frac{\partial}{\partial x_j}\left(\delta u_i^0(\mathbf{x},\, t+\Delta t)\right)\right) \mathrm{d}X \\ &= \int_X \frac{\partial}{\partial x_j}\left(\bar{\sigma}_{ij}^1(\mathbf{x}, t+\Delta t)\, \delta u_i^0(\mathbf{x},\, t+\Delta t)\right) \mathrm{d}X .\end{aligned} \tag{4.3}$$

By applying the divergence theorem to the term on the right-hand side, we produce

$$\begin{aligned}&\int_X \left(\bar{\sigma}_{ij}^1(\mathbf{x},\, t+\Delta t) \frac{\partial}{\partial x_j}\left(\delta u_i^0(\mathbf{x},\, t+\Delta t)\right)\right) \mathrm{d}X \\ &= \int_{\partial X} \left(\bar{\sigma}_{ij}^1(\mathbf{x}, t+\Delta t)\, \delta u_i^0(\mathbf{x}, t+\Delta t)\, n_j \right) \mathrm{d}S.\end{aligned} \tag{4.4}$$

To incrementalize (4.4), we must define the following:

$$\Delta\varepsilon_{ij}^0 \equiv \varepsilon_{ij}^0(\mathbf{x},\ t+\Delta t) - \varepsilon_{ij}^0(\mathbf{x},\ t) \tag{4.5}$$

$$\Delta u_i^0 \equiv u_i^0(\mathbf{x},\ t+\Delta t) - u_i^0(\mathbf{x},\ t) . \tag{4.6}$$

Recognizing that $u_i^0(\mathbf{x},\ t)$ and $\varepsilon_{ij}^0(\mathbf{x},\ t)$ are known values, we now substitute (4.5) and (4.6) as well as the increment in the global stress (3.1) into (4.4). This action produces the following:

$$\int_X \left(\left(\bar{\sigma}_{ij}^1(\mathbf{x}, t) + \Delta\bar{\sigma}_{ij}^1 \right) \Delta\delta\varepsilon_{ij}^0 \right) \mathrm{d}X = \int_{\partial X} \left(\bar{\sigma}_{ij}^1(\mathbf{x}, t+\Delta t)\, n_j\, \Delta\delta u_i^0 \right) \mathrm{d}S \tag{4.7}$$

where a rearrangement of terms yields

$$\int_X \left(\Delta\bar{\sigma}_{ij}^1 \Delta\delta\varepsilon_{ij}^0 \right) \mathrm{d}X = \int_{\partial X} \left(\bar{\sigma}_{ij}^1(\mathbf{x}, t+\Delta t)\, n_j\, \Delta\delta u_i^0 \right) \mathrm{d}S - \int_X \left(\bar{\sigma}_{ij}^1(\mathbf{x}, t) \Delta\delta\varepsilon_{ij}^0 \right) \mathrm{d}X . \tag{4.8}$$

We now introduce the incrementalized form of the multiscale constitutive equation (3.23) into (4.8). This action gives

$$\begin{aligned}&\int_X \left(\bar{C}'_{ijkl}\Delta\varepsilon^0_{kl} \; + \; \Delta\bar{\sigma}^R_{ij} \; + \; \Delta\sigma^D_{ij}\right)\Delta\delta\varepsilon^0_{ij}\,\mathrm{d}X \\ &= \int_{\partial X}\left(\bar{\sigma}^1_{ij}\left(\mathbf{x},t+\Delta t\right)n_j\,\Delta\delta u^0_i\right)\mathrm{d}S - \int_X\left(\bar{\sigma}^1_{ij}\left(\mathbf{x},t\right)\Delta\delta\varepsilon^0_{ij}\right)\mathrm{d}X.\end{aligned} \tag{4.9}$$

Rearranging terms yields

$$\begin{aligned}\int_X \bar{C}'_{ijkl}\Delta\varepsilon^0_{kl}\,\Delta\delta\varepsilon^0_{ij}\,\mathrm{d}X = &\int_{\partial X}\left(\bar{\sigma}^1_{ij}\left(\mathbf{x},t+\Delta t\right)n_j\,\Delta\delta u^0_i\right)\mathrm{d}S \\ &-\int_X\left(\bar{\sigma}^1_{ij}\left(\mathbf{x},t\right)\Delta\delta\varepsilon^0_{ij}\right)\mathrm{d}X \\ &-\int_X \Delta\bar{\sigma}^R_{ij}\Delta\delta\varepsilon^0_{ij}\,\mathrm{d}X \\ &-\int_X \Delta\sigma^D_{ij}\Delta\delta\varepsilon^0_{ij}\,\mathrm{d}X\end{aligned} \tag{4.10}$$

which can be expressed in matrix notation as

$$\begin{aligned}\int_X\left(\left[D\right]\left[\Delta\delta u^0\right]\right)^T\left[\bar{C}'\right]\left[D\right]\left[\Delta u^0\right]\mathrm{d}X = &\int_{\partial X}\left[\Delta\delta u^0\right]^T\left[\bar{\sigma}^1\left(\mathbf{x},t\right)\right]\left[\;n\;\right]\mathrm{d}S \\ &-\int_X\left(\left[D\right]\left[\Delta\delta u^0\right]\right)^T\left[\;\bar{\sigma}^1\left(\mathbf{x},t\right)\;\right]\mathrm{d}X \\ &-\int_X\left(\left[D\right]\left[\Delta\delta u^0\right]\right)^T\left[\Delta\bar{\sigma}^R\right]\mathrm{d}X \\ &-\int_X\left(\left[D\right]\left[\Delta\delta u^0\right]\right)^T\left[\Delta\sigma^D\right]\mathrm{d}X\end{aligned} \tag{4.11}$$

where $\left[D\right]$ is the strain-displacement relationships operator.

We now assume that the increment in the displacement field over an element $\Delta\left(u_i^0\right)_h^e$ can be given in terms of the displacement increments $\Delta\left(u_i^0\right)_I^e$ at the nodes I. This leads to the following relationship:

$$\Delta\left(u_i^0\right)_h^e = \sum_{I=1}^{N^e} \Delta\left(u_i^0\right)_I^e \psi_I^e\left(\mathbf{x},\, t\right) \tag{4.12}$$

where N^e is the number of interpolation functions $\psi_I^e\left(\mathbf{x},\, t\right)$.

Equation (4.12) can be represented in matrix notation as

$$\left[\Delta\left(u_i^0\right)_h^e\right] = \left[\psi^e\left(\mathbf{x},\, t\right)\right]\left[\Delta\left(u_i^0\right)^e\right]. \tag{4.13}$$

Substituting (4.13) into (4.11) yields

$$\begin{aligned}
&\int_{X^e}\left(\left[B^e(\mathbf{x},t)\right]\left[\Delta\left(\delta u^0\right)^e\right]\right)^T\left[\bar{C}'\right]\left[B^e(\mathbf{x},t)\right]\left[\Delta\left(u^0\right)^e\right]\mathrm{d}X \\
&= \int_{\partial X^e}\left[\Delta\left(\delta u^0\right)^e\right]^T\left[\bar{\sigma}^1(\mathbf{x},t)\right]\left[\, n\,\right]\mathrm{d}S \\
&- \int_{X^e}\left(\left[B^e(\mathbf{x},t)\right]\left[\Delta\left(\delta u^0\right)^e\right]\right)^T\left[\,\bar{\sigma}^1(\mathbf{x},t)\,\right]\mathrm{d}X \\
&- \int_{X^e}\left(\left[B^e(\mathbf{x},t)\right]\left[\Delta\left(\delta u^0\right)^e\right]\right)^T\left[\Delta\bar{\sigma}^R\right]\mathrm{d}X \\
&- \int_{X^e}\left(\left[B^e(\mathbf{x},t)\right]\left[\Delta\left(\delta u^0\right)^e\right]\right)^T\left[\Delta\sigma^D\right]\mathrm{d}X
\end{aligned} \tag{4.14}$$

where

$$\left[B^e(\mathbf{x},\, t)\right] = \left[D\right]\left[\psi^e(\mathbf{x},\, t)\right]. \tag{4.15}$$

Recognizing that $\Delta\left(\delta u_i^0\right)^e$ is an arbitrary function, (4.15) can be simplified by

$$\left[k^e(\mathbf{x},t)\right]=\left[f_1^e(\mathbf{x},t)\right]+\left[f_2^e(\mathbf{x},t)\right]+\left[f_3^e(\mathbf{x},t)\right]+\left[f_4^e(\mathbf{x},t)\right] \tag{4.16}$$

where

$$\left[k^e(\mathbf{x},t)\right]=\int_{X^e}\left[B^e(\mathbf{x},t)\right]^T\left[\bar{C}'\right]\left[B^e(\mathbf{x},t)\right]\mathrm{d}X \tag{4.17}$$

$$\left[f_1^e(\mathbf{x},t)\right]=\int_{\partial X^e}\left[\psi^e(\mathbf{x},t)\right]^T\left[\bar{\sigma}^1(\mathbf{x},t)\right]\left[\,n\,\right]\mathrm{d}S \tag{4.18}$$

$$\left[f_2^e(\mathbf{x},t)\right]=-\int_{X^e}\left[B^e(\mathbf{x},t)\right]^T\left[\bar{\sigma}^1(\mathbf{x},t)\right]\mathrm{d}X \tag{4.19}$$

$$\left[f_3^e(\mathbf{x},t)\right]=-\int_{X^e}\left[B^e(\mathbf{x},t)\right]^T\left[\Delta\bar{\sigma}^R\right]\mathrm{d}X \tag{4.20}$$

$$\left[f_4^e(\mathbf{x},t)\right]=-\int_{X^e}\left[B^e(\mathbf{x},t)\right]^T\left[\Delta\sigma^D\right]\mathrm{d}X\ . \tag{4.21}$$

In the above, $\left[k^e(\mathbf{x},t)\right]$ is the element stiffness matrix; and $\left[f_1^e(\mathbf{x},t)\right]$, $\left[f_2^e(\mathbf{x},t)\right]$, $\left[f_3^e(\mathbf{x},t)\right]$, and $\left[f_4^e(\mathbf{x},t)\right]$ are the contributions to the element load vector due to external boundary tractions; the global scale stress at the beginning of the time step; the change in the viscoelastic residual stress during the time step; and the change in the local scale damage effects during the time step, respectively.

Assembling the element stiffness matrices and load vectors yields

$$\left[K^0(t)\right]\left[\Delta u^0\right]=\left[F^0(t)\right] \tag{4.22}$$

where $\left[K^0(t)\right]$ is the stiffness matrix; $\left[\Delta u^0\right]$ is the displacement vector; and $\left[F^0(t)\right]$ is the force vector for the entire global scale problem.

4.2 Local Scale Formulation

We begin with the expression for the local scale conservation of linear momentum evaluated at time $t+\Delta t$

$$\frac{\partial \sigma_{ij}^1\left(\mathbf{x},\mathbf{y},t+\Delta t\right)}{\partial y_j}\,. \tag{4.23}$$

To obtain the statement of virtual work, we multiply the conservation of linear momentum by the virtual local scale displacement field $\delta u_i^1\left(\mathbf{x},\mathbf{y},t+\Delta t\right)$ and integrate the product over the unit cell Y

$$\int_Y \frac{\partial \sigma_{ij}^1\left(\mathbf{x},\mathbf{y},t+\Delta t\right)}{\partial y_j}\,\delta u_i^1\left(\mathbf{x},\mathbf{y},t+\Delta t\right)\mathrm{d}Y=0\ . \tag{4.24}$$

We then apply the product rule to yield

$$\begin{aligned}&\int_Y \left(\sigma_{ij}^1\left(\mathbf{x},\mathbf{y},t+\Delta t\right)\frac{\partial}{\partial y_j}\left(\delta u_i^1\left(\mathbf{x},\mathbf{y},t+\Delta t\right)\right)\right)\mathrm{d}Y\\ &=\int_Y \frac{\partial}{\partial y_j}\left(\sigma_{ij}^1\left(\mathbf{x},\mathbf{y},t+\Delta t\right)\delta u_i^1\left(\mathbf{x},\mathbf{y},t+\Delta t\right)\right)\mathrm{d}Y\end{aligned}\ . \tag{4.25}$$

By applying the divergence theorem to the term on the right-hand side, we produce

$$\begin{aligned}&\int_Y \left(\sigma_{ij}^1(\mathbf{x},\mathbf{y},t+\Delta t) \frac{\partial}{\partial y_j}\left(\delta u_i^1(\mathbf{x},\mathbf{y},t+\Delta t)\right)\right)\mathrm{d}Y \\ &= \int_{\partial Y+\Gamma} \left(\sigma_{ij}^1(\mathbf{x},\mathbf{y},t+\Delta t)\,\delta u_i^1(\mathbf{x},\mathbf{y},t+\Delta t)\,n_j\right)\mathrm{d}S\end{aligned} \quad . \tag{4.26}$$

Since the traction along the external boundary of the unit cell ∂Y is self canceling with the boundary traction of the adjacent cell, the integral along ∂Y in (4.26) will be zero.

To incrementalize (4.26), we must define the following:

$$\Delta\sigma_{ij}^1 \equiv \sigma_{ij}^1(\mathbf{x},\mathbf{y},t+\Delta t) - \sigma_{ij}^1(\mathbf{x},\mathbf{y},t) \tag{4.27}$$

$$\Delta e_{ij}^1 \equiv e_{ij}^1(\mathbf{x},\mathbf{y},t+\Delta t) - e_{ij}^1(\mathbf{x},\mathbf{y},t) \tag{4.28}$$

$$\Delta u_i^1 \equiv u_i^1(\mathbf{x},\mathbf{y},t+\Delta t) - u_i^1(\mathbf{x},\mathbf{y},t)\,. \tag{4.29}$$

Recognizing that $u_i^1(\mathbf{x},\mathbf{y},t)$ and $e_{ij}^1(\mathbf{x},\mathbf{y},t)$ are known values, we now substitute (4.27), (4.28), and (4.29) into (4.26). This action produces the following:

$$\int_Y \left(\left(\sigma_{ij}^1(\mathbf{x},\mathbf{y},t) + \Delta\sigma_{ij}^1\right)\Delta\delta e_{ij}^1\right)\mathrm{d}Y = \int_\Gamma \left(\sigma_{ij}^1(\mathbf{x},\mathbf{y},t+\Delta t)\,n_j\,\Delta\delta u_i^1\right)\mathrm{d}S \tag{4.30}$$

where the rearrangement of terms yields

$$\begin{aligned}\int_Y \left(\Delta\sigma_{ij}^1 \Delta\delta e_{ij}^1\right) \mathrm{d}Y = &\int_\Gamma \left(\sigma_{ij}^1(\mathbf{x},\mathbf{y},t)\, n_j\, \Delta\delta u_i^1\right) \mathrm{d}S \\ &+\int_\Gamma \left(\Delta\sigma_{ij}^1\, n_j\, \Delta\delta u_i^1\right) \mathrm{d}S \\ &-\int_Y \left(\sigma_{ij}^1(\mathbf{x},\mathbf{y},t)\, \Delta\delta e_{ij}^1\right) \mathrm{d}Y.\end{aligned} \tag{4.31}$$

We now introduce the incrementalized form of the local scale viscoelastic constitutive equation,

$$\Delta\sigma_{ij}^1 = C'_{ijkl}(\mathbf{y}) \cdot \left(\Delta\varepsilon_{kl}^0 + \Delta e_{kl}^1\right) \; + \; \Delta\sigma_{ij}^R \tag{4.32}$$

which was developed by Zocher, et al (1997). Placing (4.32) into (4.31) gives

$$\begin{aligned}&\int_Y \left(C'_{ijkl}(\mathbf{y}) \cdot \left(\Delta\varepsilon_{kl}^0 + \Delta e_{kl}^1\right) + \Delta\sigma_{ij}^R\right) \Delta\delta e_{ij}^1 \,\mathrm{d}Y = \int_\Gamma \left(\sigma_{ij}^1(\mathbf{x},\mathbf{y},t)\, n_j\, \Delta\delta u_i^1\right) \mathrm{d}S \\ &+\int_\Gamma \left(\left(C'_{ijkl}(\mathbf{y}) \cdot \left(\Delta\varepsilon_{kl}^0 + \Delta e_{kl}^1\right) + \Delta\sigma_{ij}^R\right) n_j\, \Delta\delta u_i^1\right) \mathrm{d}S \\ &-\int_Y \left(\sigma_{ij}^1(\mathbf{x},\mathbf{y},t)\, \Delta\delta e_{ij}^1\right) \mathrm{d}Y.\end{aligned} \tag{4.33}$$

After rearranging terms we achieve the following:

$$\begin{aligned}&\int_Y C'_{ijkl}(\mathbf{y})\, \Delta e_{kl}^1\, \Delta\delta e_{ij}^1 \,\mathrm{d}Y - \int_\Gamma C'_{ijkl}(\mathbf{y})\, \Delta e_{kl}^1\, n_j\, \Delta\delta u_i^1 \,\mathrm{d}S = \\ &\int_\Gamma \left(\sigma_{ij}^1(\mathbf{x},\mathbf{y},t)\, n_j\, \Delta\delta u_i^1\right) \mathrm{d}S + \int_\Gamma C'_{ijkl}(\mathbf{y})\, \Delta\varepsilon_{kl}^0\, n_j\, \Delta\delta u_i^1 \,\mathrm{d}S \\ &+\int_\Gamma \Delta\sigma_{ij}^R\, n_j\, \Delta\delta u_i^1 \,\mathrm{d}S - \int_Y \left(\sigma_{ij}^1(\mathbf{x},\mathbf{y},t)\, \Delta\delta e_{ij}^1\right) \mathrm{d}Y \\ &-\int_Y C'_{ijkl}(\mathbf{y})\, \Delta\varepsilon_{kl}^0 \Delta\delta e_{ij}^1 \,\mathrm{d}Y - \int_Y \Delta\sigma_{ij}^R\, \Delta\delta e_{ij}^1 \,\mathrm{d}Y\end{aligned} \tag{4.34}$$

which can be expressed in matrix notation as

$$\begin{aligned}
&\int_Y \left([D]\left[\Delta\delta u^1\right]\right)^T [C'][D]\left[\Delta u^1\right] \mathrm{d}Y - \int_\Gamma \left[\Delta\delta u^1\right]^T [C'][D]\left[\Delta u^1\right][n]\mathrm{d}S \\
&= \int_\Gamma \left[\Delta\delta u^1\right]^T \left[\sigma^1(\mathbf{x},\mathbf{y},t)\right][n]\mathrm{d}S \\
&- \int_{\partial Y} \left[\Delta\delta u^1\right]^T \left[C'_{ijkl}(\mathbf{y})\right]\left[\Delta\varepsilon^0_{kl}\right][n]\mathrm{d}S \\
&+ \int_\Gamma \left[\Delta\delta u^1\right]^T \left[\Delta\sigma^R\right][n]\mathrm{d}S \\
&- \int_Y \left([D]\left[\Delta\delta u^1\right]\right)^T \left[\sigma^1(\mathbf{x},\mathbf{y},t)\right]\mathrm{d}Y \\
&- \int_Y \left([D]\left[\Delta\delta u^1\right]\right)^T \left[\Delta\sigma^R\right]\mathrm{d}Y
\end{aligned} \tag{4.35}$$

where $[D]$ is the strain-displacement relations operator.

We now assume that the increment in the local displacement field over an element $\Delta\left(u_i^1\right)_h^e$ can be given in terms of the displacement increments $\Delta\left(u_i^1\right)_I^e$ at the element nodes I. This leads to the following relationship:

$$\Delta\left(u_i^1\right)_h^e = \sum_{I=1}^{N^e} \Delta\left(u_i^1\right)_I^e \psi_I^e(\mathbf{x},\mathbf{y},t) \tag{4.36}$$

where N^e is the number of interpolation functions $\psi_I^e(\mathbf{x},\mathbf{y},t)$.

Equation (4.36) can be represented in matrix notation as

$$\left[\Delta\left(u_i^1\right)_h^e\right] = \left[\psi^e(\mathbf{x},\mathbf{y},t)\right]\left[\Delta\left(u_i^1\right)^e\right]. \tag{4.37}$$

Substituting (4.37) into (4.35) yields

$$\begin{aligned}
&\int_{Y^e}\left(\left[B^e(\mathbf{x},\mathbf{y},t)\right]\left[\Delta\left(\delta u^1\right)^e\right]\right)^T\left[C'^e(\mathbf{y})\right]\left[B^e(\mathbf{x},\mathbf{y},t)\right]\left[\Delta\left(u^1\right)^e\right]\mathrm{d}Y\\
&-\int_{\Gamma^e}\left[\Delta\left(\delta u^1\right)^e\right]^T\left[C'^e(\mathbf{y})\right]\left[B^e(\mathbf{x},\mathbf{y},t)\right]\left[\Delta\left(u^1\right)^e\right]\left[\,n\,\right]\mathrm{d}S\\
=&\int_{\Gamma^e}\left[\Delta\left(\delta u^1\right)^e\right]^T\left[\sigma^1(\mathbf{x},\mathbf{y},t)\right]\left[\,n\,\right]\mathrm{d}S\\
&-\int_{\partial Y}\left[\Delta\left(\delta u^1\right)^e\right]^T\left[C'^e(\mathbf{y})\right]\left[\Delta\varepsilon^0_{kl}\right]\left[\,n\,\right]\mathrm{d}S\\
&+\int_{\Gamma^e}\left[\Delta\left(\delta u^1\right)^e\right]^T\left[\Delta\sigma^R\right]\left[\,n\,\right]\mathrm{d}S\\
&-\int_{Y^e}\left(\left[B^e(\mathbf{x},\mathbf{y},t)\right]\left[\Delta\left(\delta u^1\right)^e\right]\right)^T\left[\sigma^1(\mathbf{x},\mathbf{y},t)\right]\mathrm{d}Y\\
&-\int_{Y^e}\left(\left[B^e(\mathbf{x},\mathbf{y},t)\right]\left[\Delta\left(\delta u^1\right)^e\right]\right)^T\left[\Delta\sigma^R\right]\mathrm{d}Y
\end{aligned}\tag{4.38}$$

where

$$\left[B^e(\mathbf{x},\mathbf{y},\,t)\right]=\left[D\right]\left[\psi^e(\mathbf{x},\mathbf{y},t)\right]\tag{4.39}$$

Recognizing that $\Delta\left(\delta u_i^1\right)^e$ is an arbitrary function, (4.38) can be more simply stated as

$$\left[k^e(\mathbf{x},t)\right]=\left[f_1^e(\mathbf{x},t)\right]+\left[f_2^e(\mathbf{x},t)\right]+\left[f_3^e(\mathbf{x},t)\right]+\left[f_4^e(\mathbf{x},t)\right]+\left[f_5^e(\mathbf{x},t)\right]\tag{4.40}$$

where

$$\left[k^e(\mathbf{x},\mathbf{y},t)\right]=\int_{Y^e}\left[B^e(\mathbf{x},\mathbf{y},t)\right]^T\left[C'^e(\mathbf{y})\right]\left[B^e(\mathbf{x},\mathbf{y},t)\right]\mathrm{d}Y \tag{4.41}$$

$$\left[k^e_{cz}(\mathbf{x},\mathbf{y},t)\right]=\int_{\Gamma}\left[C'^e(\mathbf{y})\right]\left[B^e(\mathbf{x},\mathbf{y},t)\right][\,n\,]\mathrm{d}S \tag{4.42}$$

$$\left[f^e_1(\mathbf{x},\mathbf{y},t)\right]=\int_{\Gamma^e}\left[\psi^e(\mathbf{x},\mathbf{y},t)\right]^T\left[\sigma^1(\mathbf{x},\mathbf{y},t)\right][\,n\,]\mathrm{d}S \tag{4.43}$$

$$\left[f^e_2(\mathbf{x},\mathbf{y},t)\right]=-\int_{\partial Y}\left[\psi^e(\mathbf{x},\mathbf{y},t)\right]^T\left[C'^e(\mathbf{y})\right]\left[\Delta\varepsilon^0_{kl}\right][\,n\,]\mathrm{d}S \tag{4.44}$$

$$\left[f^e_3(\mathbf{x},\mathbf{y},t)\right]=\int_{\Gamma^e}\left[\psi^e(\mathbf{x},\mathbf{y},t)\right]^T\left[\Delta\sigma^R\right][\,n\,]\mathrm{d}S \tag{4.45}$$

$$\left[f^e_4(\mathbf{x},\mathbf{y},t)\right]=-\int_{Y^e}\left[B^e(\mathbf{x},\mathbf{y},t)\right]^T\left[\sigma^1(\mathbf{x},\mathbf{y},t)\right]\mathrm{d}Y \tag{4.46}$$

$$\left[f^e_5(\mathbf{x},\mathbf{y},t)\right]=-\int_{Y^e}\left[B^e(\mathbf{x},\mathbf{y},t)\right]^T\left[\Delta\sigma^R\right]\mathrm{d}Y\ . \tag{4.47}$$

In the above, $\left[k^e(\mathbf{x},\mathbf{y},t)\right]$ is the element stiffness matrix for bulk media; $\left[k^e_{cz}(\mathbf{x},\mathbf{y},t)\right]$ is the element stiffness matrix for cohesive elements; and $\left[f^e_1(\mathbf{x},\mathbf{y},t)\right]$, $\left[f^e_2(\mathbf{x},\mathbf{y},t)\right]$, $\left[f^e_3(\mathbf{x},\mathbf{y},t)\right]$, $\left[f^e_4(\mathbf{x},\mathbf{y},t)\right]$, and $\left[f^e_5(\mathbf{x},\mathbf{y},t)\right]$ are the contributions to the element load vector due to cohesive tractions at the beginning of the time step; the influence of the global scale strains; the change in the cohesive viscoelastic residual stress during the time step; to stresses at the beginning of the time step; and the change in the bulk viscoelastic residual stress during the time step, respectively.

Assembling the element stiffness matrices and load vectors yields

$$\left[K^1(\mathbf{x},t)\right]\left[\Delta u^1\right]=\left[F^1(\mathbf{x},t)\right] \tag{4.48}$$

where $\left[K^1(\mathbf{x},t)\right]$ is the stiffness matrix; $\left[\Delta u^1\right]$ is the displacement vector; and $\left[F^1(\mathbf{x},t)\right]$ is the force vector for the entire local scale problem.

4.3 Program Structure

The finite element formulations in this section have been implemented into a newly developed two-scale finite element program. This program, which has been written in FORTRAN, is represented schematically in Figure 4.1. From this schematic it can be seen that this code consists of two separate finite element algorithms: one that performs all global scale calculations based on (4.16) through (4.22); and another which performs all local scale calculations based on (4.40) through (4.48).

A multiscale analysis begins with the reading of the input information. The global scale information includes: 1) the mesh which defines the global scale geometry, 2) the mechanical properties associated with each global scale element, 3) which global scale elements are designated for multiscale analysis; 4) the loads and displacements applied to the global scale problem; and 5) and time stepping information which governs the rate of loading for the entire multiscale boundary value problem. -- for both global and local boundary value problems. The local scale information includes: 1) the mesh which defines the local scale geometry; and 2) the mechanical properties associated with each local scale element. In the current version of the code all local scale analyses begin with the same local scale geometry, material properties, and initial state.

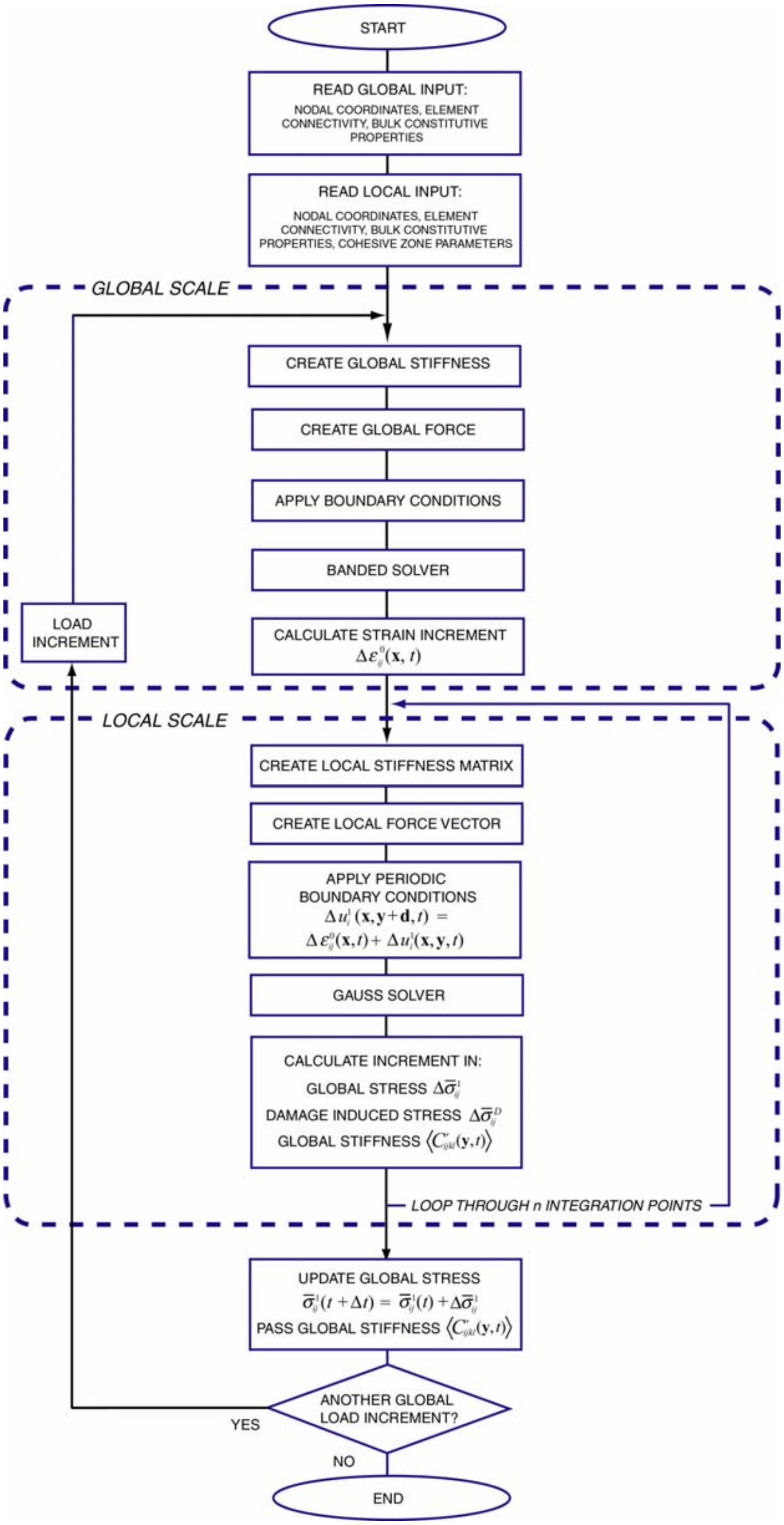

Figure 4.1. Flowchart for Multiscale Finite Element Algorithm.

A time stepping routine commences which governs the rate of loading for the entire multiscale problem. For the first time step t_1, the first task is to perform a finite element analysis on the global scale. This analysis will require the assembly of the global scale stiffness matrix $\left[K^0\left(t_1\right)\right]$ and force vector $\left[F^0\left(t_1\right)\right]$. After boundary conditions have been applied, the stiffness matrix and force vector are placed into a standard banded solver routine. This routine solves for the global scale displacements $u_i^0\left(\mathbf{x},t_1\right)$. From these displacements the global scale strains $\varepsilon_{ij}^0\left(\mathbf{x},t_1\right)$ are calculated. After this global scale strains have been calculated, a series of local scale analyses begins.

A local scale analysis is performed for every integration point within a global scale element that has been designated for multiscale analysis. This analysis will require the assembly of the local scale stiffness matrix $\left[K^1\left(\mathbf{x},\, t_1\right)\right]$ and force vector $\left[F^1\left(\mathbf{x},t_1\right)\right]$. As mentioned before, each local scale analysis begins with the same local scale geometry, material properties, and initial state. Each local analysis is unique, however, because each local scale boundary value problem receives a unique set of boundary conditions from the global scale strain. The global scale strain contribution to the force vector (4.44) can be converted into an equivalent condition for the local displacements $u_i^1\left(\mathbf{x},\mathbf{y},\, t_1\right)$ on the boundary on the local scale problem. The periodicity of the local displacement field at any time may now be expressed as

$$u_i^1\left(\mathbf{x},\mathbf{y}+\mathbf{d},\, t\right)=\varepsilon_{ij}^0\left(\mathbf{x},t\right)+\, u_i^1\left(\mathbf{x},\mathbf{y},\, t\right) \qquad \text{on } \partial Y \qquad (4.49)$$

where $\varepsilon_{ij}^0\left(\mathbf{x},t\right)$ are the strains from the corresponding global scale integration point. Since the multipoint constraints specified by (4.46) degrade the band structure of the local scale stiffness matrix $\left[K^1\left(\mathbf{x},t_1\right)\right]$, there are no advantages (and even a few disadvantages) to using a banded solver. Therefore, a standard Gaussian solver routine is used to calculate the local scale displacements. From this finite element analysis, local scale damage can be homogenized using (3.24) to produce the contribution to the global scale stress due to local scale damage $\Delta\bar{\sigma}_{ij}^{D}$.

Once this local scale procedure has been performed for one multiscale integration point, all local damage variables and viscoelastic residual terms are stored, and a new and independent local scale analysis is performed on a unit cell associated with the next global multiscale integration point. After all local scale analyses have been conducted for a particular time step, global scale damage information $\Delta\sigma_{ij}^{D}$, volume averaged residual stresses $\Delta\bar{\sigma}_{ij}^{R}$, and updated viscoelastic material properties $\bar{C}'_{ijkl}$ are passed back to the global algorithm where they will be used in the calculation of the of the global scale stress $\bar{\sigma}_{ij}^{1}\left(\mathbf{x}, t_1\right)$. At this point, the code will proceed with the global scale analysis for the next time step t_2. No user intervention is required during the program's execution. The program will terminate after all the user specified time steps have been executed.

5. EXAMPLE PROBLEMS

In this section, we shall demonstrate the ability of our finite element program to predict the multiscale response of heterogeneous elastic and viscoelastic bodies to various types of loading histories. For this demonstration, two test case types -- a tapered uniaxial bar and a thick-walled pressure vessel – have been selected. These classical types of boundary value problems were chosen specifically for their ability to produce gradients in the global scale stress field. When one considers the presence of evolving cracks on the smaller scales, these stress gradients will produce a similar spatial gradient in the effects of local scale damage. Therefore, with these test cases, we will be able to demonstrate the effects of local scale damage on the spatial distribution of the global stress field. To confirm the displacements calculated by our finite element program we have constructed quasi-analytic solutions which employ a fourth-order Runge-Kutta integration scheme.

5.1 Tapered Bar Problem

Consider the case of a uniaxial bar – ten inches in length and of unit depth -- which features a linearly varying cross-sectional area. The geometry for this tapered bar is depicted in Figure 5.1a. In this example, displacements in the x_1 - direction are restricted at the left end of the bar, while monotonically increasing displacements are imposed on the right end. These monotonically increasing displacements $\hat{u}_1(\mathbf{x},t)$ obey the following relationship

$$\hat{u}_1\left(x_1 = 10,\ x_2,\ x_3,\ t\right) = ctH\left(t\right) \tag{5.1}$$

where c has a value of 1.0×10^{-5} inches.

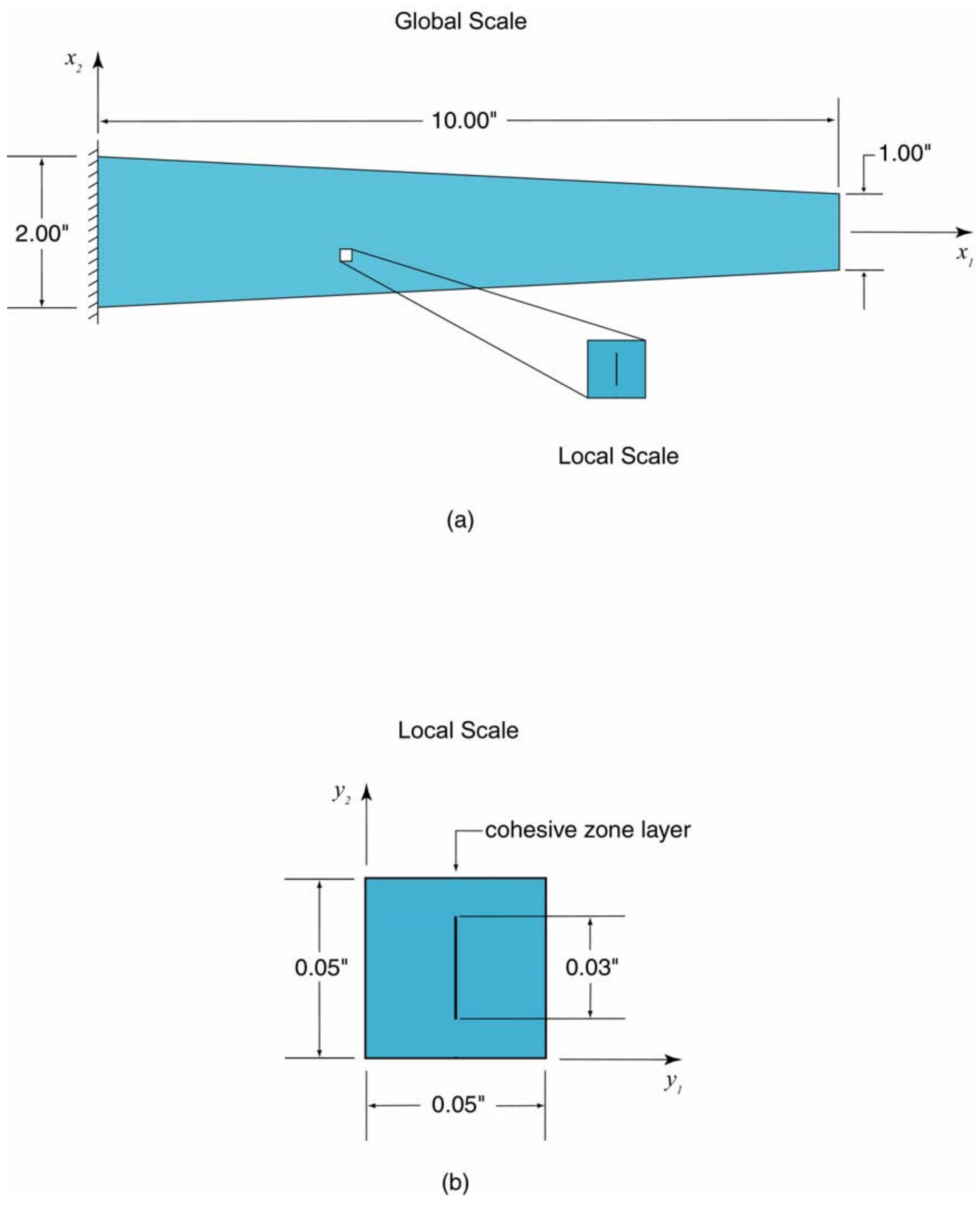

Figure 5.1. Tapered Bar Geometries and Dimensions.
(a) Global geometry (b) Local geometry.

At the local scale, this tapered bar exhibits a structure that is represented by the unit cell geometry depicted in Figure 5.1b. This 5.0×10^{-2} inch square unit cell features a 3.0×10^{-2} inch long crack that runs vertically along the cell's mid-plane. In the undeformed configuration, the crack faces are joined together by an infinitesimally thin layer of cohesive material are in complete contact. Under certain loading conditions, the crack faces can separate and the cohesive strength of the layer can weaken. This weakening of the cohesive material reflects the accumulation of microscale damage within the layer. This damage leads to the growth of the local scale crack within the unit cell. The large disparity in the dimensions of the global scale body and the local scale unit cell implies that within the tapered bar there exist millions of locations for smaller scale crack growth. Each of these sites is aligned perpendicularly with respect to the loading direction. We will use this problem to demonstrate how local scale crack growth influences the stress distribution on the global scale.

Symmetry along the axial centerline permits us to model only half of the global geometry. The resulting global scale finite element mesh is depicted in Figure 5.2a. In this figure it can be seen that the domain for the global scale problem was partitioned using forty constant strain triangles (CSTs). Every one of these forty CSTs has been designated as a *multiscale element*. Because of this designation, a separate local scale analysis will be conducted for every integration point within the global problem. Since all CSTs possess one integration point, which is physically located at the geometric center of the element, this tapered bar problem will require forty separate local scale analyses. In each of these analyses, local scale damage and its effect on the global scale stress field $\Delta\sigma_{ij}^{D}$ will be calculated. These effects will be passed back to the global scale finite element subroutine for the calculation of the global stresses.

The domain for each of the forty local scale problems was partitioned using 200 CSTs. In each unit cell, seven cohesive zone elements are used to join the two crack faces together. In their undeformed state at $t=0$, all forty of the local scale domains can be represented by the finite element mesh depicted in Figure 5.2b. After loading begins, each local scale problem evolves separately according to the global scale strain $\varepsilon_{ij}^{0}\left(\mathbf{x},\, t\right)$.

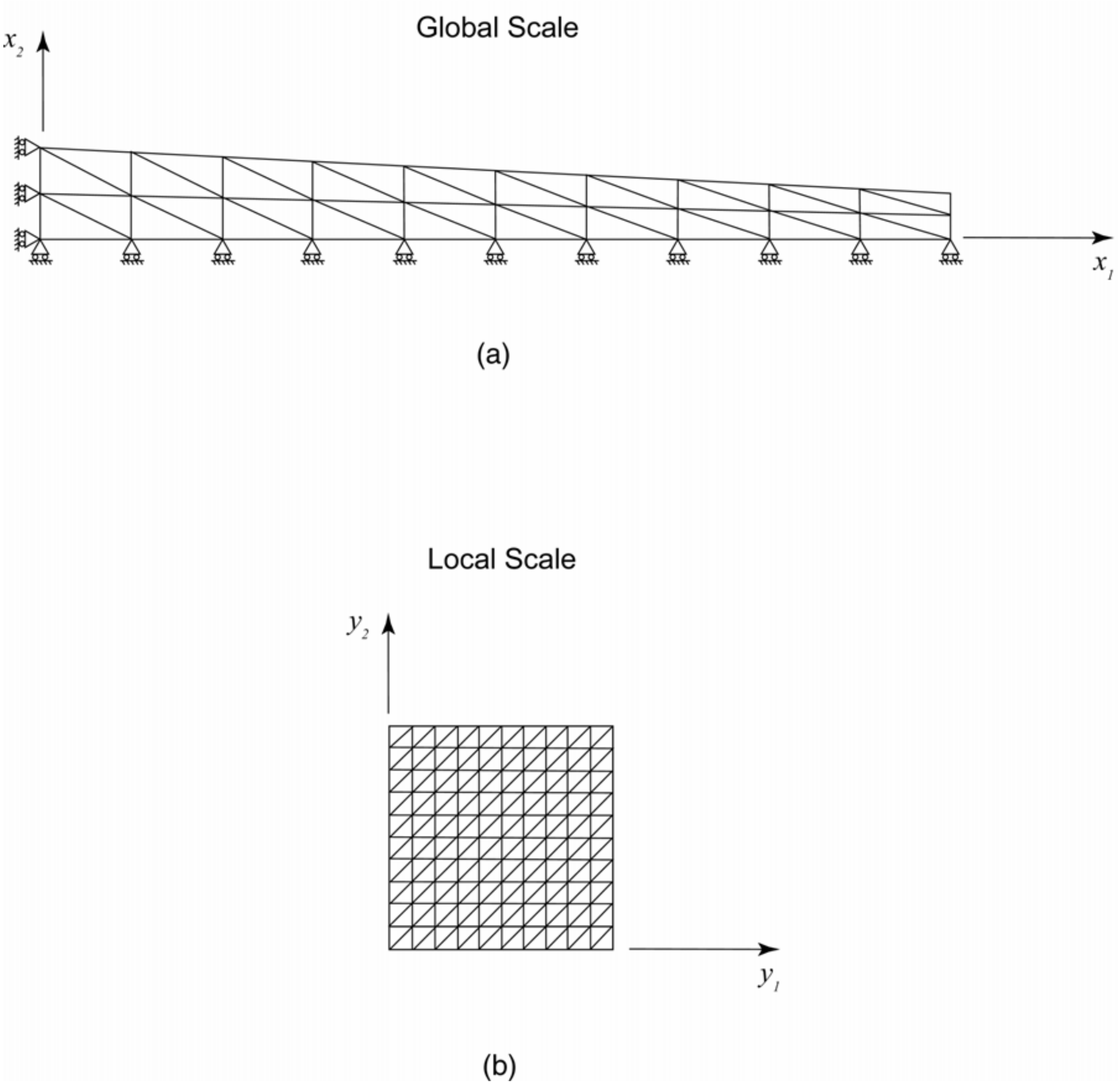

(a)

(b)

Figure 5.2. Tapered Bar Finite Element Meshes.
(a) Global mesh (b) Local Mesh

The property set for this elastic tapered bar problem is presented in Table 5.1. This set of properties describes a hypothetical material system, which was designed specifically for this demonstration. The initial properties of the global medium as well as the properties of bulk medium at the local scale are assumed to be isotropic linear elastic. We emphasize that after the first time step, all global scale CSTs are endowed with the updated stiffnesses taken from their respective local scale analysis.

Table 5.1 Material Properties for Elastic Tapered Bar Problem.

Global*			**Local**					
Bulk Properties			**Bulk Properties**			**Cohesive Zone Properties**		
E	1.00E+06	(psi)	E	1.00E+06	(psi)	E	1.00E+06	(psi)
ν	0.0	(--)	ν	0.0	(--)	ν	0.45	(--)
						δ_n	1.00E-01	(in.)
						δ_t	1.00E-01	(in.)
						m	1.00E-03	(in.)
						s	2.00E-04	(in.)
						r_{cr}	1.00E-04	(in.)

* Global properties are necessary for first time step only

The entire displacement history described by (5.1) is illustrated in Figure 5.3. The time increment Δt chosen for this problem is 1.0×10^0 second.

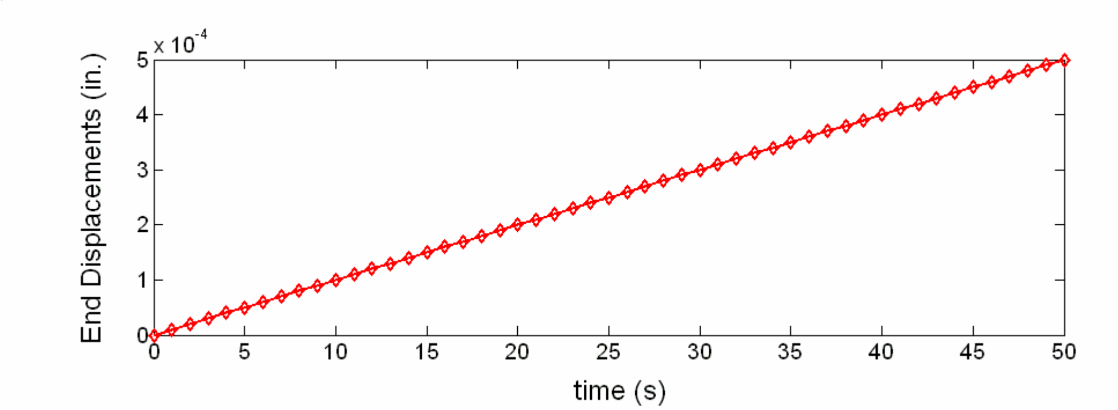

Figure 5.3 Loading History for Tapered Bar Problem.

Three plane stress analyses were conducted for this demonstration. The first was strictly a global scale analysis with no consideration for multiscale effects. The stress distribution predicted by this analysis serves as our baseline when assessing multiscale results. In the second analysis, multiscale effects were considered; however, the cohesive zone properties in this analysis were modified so as to prevent the development of local scale damage. Specifically, the cohesive zone modulus was increased to 1.0×10^{10} psi (which inhibits the possibility of crack opening displacements); the cohesive zone Poisson's ratio was decreased to 0.0 (which prevents the accumulation of damage); and the critical fibril radius r_{cr} was given a negative value (which ensures that there is no initial state of damage in the cohesive zone). By performing a multiscale analysis that features these three modifications, we hoped to recover the same stress distribution predicted by the first analysis where no multiscale effects are modeled. Indeed, we were able to recover the stress distribution predicted by the first analysis as evidenced by Figure 5.4. In this figure, the axial stress distributions for both the first and second analyses are depicted for selected times during their loading histories. The circles indicate the value of the stress calculated at each global integration point. The lines are fourth order polynomial curve fits of the calculated stresses. At each time step, the stress distributions are identical. Thus, by recovering the non-multiscaling solution, we can conclude that the multiscale model treats the non-multiscaling problem as a special case..

In the third elastic tapered bar analysis multiscale effects are considered without any modification to the material set listed in Table 5.1. As a result, local scale damage was permitted to initiate and grow. Figure 5.5 provides a direct comparison between the stress evolution of the tapered bar without local scale damage and then with local scale damage. The stress distributions for these two analyses remain similar after ten seconds has passed; however, a noticeable difference exists between the two distributions at the twenty second mark. By this time, local scale damage has accumulated at the right end of the bar where the cross-sectional area is at its minimum. As a result, the axial stress at the right end is 21.5 psi in the multiscaling case while it is 26.5 psi in the non-multiscaling case. After forty seconds, the local scale damage has diminished the global stress distribution along the entire length of the bar. This difference only becomes more pronounced at later time steps.

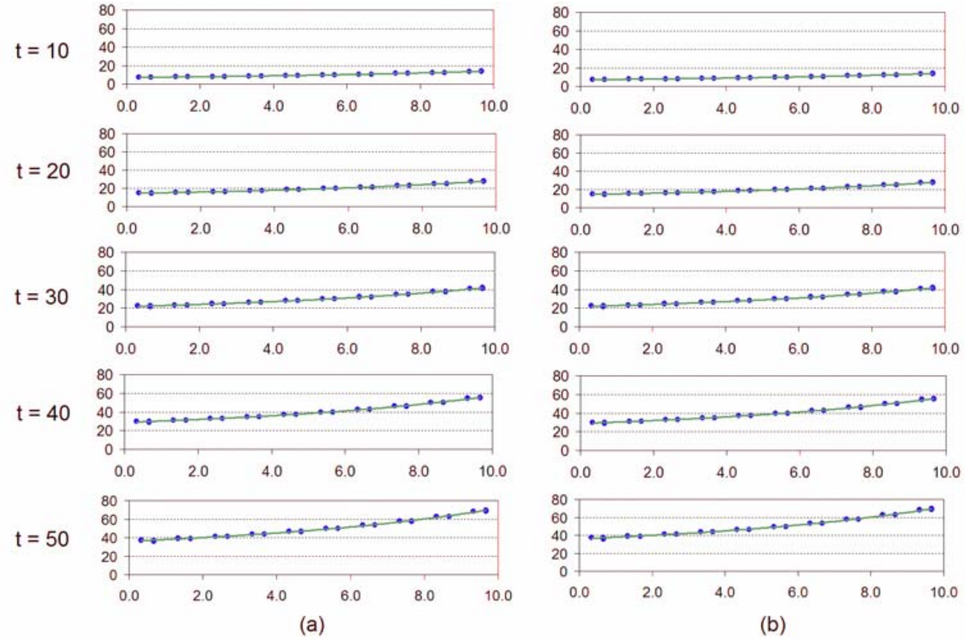

Figure 5.4 Tapered Bar Comparison I.
(a) Axial Stress Distribution for Elastic Tapered Bar without Multiscaling (psi)
(b) Axial Stress Distribution for Elastic Tapered Bar with Cohesive Zones Closed (psi).

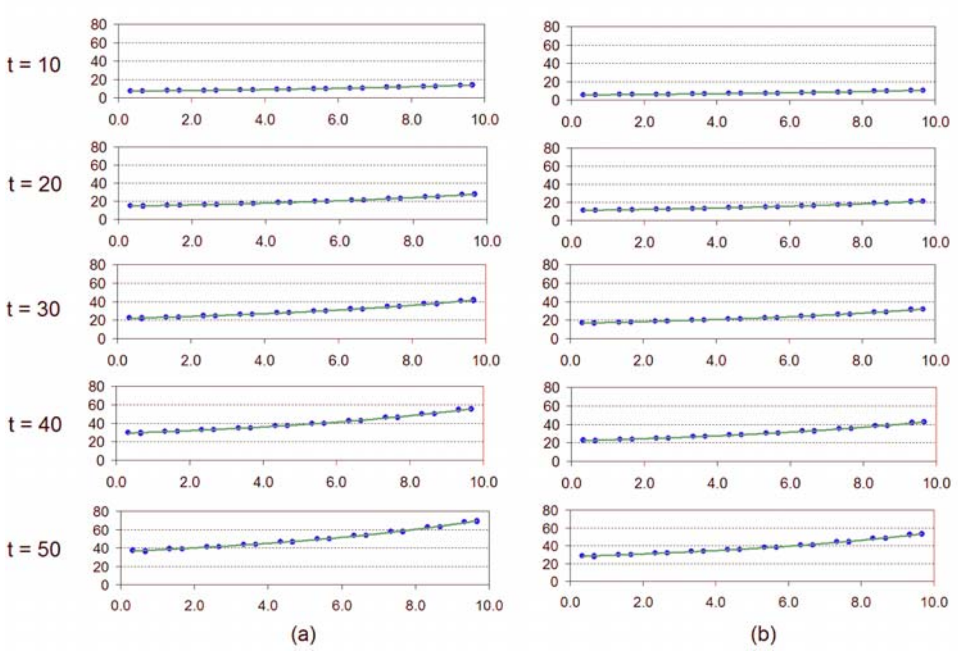

Figure 5.5 Tapered Bar Comparison II.
(a) Axial Stress Distribution for Elastic Tapered Bar with No Multiscaling (psi)
(b) Axial Stress Distribution for Elastic Tapered Bar with Cohesive Zones Free to Open (psi).

To illustrate what is happening on the local scale for the elastic tapered bar where cohesive zones are free to open, we have chronicled the deformations of three unit cells positioned at three different locations within the tapered bar. These unit cells and their corresponding global scale elements within the tapered bar mesh are depicted in Figure 5.6. Unit cell A corresponds with the global scale integration point located at $x_1 = 1.33$ in.; unit cell B corresponds with the global scale integration point located at $x_1 = 5.33$ in.; and, unit cell C corresponds with the global scale integration point located at $x_1 = 9.33$ in. Snapshots of these three unit cells are shown in ten second increments up until the total loading time of fifty seconds. Local scale displacements have been magnified 100 times to make the deformations in each unit cell more visible in the figure.

After twenty seconds, there appears to be no difference in the deformation of the three unit cells. However by thirty seconds, unit cell C exhibits the first visible signs of cohesive zones opening. Since the integration point associated with unit cell C is located 0.66 in. from the loading end of the tapered bar, it is reasonable to expect this unit cell to be the first to show signs of crack growth. The cross-sectional area of the tapered bar is the smallest at this end, and consequently, the axial stresses within the tapered bar are the largest at this end. In this example problem, the stresses at this end are even greater because of multiscale effects. Local scale cracks, which are beginning to develop at this end, produce a noticeable increase in the stresses at this end. This phenomenon is shown in Figure 5.5b.

As the imposed displacements on the global scale continue to increase, damage begins to form in unit cells A and B. After forty seconds, unit cells A and B show their first visible signs of crack development. Meanwhile, the crack opening displacements in unit cell C continue to increase.

The cracks that form and develop in unit cells A, B, and C all act as stress raisers which increase the global stress levels within tapered bar at their respective global scale integration points.

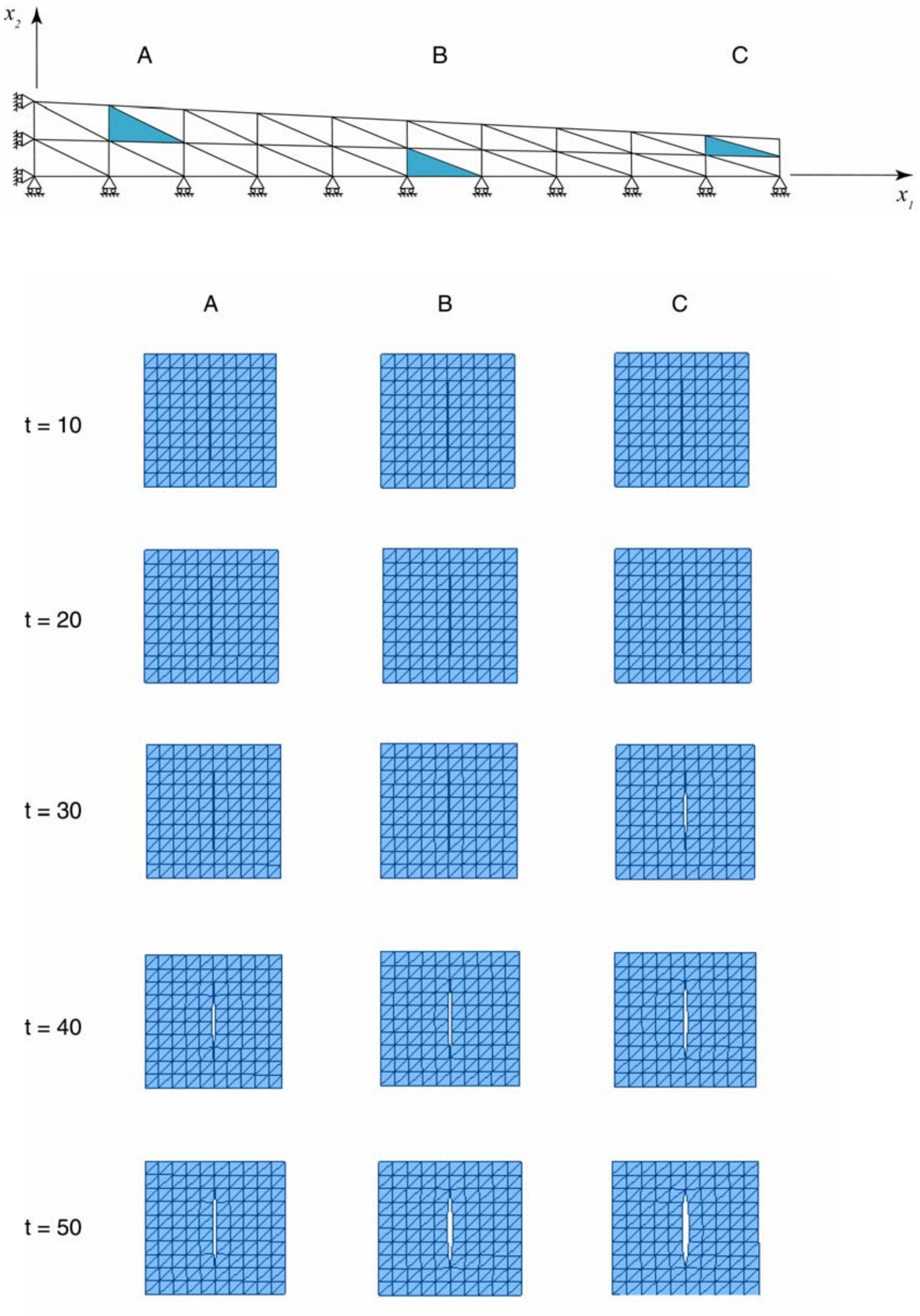

Figure 5.6 Local Scale Deformations for Elastic Tapered Bar.

Two more tapered bar analyses were performed; each of these analyses featured the viscoelastic property set presented in Table 5.2. The initial properties of the global medium as well as the properties of bulk medium at the local scale are assumed to be isotropic linear viscoelastic. The uniaxial relaxation modulus for the bulk media and the cohesive zone model are represented by a standard linear solid, where the relaxation modulus $E(t)$ may be represented by the following relationship

$$E(t) = E_\infty + E_1 \exp\left(-E_1 t / \eta_1\right) \tag{5.2}$$

where E_∞ is a constant-valued linear elastic spring coefficient which represents the long-time value of the relaxation modulus, E_1 is a constant-valued Hookean spring constant, and η_1 is a constant-valued Newtonian dashpot coefficient. The viscoelastic properties listed in Table 5.2 were designed so that the initial value of the relaxation modulus would be identical to the value of modulus of elasticity found in Table 5.1. Also, the dashpot coefficient was chosen so that viscoelastic relaxation would be evident within the tapered bar during the time of loading. Therefore, the properties listed in Table 5.2 allow us to make a direct comparison between the elastic and viscoelastic tapered bar problems.

Table 5.2 Material Properties for Viscoelastic Tapered Bar Problem.

Global*			**Local**					
Bulk Properties			**Bulk Properties**			**Cohesive Zone Properties**		
E_∞	5.00E+05	(psi)	E_∞	5.00E+05	(psi)	E_∞	5.00E+05	(psi)
E_1	5.00E+05	(psi)	E_1	5.00E+05	(psi)	E_1	5.00E+05	(psi)
η_1	5.00E+06	(psi-s)	η_1	5.00E+06	(psi-s)	η_1	5.00E+06	(psi-s)
ν	0.0	(--)	ν	0.0	(--)	ν	0.45	(--)
						δ_n	1.00E-01	(in.)
						δ_t	1.00E-01	(in.)
						m	1.00E-03	(in.)
						s	2.00E-04	(in.)
						r_{cr}	1.00E-04	(in.)

* Global properties are necessary for first time step only

The first viscoelastic tapered bar problem was strictly a global scale analysis with no consideration for multiscale effects. In Figure 5.7 we present the axial stress distribution predicted by this analysis as well as the stress distribution predicted for the elastic tapered bar with no multiscale effects. As expected, the two tapered bars initially display identical stress distributions. However, after thirty seconds, relaxation effects have clearly overtaken the stress response of the right end of the viscoelastic tapered bar. The effects of viscoelastic relaxation become even more pronounced with increasing end displacements so that after fifty seconds the entire stress distribution of the bar has been affected.

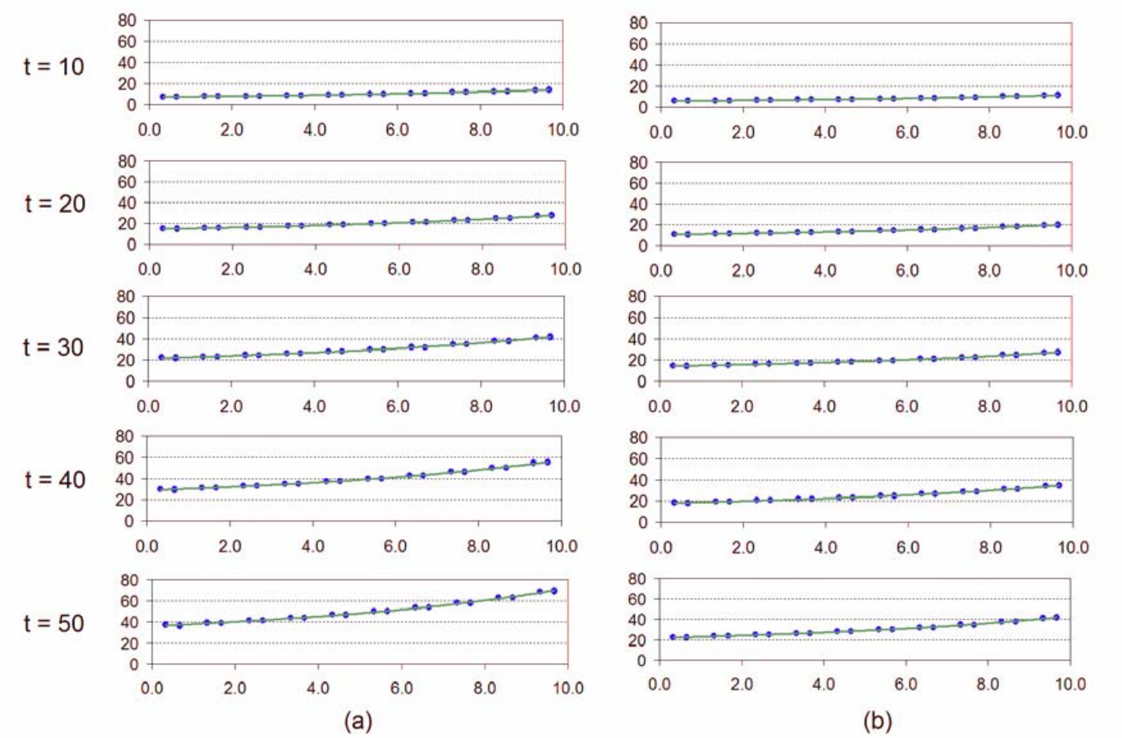

Figure 5.7 Tapered Bar Comparison III.
(a) Axial Stress Distribution for Elastic Tapered Bar with No Multiscaling (psi)
(b) Axial Stress Distribution for Viscoelastic Tapered Bar with No Multiscaling (psi).

The second viscoelastic tapered bar problem does account for local scale damage. In Figure 5.8 we present the axial stress distribution calculated for the viscoelastic tapered bar without multiscale damage as well as the stress distribution calculated for the viscoelastic tapered bar with multiscale damage. Again, as expected, the two tapered bars initially display identical stress distributions. However, after thirty seconds, damage effects have clearly overtaken the stress response of the right end of the viscoelastic tapered bar with multiscaling. After fifty seconds, the end of the tapered bar with no multiscale effects has an axial stress of 44.5 psi, while the end of the tapered bar with multiscale effects has an axial stress of 27.2 psi.

A comparison of the stress levels in Figures 5.5b and 5.8b emphasizes how local scale damage and viscoelastic relaxation both affect the global scale stress response $\bar{\sigma}^1_{ij}(\mathbf{x}, t)$. In both cases -- elastic and viscoelastic tapered bars with local scale damage -- the presence of local scale cracks reduces the axial stresses that occur within the tapered bar. Similarly, viscoelastic relaxation causes a reduction the axial stresses that occur on the global scale.

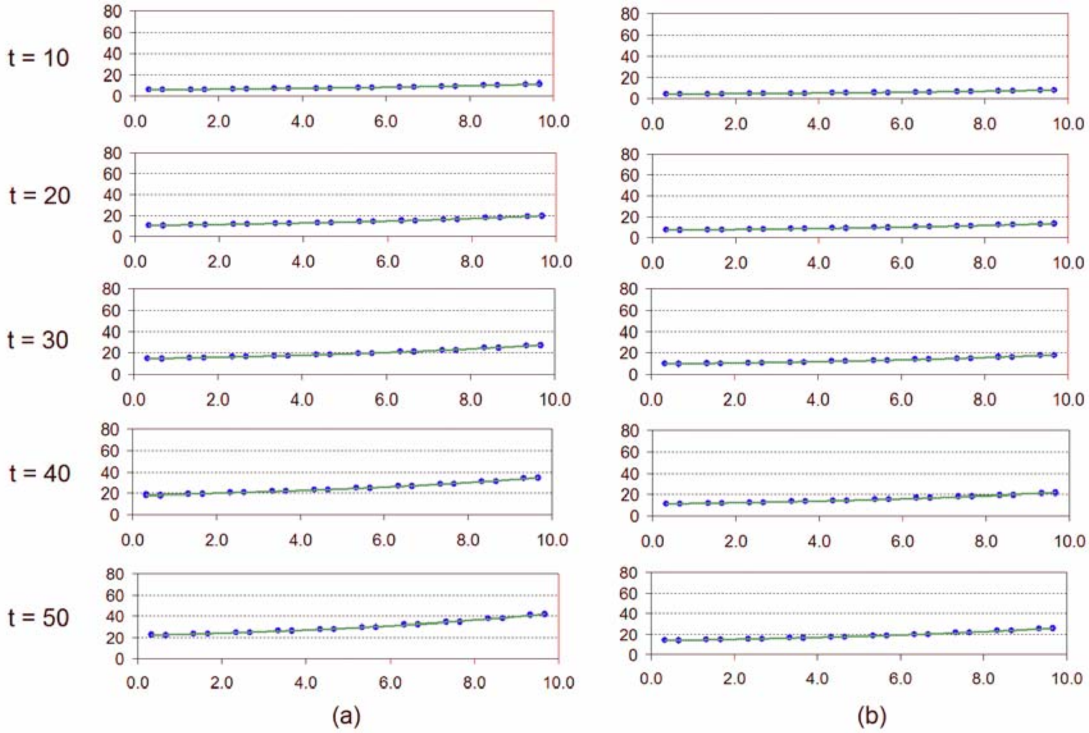

Figure 5.8 Tapered Bar Comparison IV.
(a) Axial Stress Distribution for Viscoelastic Tapered Bar with No Multiscaling (psi)
(b) Axial Stress Distribution for Viscoelastic Tapered Bar with Cohesive Zones Free to Open (psi).

As a way to compare and summarize the results of all four of the tapered bar analyses, Figure 5.9 illustrates the stress distributions of the four tapered bar problems. Finite element predictions for the elastic and viscoelastic tapered bar problems without damage compare well with their corresponding analytic solutions. This illustrates the stress relaxation caused by both viscoelastic and damage effects.

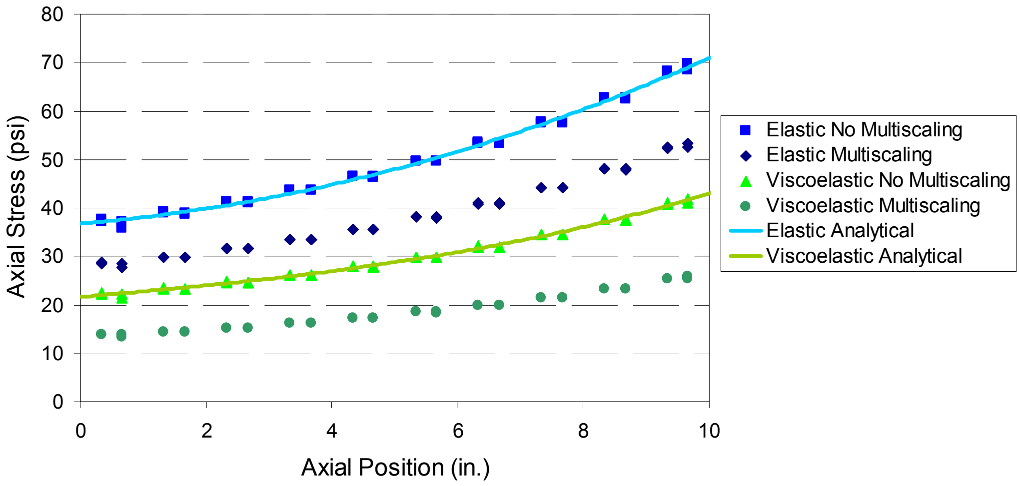

Figure 5.9 Summary of Tapered Bar Problems: Axial Stresses at t = 50 s.

A convergence study was performed to determine the necessary size of the size of the time step for the tapered bar analysis. Figure 5.10 shows three stress distributions for the viscoelastic tapered bar with multiscale damage. Each distribution was calculated using a different increment in time Δt: 0.1, 1.0, and 10.0 seconds. A less than 2% difference exists between the 0.1 ans 1.0-second time step; therefore a 1.0-second time step was deemed as acceptable for this demonstration.

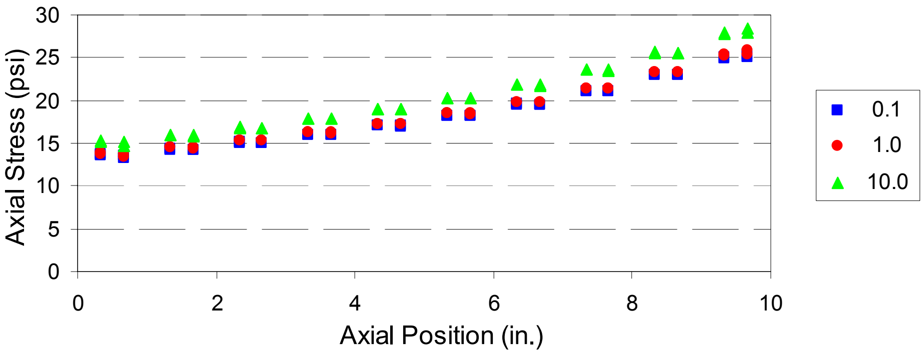

Figure 5.10 Time Step Convergence Study for Tapered Bar Problem.

With the addition of local scale damage, no closed-form analytical solution exists for the elastic tapered bar problem. Therefore, in order to confirm the validity of our finite element solution, we have constructed a quasi-analytic model for comparison. To form this model we start with the ordinary differential equation governing this problem

$$\frac{d}{dx_1}\left(EA\left(x_1\right)\left(\frac{du_1^0\left(x_1,t\right)}{dx_1}\right)\right)+\frac{d}{dx_1}\left(A\left(x_1\right)\sigma_{11}^D\left(x_1,t\right)\right)=0 \qquad \text{for } 0 \le x_1 \le 10 \qquad (5.3)$$

We have placed this differential equation into a fourth-order Runge Kutta integration scheme. To perform integration on (5.3), we supplied: the constant valued modulus of elasticity E; the equation for the cross-sectional area $A\left(x_1\right)$; a curve-fit of the damage induced stresses $\sigma_{11}^D\left(x_1,t\right)$ for a specific time t; and values for the displacement $u_1^0\left(x_1,t\right)$ and strain $\varepsilon_{11}^0\left(x_1,t\right)$ at $x_1=0$. From this quasi-analytic solution, we shall be able to recover the displacements calculated by our finite element code.

In the examples presented earlier, $\sigma_{11}^D\left(x_1,t\right)$ is an almost linear function which increases with respect to the axial position x_1. Its product with the linearly decreasing cross-sectional area $A\left(x_1\right)$ yields a nearly constant-valued function that has a spatial derivative close to zero. Because of this fact, the global displacements in the previous examples demonstrate a weak dependence on the local scale damage – too weak to illustrate the effect local damage has on the global displacements. To overcome this obstacle, we have constructed a power law type damage equation that varies with respect to position x_1. This damage equation is

$$\sigma_{11}^D\left(x_1,t\right) = -1.5\left(1-\frac{x_1}{10}\right)^3 \qquad (5.4)$$

It is important to note that this law is not physically-based. This law is merely designed to yield a noticeable effect in the global displacements for the purpose of checking the finite element program. All loading, geometry, and material properties remain the same as those used in the previous elastic tapered bar problem with local scale damage.

Figure 5.11 shows the distribution of the damage induced stresses $\sigma_{11}^{D}\left(x_1,t\right)$ calculated by our multiscale finite element program after 25 seconds.

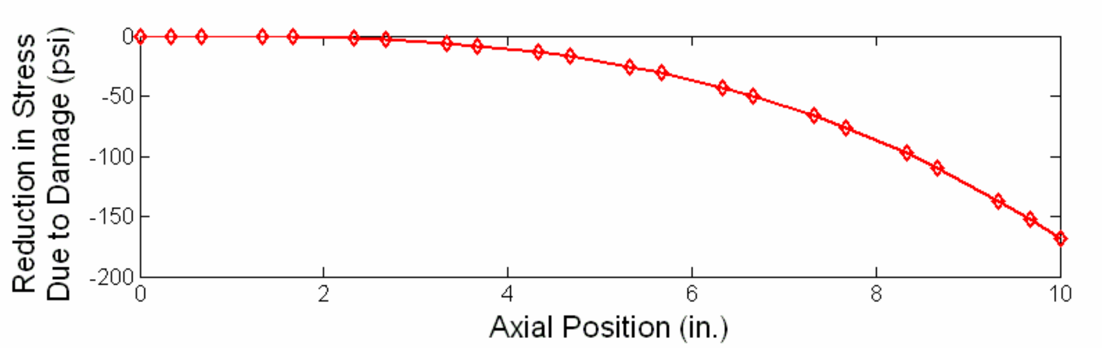

Figure 5.11 Contributions to Axial Stress Made by Local Scale Damage.

Runge Kutta was used to calculate the displacements for the elastic tapered bar. These displacements are shown in Figure 5.12. From this figure it can be seen that the values calculated by the quasi-analytical solution and by the multiscale finite element program are in close agreement.

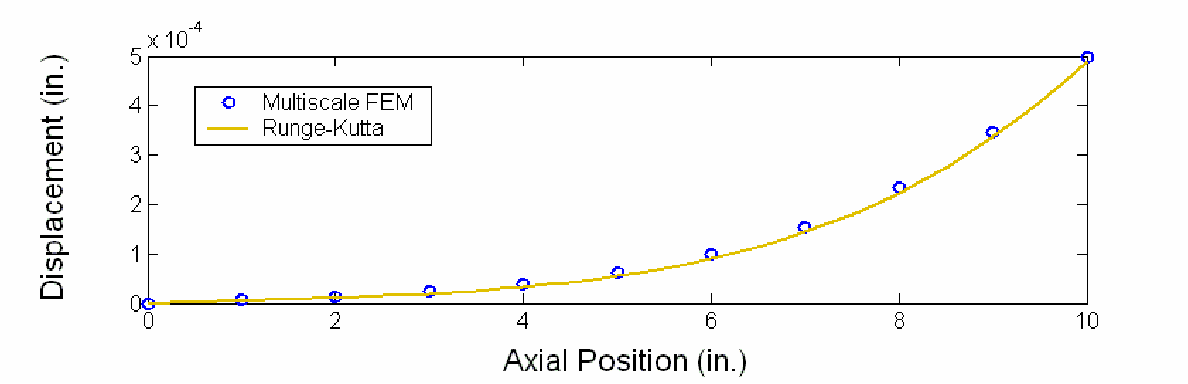

Figure 5.12 Comparison of Quasi-Analytical Solution and Finite Element Program I.

5.2 Thick-Walled Pressure Vessel Problem

We now consider the case of a thick-walled pressure vessel with an internal radius of 1.0 inch and an external radius of 2.0 inches. The geometry for this pressure vessel is depicted in Figure 5.13a. In this example, monotonically increasing radial displacements $\hat{u}_r\left(R,\varTheta,t\right)$ are imposed on internal boundary of the pressure vessel. These monotonically increasing displacements obey the following relationship

$$\hat{u}_r\left(R=1.0,\ \varTheta,\ t\right)=c\,t\,H\left(t\right) \tag{5.5}$$

where c has a value of 5.0×10^{-6} inches.

At the local scale, this pressure vessel exhibits a structure which is represented by the unit cell depicted in Figure 5.13b. This unit cell features a 1.6×10^{-2} inch diameter cylindrical inclusion embedded in a 2.0×10^{-2} inch square of matrix material. In the following pressure vessel analyses, the inclusion and the binder are endowed with identical mechanical properties. In the undeformed configuration, an infinitesimally thin layer of cohesive material binds the inclusion to the surrounding medium. Under certain loading conditions, this layer of cohesive material can weaken and eventually fail, which leads to the formation and growth of a local scale crack between the inclusion and the matrix. The large disparity in the dimensions of the global scale body and the local scale unit cell implies that within the pressure vessel there exist thousands of inclusions – all of which are potential sites for local scale crack growth. We will use this pressure vessel problem to demonstrate how smaller scale crack growth influences the stress distribution on the global scale.

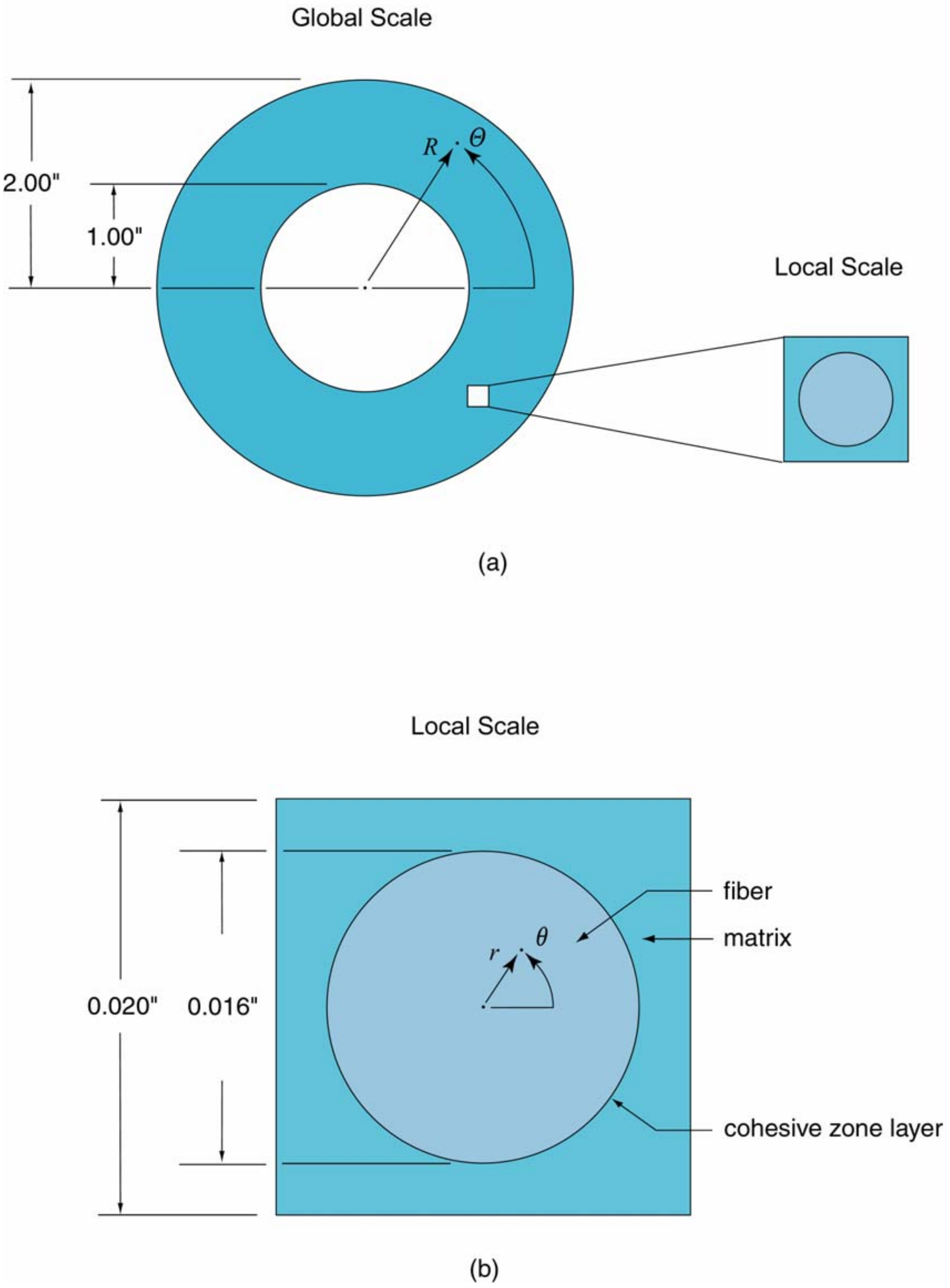

Figure 5.13 Geometries and Dimensions for Thick-Walled Pressure Vessel Problem.
(a) Global geometry (b) Local geometry.

The pressure vessel geometry possesses infinite symmetry about its axis. By exploiting two planes of symmetry, we choose to model only one fourth of the global geometry. The resulting global scale finite element mesh is depicted in Figure 5.14a. In this figure it can be seen that the domain for the global scale problem was partitioned using 200 CSTs. Every one of these 200 CSTs has been designated as a multiscale element.

The domain for each of the 200 local scale problems was partitioned using 288 CSTs. In each unit cell, thirty-two cohesive zone elements are used to join the fiber with surrounding matrix material. In their undeformed state at $t = 0$, all 200 of the local scale domains can be represented by the finite element mesh depicted in Figure 5.14b. After loading begins, each local scale problem evolves separately according to the global scale strains, which in cylindrical coordinates are represented as $\varepsilon^0_{RR}\left(R, t\right)$, $\varepsilon^0_{\Theta\Theta}\left(R, t\right)$, and $\varepsilon^0_{R\Theta}\left(R, t\right)$.

The property set for this elastic pressure vessel analysis is presented in Table 5.3. This set of properties describes a hypothetical material system, which was designed for this demonstration. The initial properties of the global medium as well as the properties of bulk medium at the local scale are assumed to be isotropic linear elastic. Again, we emphasize that after the first timestep, all global scale CSTs are endowed with the updated stiffness taken from their respective local scale analysis.

Table 5.3 Material Properties for Elastic Thick-Walled Pressure Vessel Problem.

Global*			**Local**					
Bulk Properties			**Bulk Properties**			**Cohesive Zone Properties**		
E	*1.00E+06*	(psi)	E	*1.00E+06*	(psi)	E	*1.00E+06*	(psi)
ν	*0.0*	(--)	ν	*0.0*	(--)	ν	*0.45*	(--)
						δ_n	*5.00E-04*	(in.)
						δ_t	*5.00E-04*	(in.)
						m	*1.00E-03*	(in.)
						s	*2.00E-04*	(in.)
						r_{cr}	*1.00E-04*	(in.)

* Global properties are necessary for first time step only

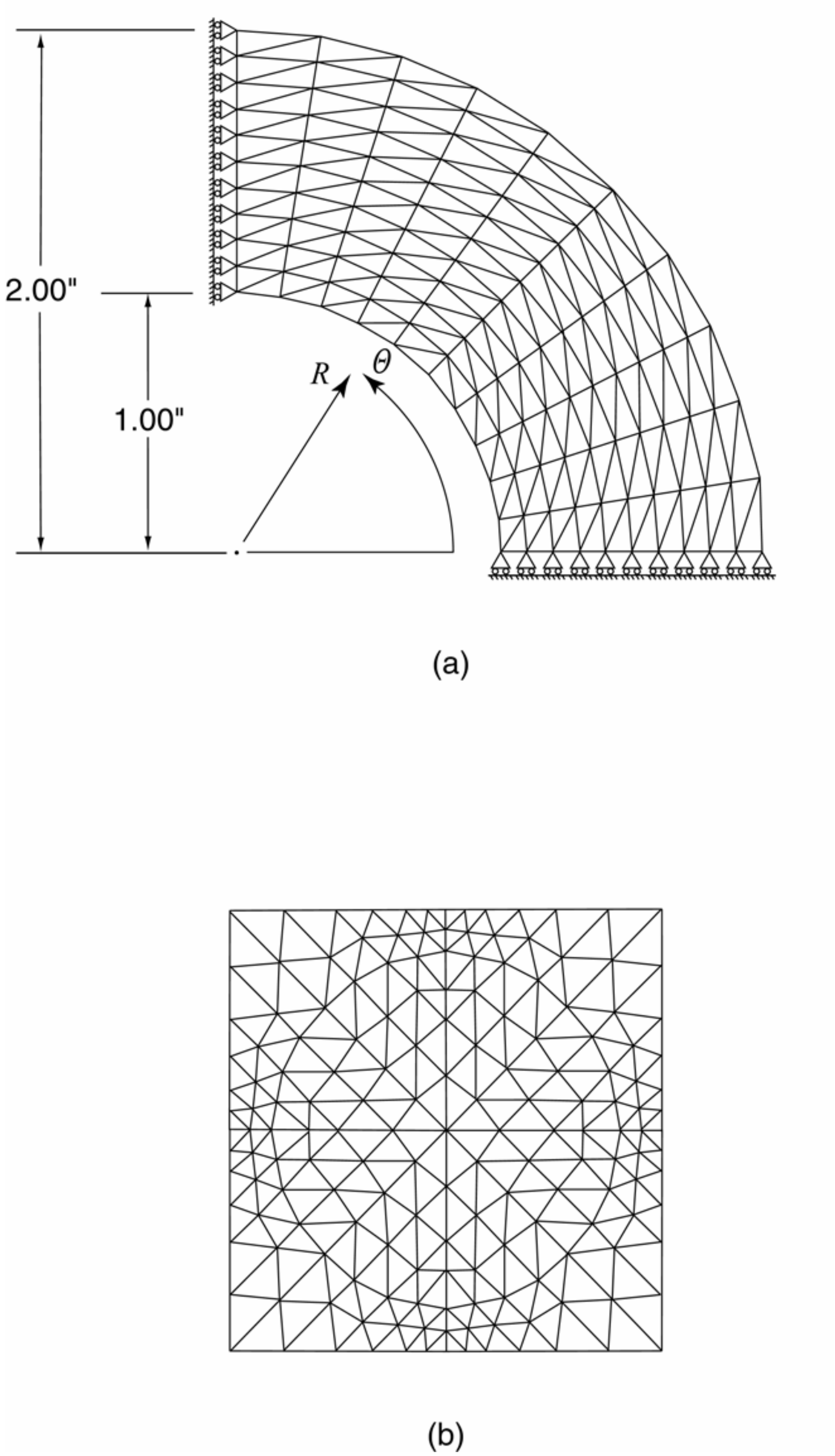

Figure 5.14 Thick-Walled Pressure Vessel Finite Element Meshes.
(a) Global mesh (b) Local Mesh .

The property set for this elastic pressure vessel analysis is presented in Table 5.3. This set of properties describes a hypothetical material system, which was designed for this demonstration. The initial properties of the global medium as well as the properties of bulk medium at the local scale are assumed to be isotropic linear elastic. Again, we emphasize that after the first time step, all global scale CSTs are endowed with the updated stiffness taken from their respective local scale analysis.

The entire ramp displacement history as described by (5.5) is illustrated in Figure 5.15. The time increment Δt chosen for this problem is 1.0 second.

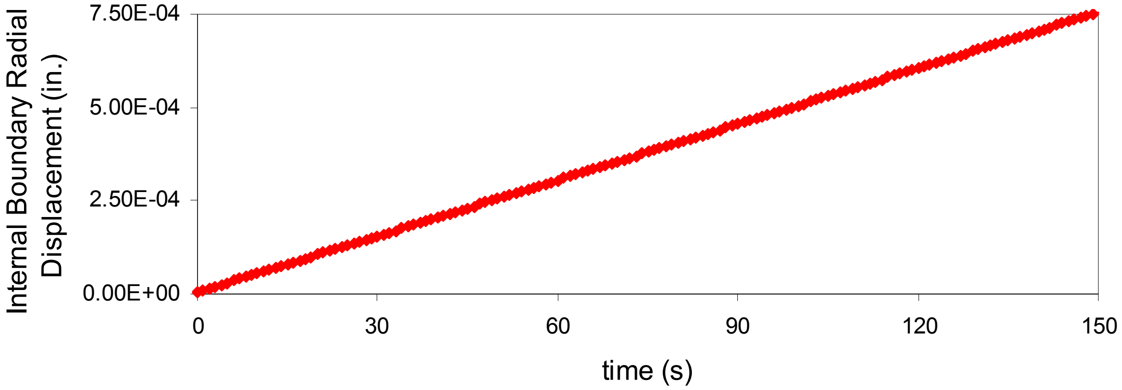

Figure 5.15 Displacements along Internal Boundary of Thick-Walled Pressure Vessel.

Two plane strain analyses were conducted for this demonstration. The first is strictly a global scale analysis with no consideration for local scale damage. The stress distribution predicted by this analysis serves as our baseline when assessing multiscale results. The second analysis includes multiscale effects where local scale cracks are permitted to initiate and grow. Figure 5.16 provides a direct comparison between the tangential stress distribution of the pressure vessel analysis without local scale damage and the corresponding pressure vessel analysis with local scale damage. Figure 5.17 provides a similar comparison between radial stress distributions of the two analyses. In these figures, the stress distributions for both the first and second analyses are depicted for selected times during their loading histories. The circles indicate the value of the stress calculated at each global integration point. The lines are fourth order polynomial curve fits of the calculated stresses.

The stress distributions for these analyses remain similar even after sixty seconds has passed; however, a clear difference exists between the two distributions at the ninety-second mark. By this time, local scale damage has accumulated along the interior boundary of the pressure vessel where the montonically increasing displacements are imposed. As expected, the magnitudes of both the tangential and radial stresses near the internal boundary are reduced in the multiscaling case than in the non-multiscaling case. Meanwhile, near the external boundary of the pressure vessel, the effects of local scale damage have yet to make a noticeable contribution to the stresses.

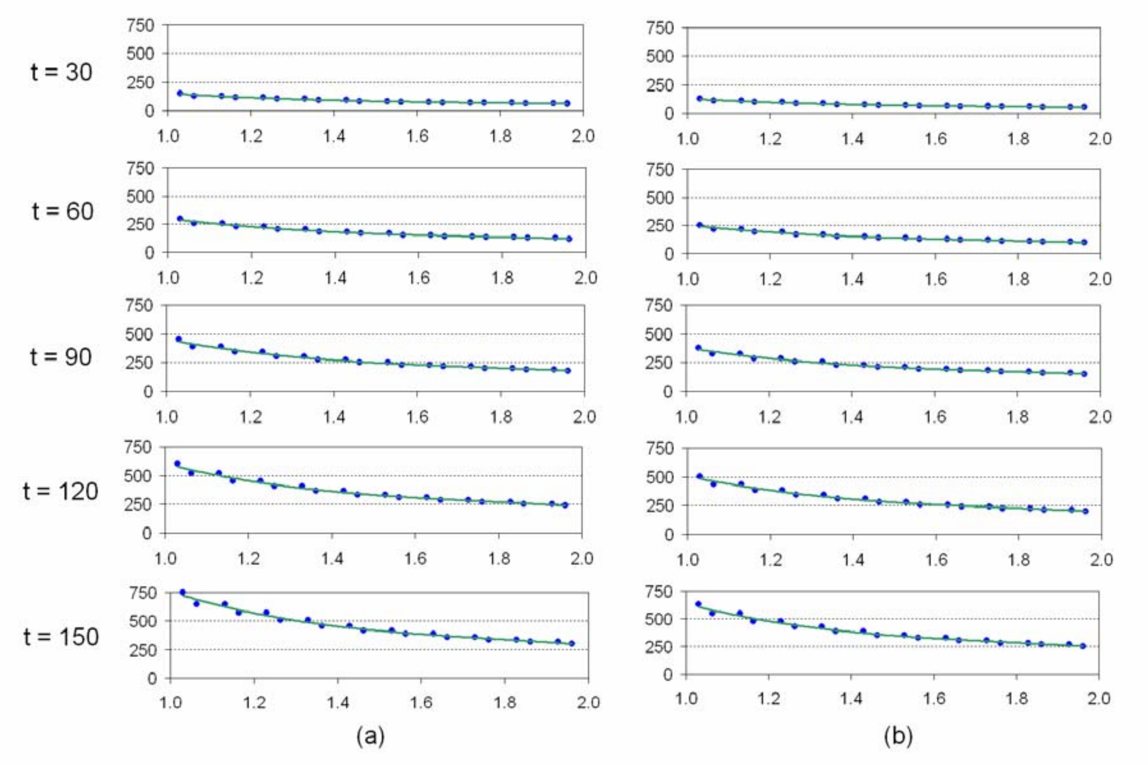

Figure 5.16 Elastic Pressure Vessel Comparison I.
(a) Tangential Stress vs. Radial Position for No Multiscaling (psi)
(b) Tangential Stress vs. Radial Position with Cohesive Zones Free to Open (psi)

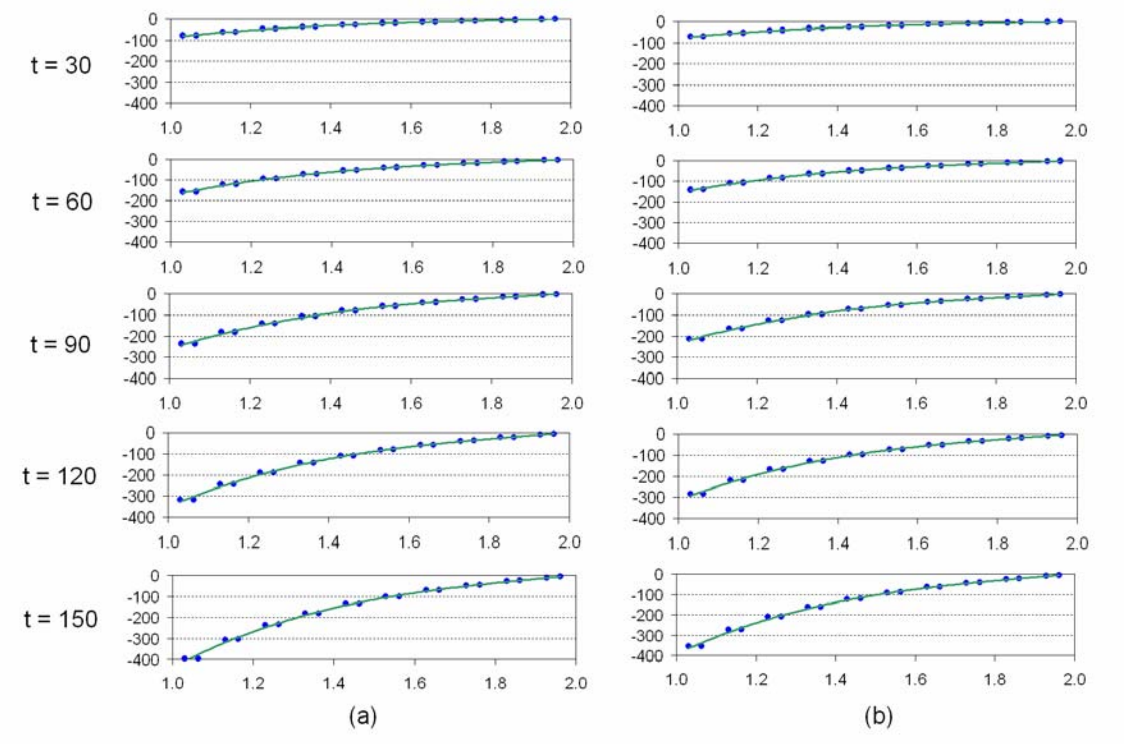

Figure 5.17 Elastic Pressure Vessel Comparison II.
(a) Radial Stress vs. Radial Position for No Multiscaling (psi)
(b) Radial Stress vs. Radial Position with Cohesive Zones Free to Open (psi)

To illustrate what is happening on the local scale of the elastic pressure vessel where cohesive zones are free to open, we have chronicled the deformations of six unit cells positioned at six different locations within the pressure vessel. The global scale integration points associated with the first three unit cells all possess the same global scale angular position Θ but different global scale radial positions R. Their positions within the global geometry are depicted in Figure 5.18. Unit cell A corresponds with the global scale integration point located at $R = 1.15$ in.; unit cell B corresponds with the global scale integration point located at $R = 1.54$ in.; and, unit cell C corresponds with the global scale integration point located at $R = 1.93$ in. Snapshots of these three unit cells are shown in thirty second increments up until the total loading time of 150 seconds. Local scale displacements have been magnified fifty times to make the deformations in each unit cell more visible in the figure.

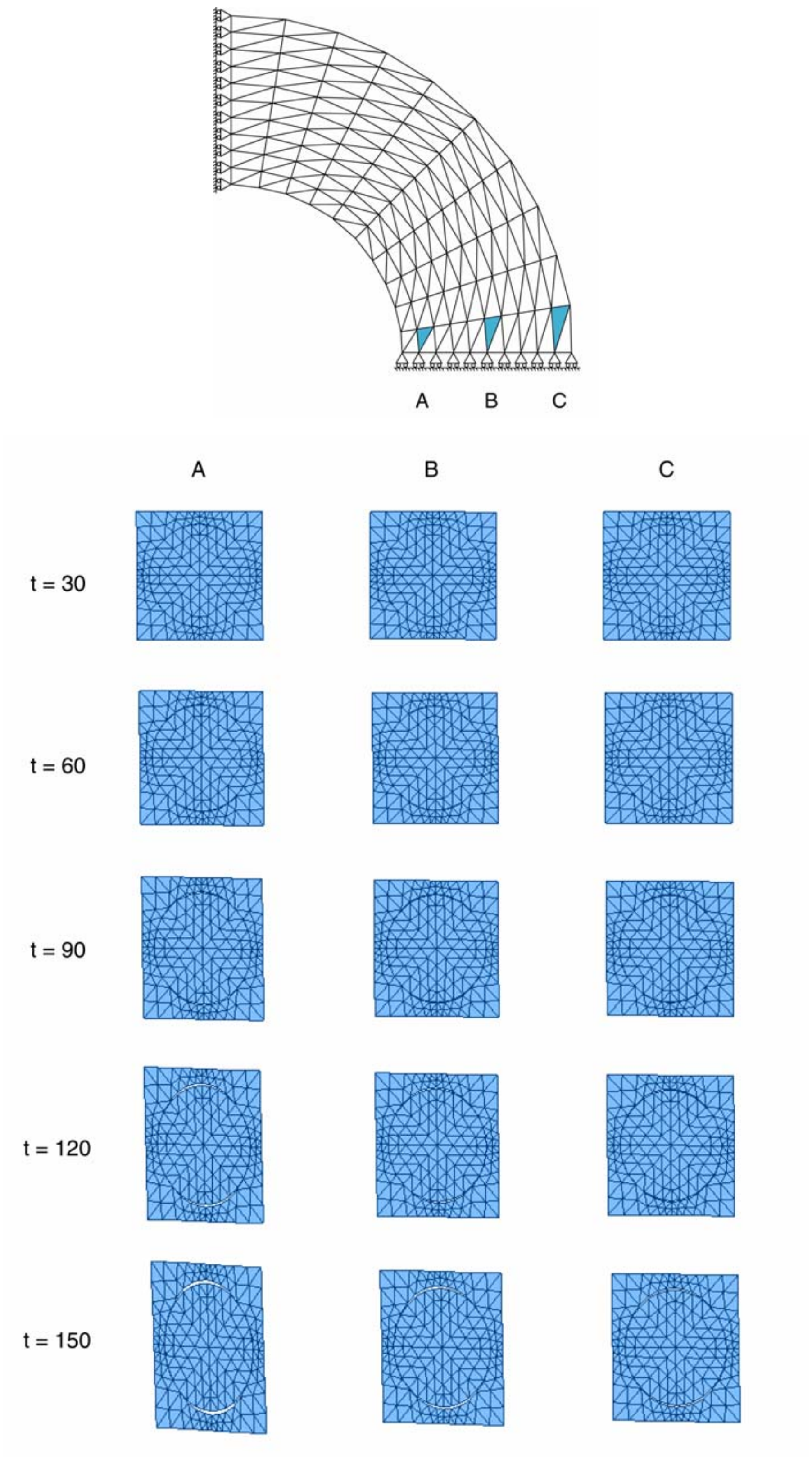

Figure 5.18 Local Scale Deformations for Elastic Pressure Vessel I.

After ninety seconds, all three unit cells in Figure 5.18 remain similar in appearance. However by 120 seconds, unit cell A exhibits the first visible signs of cohesive zones opening. Since unit cell A is located near the inner wall of the pressure vessel where the tangential stresses are the largest, it is reasonable to expect this unit cell to be the first of the three to show signs of crack growth. Because cracks are beginning to develop along the inner wall, there is a reduction in the global scale stresses at this location. This phenomenon is shown in Figure 5.16. After 150 seconds the global scale stresses at the integration points associated with unit cells B and C have grown large enough that they too begin to show effects of damage.

The global scale integration points associated with the remaining three unit cells all possess the same global scale radial position R but different global scale angular positions Θ. . Unit cell D corresponds with the global scale integration point located at $\Theta = 3.1^{\text{o}}$ in.; unit cell E corresponds with the global scale integration point located at $\Theta = 22.1^{\text{o}}$ in.; and, unit cell F corresponds with the global scale integration point located at $\Theta = 42.1^{\text{o}}$ in. Their positions within the global geometry are depicted in Figure 5.18.

In Figure 5.19, all three units cells are located near the inner wall of the pressure vessel where the tangential stresses that dominate the deformation are the greatest. However, because each cell has a different angular position Θ, each cell will have a different deformation history. After ninety seconds this fact becomes increasingly apparent. For unit cell D, where the global tangential strain runs 3.1° from vertical, deformation is predominantly characterized by elongation in the y_2 direction. For unit cell E the global tangential strain runs 22.1° from vertical and its deformation is predominantly characterized by elongation along this tangential direction. Unit cell F behaves similarly. Its deformation is characterized by elongation along its tangential direction which is 42.1° from vertical. (The waviness of the unit cell’s external boundaries is a consequence of periodic boundary conditions.) In all three cases, crack initiation and growth occur simultaneously; however, the location of the cracks within each unit cell differs according to the direction of the global tangential strain.

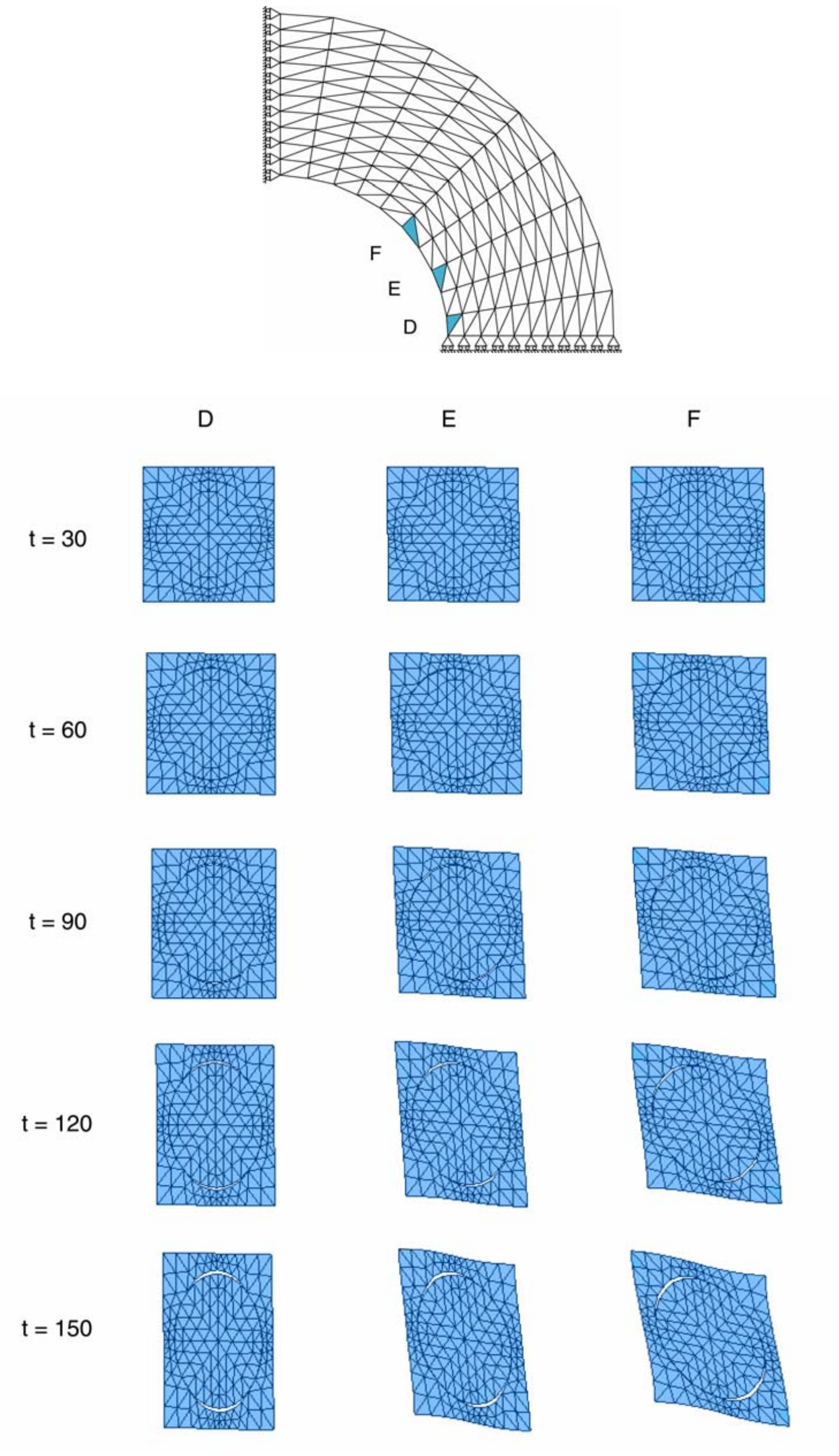

Figure 5.19 Local Scale Deformations for Elastic Pressure Vessel II.

Two more plane strain analyses were performed on this pressure vessel geometry; both of these analyses featured the viscoelastic property set presented in Table 5.4. This set of properties describes a hypothetical material system, which was designed for this demonstration. The initial properties of the global medium as well as the properties of bulk medium at the local scale are assumed to be isotropic linear viscoelastic. The uniaxial relaxation modulus for the bulk media and the cohesive zone model are represented by a standard linear solid, which may be represented by (5.2). The viscoelastic properties listed in Table 5.4 were designed so that the initial value for the relaxation modulus would be identical to the value of modulus of elasticity found in Table 5.3. Also, the constant-valued dashpot coefficient η_1 was chosen so that viscoelastic relaxation would be evident within the pressure vessel during the time of loading. Therefore, the properties listed in Table 5.4 allow us to make a direct comparison between the elastic and viscoelastic pressure vessel problems.

Table 5.4 Material Properties for Viscoelastic Thick-Walled Pressure Vessel Problem.

Global*			**Local**					
Bulk Properties			**Bulk Properties**			**Cohesive Zone Properties**		
E_∞	5.00E+05	(psi)	E_∞	5.00E+05	(psi)	E_∞	5.00E+05	(psi)
E_1	5.00E+05	(psi)	E_1	5.00E+05	(psi)	E_1	5.00E+05	(psi)
η_1	4.00E+06	(psi-s)	η_1	4.00E+06	(psi-s)	η_1	4.00E+06	(psi-s)
ν	0.0	(--)	ν	0.0	(--)	ν	0.45	(--)
						δ_n	5.00E-04	(in.)
						δ_t	5.00E-04	(in.)
						m	1.00E-03	(in.)
						s	2.00E-04	(in.)
						r_{cr}	1.00E-04	(in.)

* Global properties are necessary for first time step only

In the first viscoelastic pressure vessel problem, we do not consider the effects of local scale damage; in the second viscoelastic pressure vessel problem, we do. Figure 5.20 presents the tangential stress distribution predicted by both of these analyses. As expected, the two tapered bars initially display identical stress distributions. However, after ninety

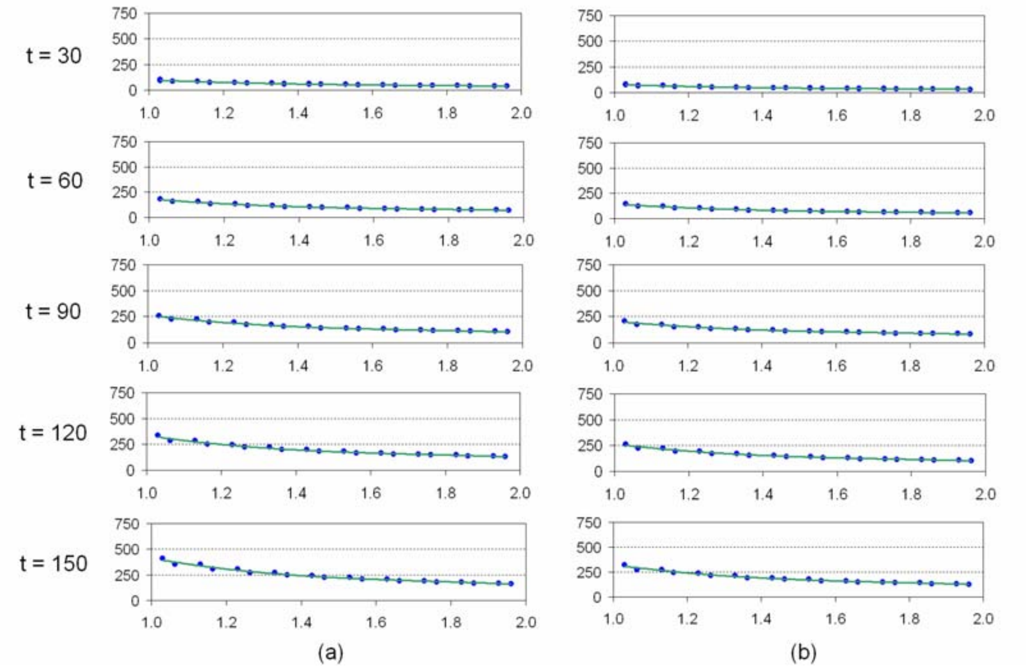

Figure 5.20 Viscoelastic Pressure Vessel Comparison I.
(a) Tangential Stress vs. Radial Position for No Multiscaling (psi)
(b) Tangential Stress vs. Radial Position with Cohesive Zones Free to Open (psi)

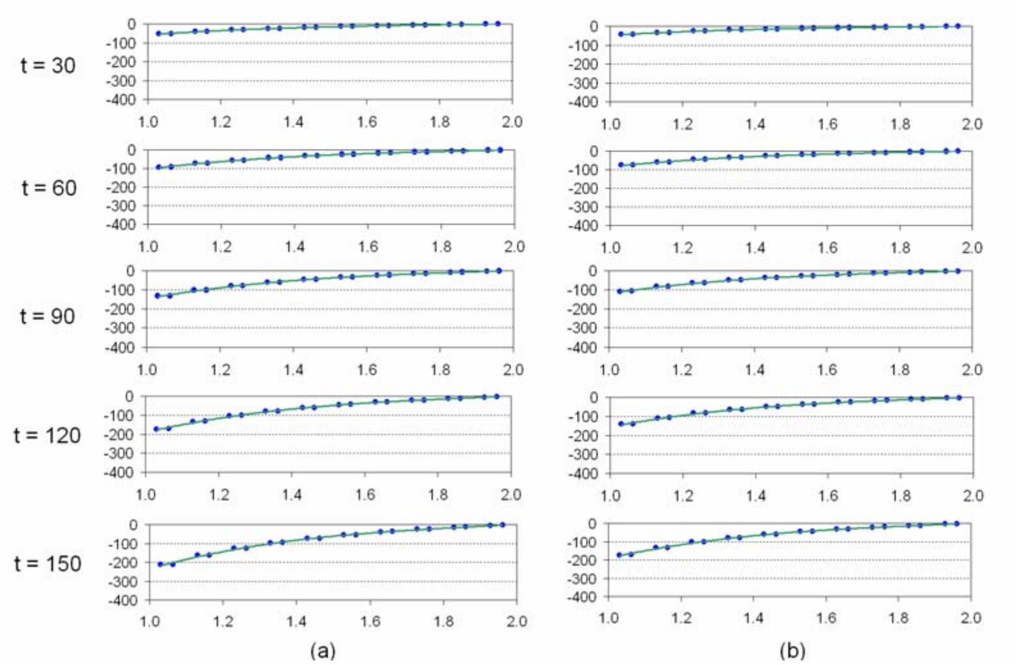

Figure 5.21 Viscoelastic Pressure Vessel Comparison II.
(a) Radial Stress vs. Radial Position for No Multiscaling (psi)
(b) Radial stress vs. Radial Position with Cohesive Zones Free to Open (psi)

seconds, local scale damage diminishes stress near the internal boundary. A similar remark can be made with respect to the radial stresses as shown in Figure 5.21. Furthermore, viscoelastic relaxation does take its toll in these analyses: The stress magnitudes in Figures 5.20 and 5.21 are less than their elastic counterparts as shown in Figures 5.16 and 5.17.

Figures 5.22 and 5.23 compare and summarize the stress distributions of the four pressure vessel problems. Finite element predictions for the elastic and viscoelastic problems without damage compare well with their corresponding analytic solutions. These figures illustrate the stress relaxation caused by both viscoelastic and damage effects.

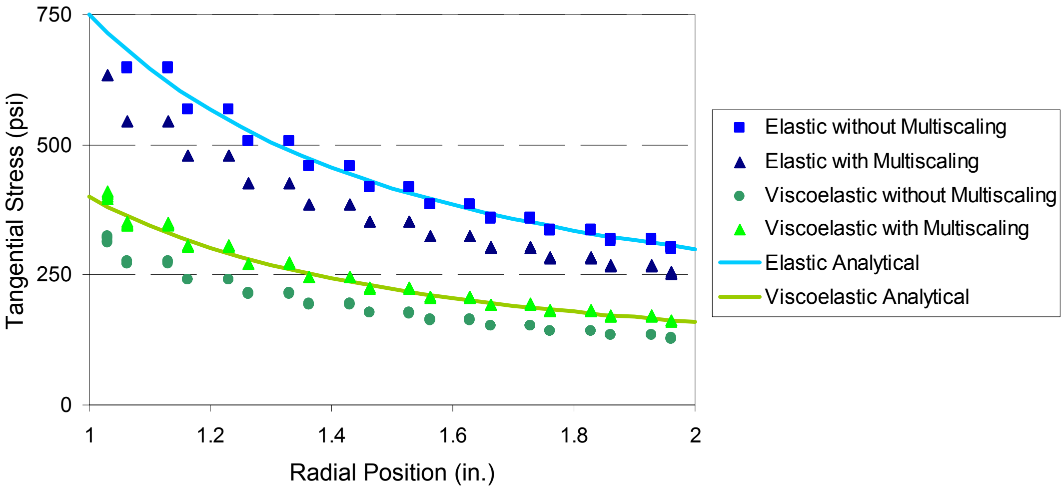

Figure 5.22 Summary of Pressure Vessel Problems I: Tangential Stresses at t = 150 s.

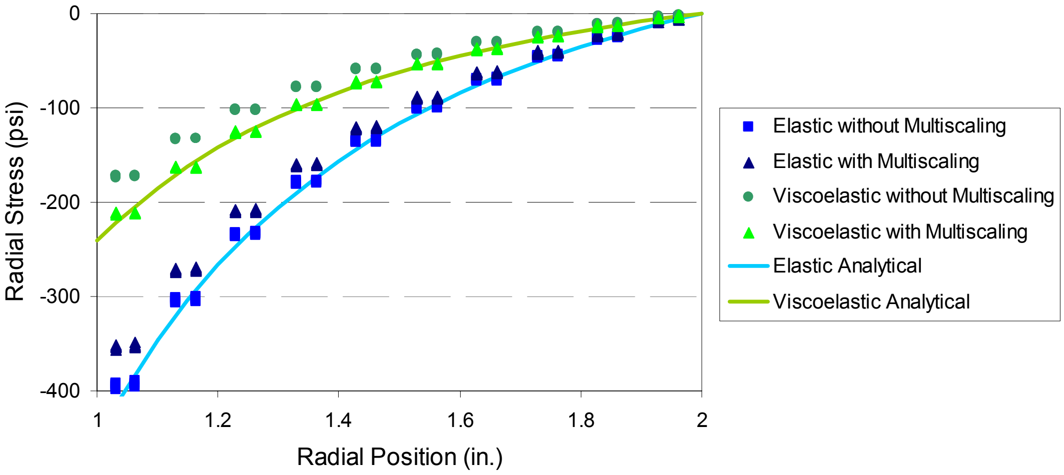

Figure 5.23 Summary of Pressure Vessel Problems II: Radial Stresses at t = 150 s.

A convergence study was performed to determine the necessary size of the size of the time step for the tapered bar analysis. Figure 5.24 shows three stress distributions for the viscoelastic tapered bar with multiscale damage. Each distribution was calculated using a different increment in time Δt: 0.1, 1.0, and 5.0 seconds. A less than 2% difference exists between the 0.1 and 1.0-second time step; therefore a 1.0-second time step was deemed as acceptable for this demonstration.

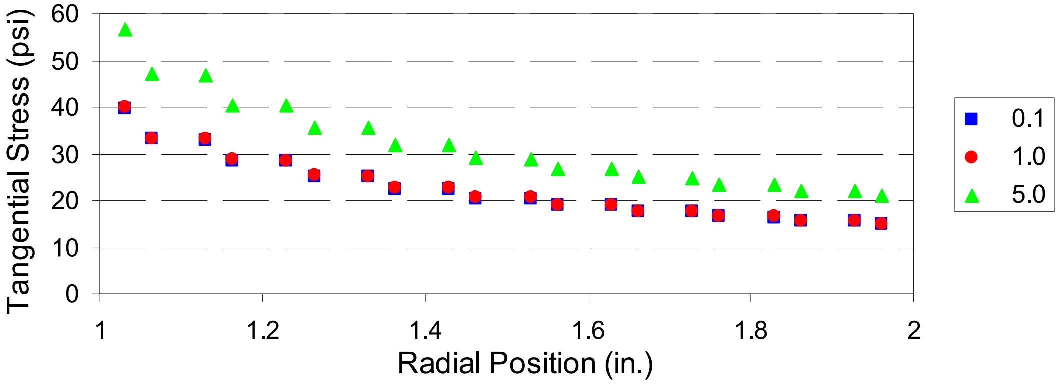

Figure 5.24 Time Step Convergence Study for Pressure Vessel Problem.

As before with the tapered bar example, we have constructed a quasi-analytic model for the purpose of checking our finite element solution to the pressure vessel problem. We begin with a variation of the Cauchy-Euler equation

$$\begin{aligned}&\frac{d^2u_R(R,t)}{dR^2}+\frac{1}{R}\frac{du_R(R,t)}{dR}-\frac{1}{R^2}u_R(R,t)\\&+\frac{1}{\lambda+2\mu}\left(\frac{d\sigma_{RR}^D(R,t)}{dR}+\frac{1}{R}\sigma_{RR}^D(R,t)\right)=0\end{aligned}\qquad \text{for } 1\le R\le 2 \qquad (5.6)$$

where $u_R(R,t)$ is the global scale displacement in the radial coordinate R. The isotropic linear elastic Lamé constants are represented by λ and μ. In this example there are no damage induced stresses in the tangential direction, i.e. $\sigma_{\Theta\Theta}(R,t)=0$.

A power law type damage equation that varies with respect to radial position R was imposed is represented by the following

$$\sigma_{RR}^{D}(R,t) = -\left(1.3-\frac{R}{2}\right)^{5}. \tag{5.7}$$

This law is not physically based; it has been designed to yield a noticeable effect in the global displacements for the purpose of checking the finite element program. All loading, geometry, and material properties remain the same as those used in the previous elastic pressure vessel problem with local scale damage.

Figure 5.25 shows the distribution of the damage induced stresses $\sigma_{RR}^{D}(R,t)$ calculated by our finite element code after 15 seconds.

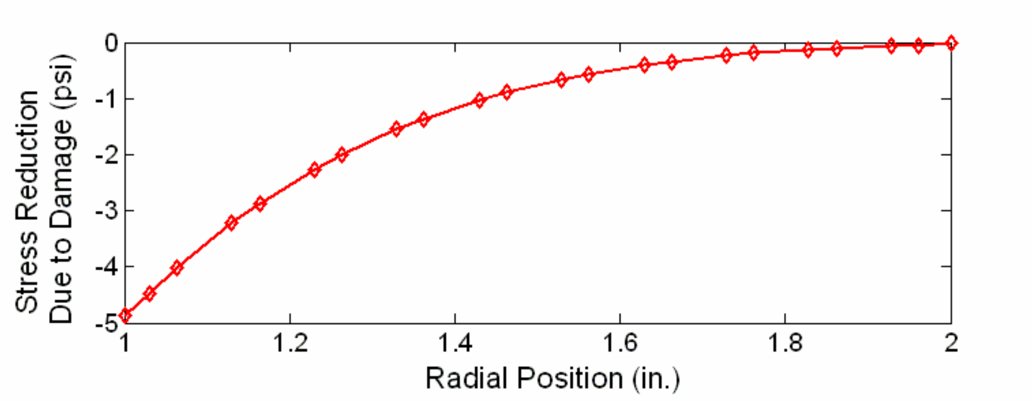

Figure 5.25 Reduction in Radial Stress Made by Local Scale Damage.

Runge Kutta was used to calculate the displacements for the elastic pressure vessel. These displacements are shown in Figure 5.26. From this figure it can be seen that the values calculated by the quasi-analytical solution and by the multiscale finite element program are in close agreement.

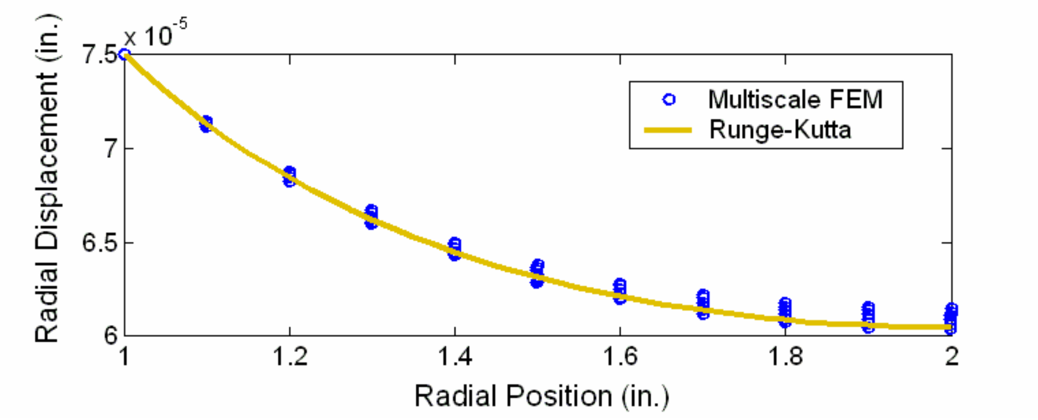

Figure 5.26 Comparison of Quasi-Analytical Solution and Finite Element Program II.

5.3 Road Problem

We now turn our attention toward the road problem that was first introduced in the Section 1. As we mentioned before, asphaltic pavements are excellent examples of multiple scale viscoelastic structures susceptible to multiple scale fracture mechanisms. By addressing this problem, we will demonstrate how our multiscale model can be a cost-effective tool for evaluating future asphaltic pavement designs. We present a clear procedure for performing similar multiscale analyses on a variety of practical problems.

We begin by defining the geometries associated with a typical asphaltic pavement. Consider the two-lane road structure depicted in Figure 5.27. For simplicity, we have chosen to use geometric symmetry to model only the right side of this road structure. For the cross-section shown in this figure, road traffic moves into the page. The top surface of the road structure is 12 meters wide (two 3.7-meter lanes and two 2.3-meter shoulders). Normally, roads of this type have a 2 to 4% cross-slope for drainage; however, no crown has been introduced in this road geometry. The top layer is a 0.2-meter thick mixture of crushed coarse aggregate of various shapes and sizes imbedded in an asphaltic tar matrix.

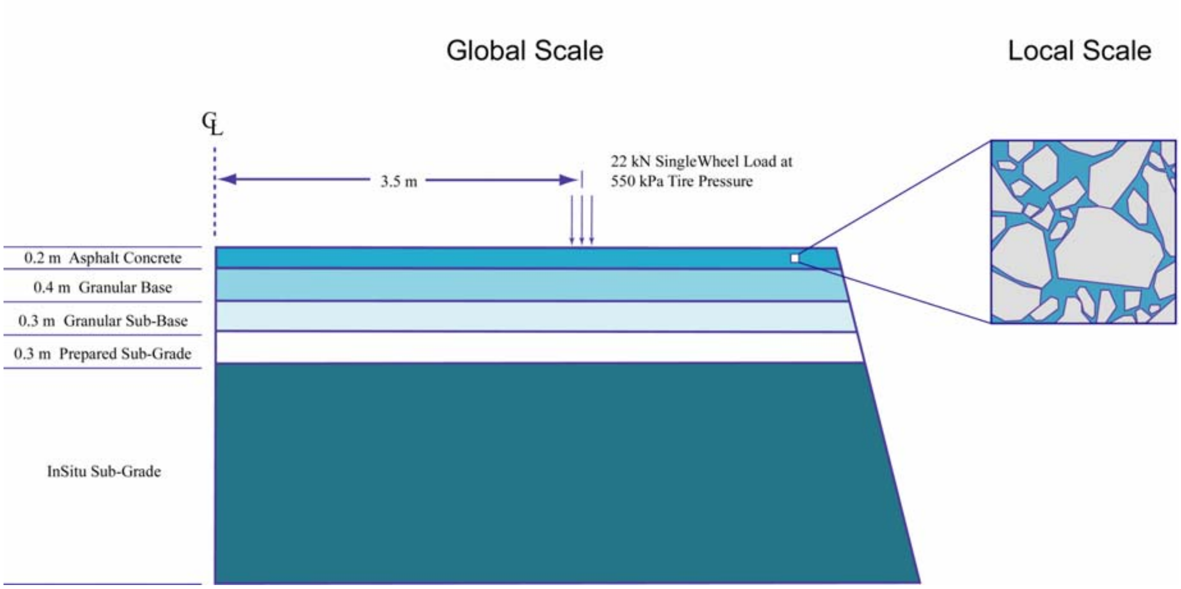

Figure 5.27 Global and Local Geometries for Road Problem.

A close-up of the local scale geometry is also depicted in Figure 5.27. Below this asphaltic layer are four other layers: a 0.4-meter granular base; a 0.3-meter granular sub-base; a 0.3-meter clay till sub-grade; and in situ sub-grade. In this model, the in situ sub-grade extends 2 meters below the prepared sub-grade. Although the top layer is modeled as an anisotropic viscoelastic medium, the remaining layers are treated as homogeneous isotropic linear elastic media.

Two problems arise when defining the local scale geometry for this analysis. First, asphaltic pavements do not exhibit spatially repeating microstructures. The randomly-oriented, irregularly-shaped pieces of aggregate prevent the establishment of any true unit cell. Second, because of the high volume fraction of the aggregate any sampling of the local geometry assumed to be unit cell Y will almost certainly have its external boundaries ∂Y intersect with pieces of the aggregate. This situation results in a material asymmetry along the external boundary of the unit cell that conflicts with the symmetry requirements specified in Section 2. To address the first problem, we choose to identify a volume of asphaltic material that is representative of the media as a whole. This representative volume should satisfy all the requirements for statistical homogeneity. To address the second problem, we must relax our requirement for periodic boundary conditions and instead opt for mirror-type boundary conditions. Mirror-type boundary displacements vary linearly with respect to the local coordinate y_1, y_2, or y_3. By addressing these problems in the manner we have described, we are adopting a mean-field approach to this multiple scale fracture problem.

To define the local scale geometry, we use photographs taken of actual asphalt samples. These samples -- originally fabricated for cyclic fatigue material characterization tests – were cut open to reveal the internal geometry of the asphalt along several cross-sections. The photograph shown in Figure 5.28a represents a portion of one of the asphalt sample’s cross-section. From this photograph, we were able to establish a representative volume element based on the size, shape, and orientation of the larger pieces of aggregate found in the photograph. This representative volume is shown in Figure 5.28b.

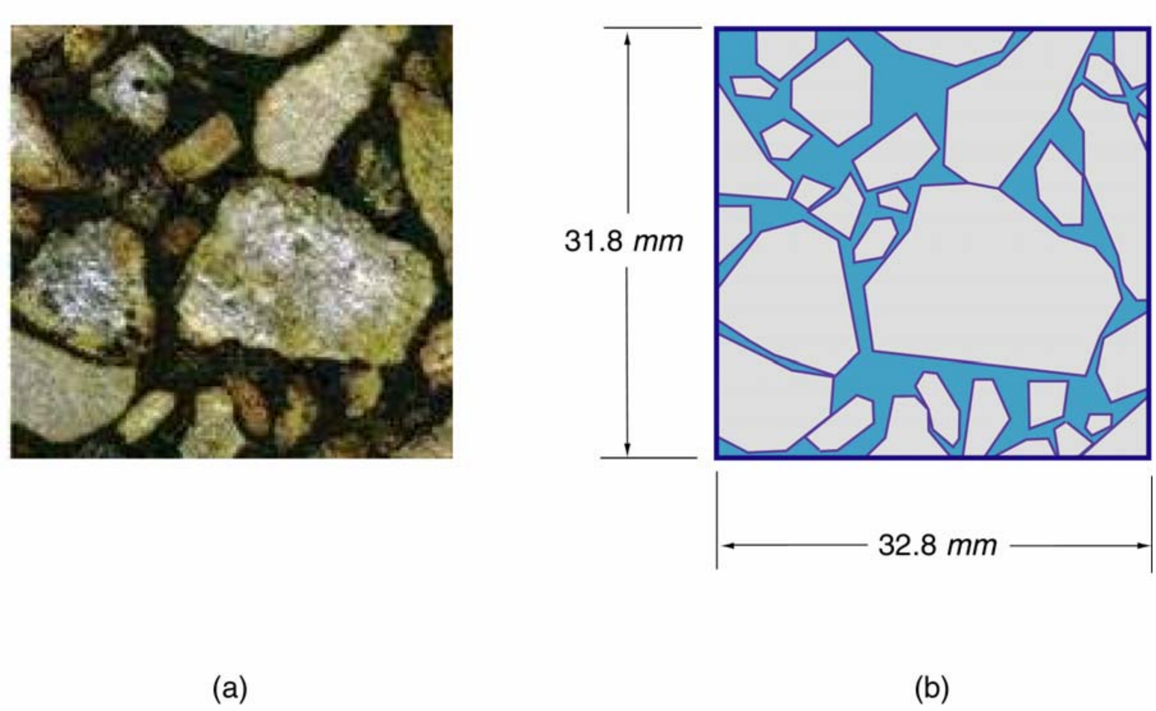

Figure 5.28 Local Scale Geometry of Asphalt.
(a) Photograph of Proposed Asphaltic Material System
(b) Representation of Local Geometry Based on Photograph.

The volume of the aggregate depicted in Figure 5.28 represents only 74% of the total representative volume. For this particular asphalt system, this value is consistent with aggregate pieces that have a critical dimension greater than or equal to 2 mm. In actuality, 85% of this material system is composed of aggregate material. The missing 11% is represented by what are called *fines* -- small pieces of rock, sand, and lime with a critical dimension less than 2 mm. These fines are dispersed throughout the tar-like matrix material; however they are too small to model explicitly in this example problem. To account for the fines we have calculated effective viscoelastic mechanical properties for the tar/fines mixture.

The domain of the global road structure was partitioned using 862 CSTs. This mesh is shown in Figure 5.29. The asphaltic layer is divided into 243 elements, fifty-six of which have been specified as multiscale elements. These multiscale elements are located in the vicinity of the applied tire load. In this region of the uppermost layer, the multiscale elements allow us to treat the asphalt as an anisotropic nonlinear viscoelastic medium. The remainder of the asphaltic layer is treated as being isotropic linear viscoelastic.

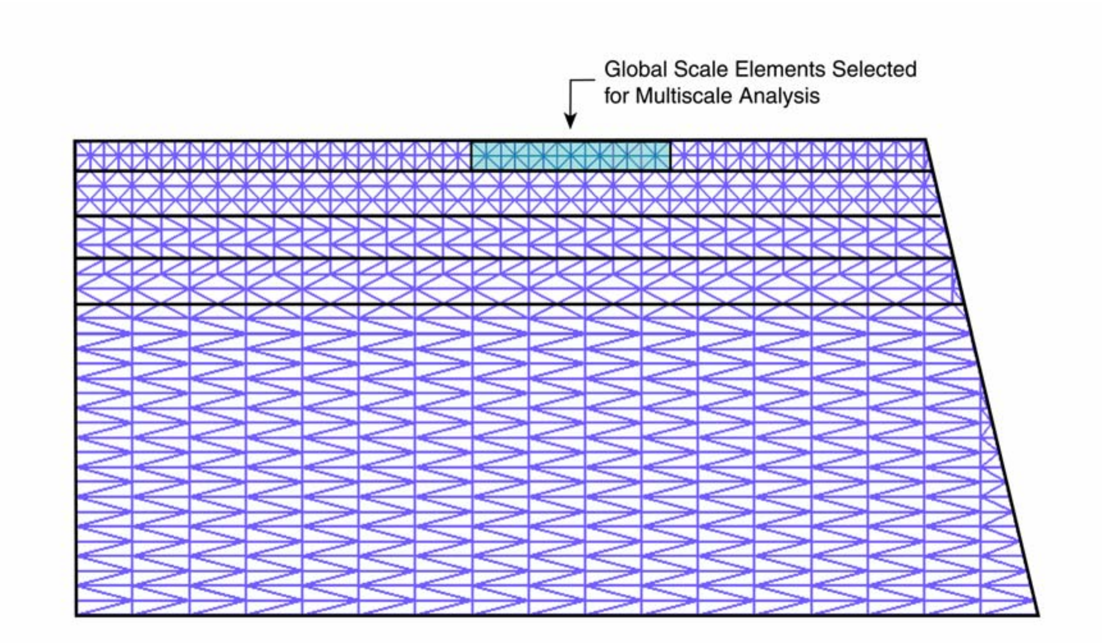

Figure 5.29 Finite Element Mesh for Global Road Structure.

The domain of the local scale problem was also partitioned using CSTs. The finite element mesh of the local geometry, which is featured in its undeformed state in Figure 5.30, consists of 1379 CSTs. The aggregate is modeled as being isotropic linear elastic; the matrix material possesses the effective properties for the tar/fines mixture. Fracture is introduced into this model by way of 671 cohesive zone elements -- all located along the boundaries of the aggregate. By placing these cohesive zone elements along the interface between the rocks and the matrix we are suggesting that the only possible mode of fracture is adhesive fracture; i.e. the separation of one type of a rock from the tar-like matrix. In actuality, fracture can occur in a variety of ways including matrix-matrix separation and brittle cracking through aggregate. Experimental evidence has shown that fracture in asphaltic pavements is most likely to occur as matrix-matrix separation very close to the aggregate-binder interface. Our model works well as a first approximation of this phenomenon.

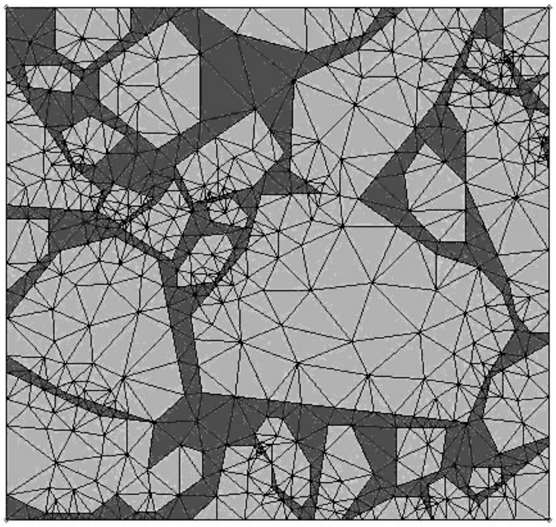

Figure 5.30. Local Scale Mesh of Asphalt Concrete Mixture.

Table 5.5 lists the mechanical properties of the base constituents found in the asphaltic layer. The tar without the fines is defined by a generalized Maxwell model (5.2).

Table 5.5 Material Properties for Asphaltic Constituents.

Properties for Asphalt Components					
Rock		**Tar**			
E	ν	*q*	*E*	η	ν
(GPa)	(--)	(--)	(Pa)	(Pa-s)	(--)
55.2	*0.15*	∞	*4.32E+00*	--	*0.45*
		1	*2.46E+07*	*2.02E+04*	
		2	*3.68E+06*	*2.83E+04*	
		3	*5.98E+05*	*3.45E+04*	
		4	*8.45E+04*	*4.53E+04*	
		5	*1.25E+04*	*6.58E+04*	
		6	*1.86E+03*	*9.78E+04*	
		7	*2.77E+02*	*1.46E+05*	
		8	*4.38E+01*	*2.42E+05*	
		9	*8.74E+00*	*6.52E+05*	

Table 5.6 lists the isotropic linear elastic properties for the layers below asphaltic pavement.

Table 5.6 Material Properties for Road Sub-Layers.

Properties for Road Sub-Layers*							
InSitu Sub-Grade		**Prepared Sub-Grade**		**Granular Sub-Base**		**Granular Base**	
E	ν	E	ν	E	ν	E	ν
(Pa)	(--)	(Pa)	(--)	(Pa)	(--)	(Pa)	(--)
2.00E+11	*0.35*	*1.00E+11*	*0.30*	*5.00E+10*	*0.30*	*5.00E+10*	*3.00*

*Sub-layer properties are necessary for every time step.
No multiscaling is performed on the road sub-layers.

The mechanical properties of the cohesive zone model are listed in Table 5.7. The cohesive zone viscoelastic relaxation modulus is taken directly from the tar properties listed in Table 5.5. The mean μ, standard deviation ζ, and critical fibril radius r_{cr} are all experimentally measured values taken from the work reported by Williams (2002).

Table 5.7 Material Properties for Viscoelastic Cohesive Zones.

Tar Cohesive Zone Properties								
q	C_{11}	η_{11}	ν	δ_n	δ_t	μ	ζ	r_{cr}
(--)	(Pa)	(Pa-s)	(--)	(m)	(m)	(m)	(m)	(m)
∞	*4.32E+10*	--	*0.27*	*1.00E-01*	*1.00E-01*	*1.26E-03*	*2.53E-04*	*1.26E-04*
1	*2.46E+07*	*8.20E-04*						
2	*3.68E+06*	*7.69E-03*						
3	*5.98E+05*	*5.77E-02*						
4	*8.45E+04*	*5.37E-01*						
5	*1.25E+04*	*5.29E+00*						
6	*1.86E+03*	*5.26E+01*						
7	*2.77E+02*	*5.26E+02*						
8	*4.38E+01*	*5.53E+03*						
9	*8.74E+00*	*7.46E+04*						

To account for the fines embedded in the tar-like matrix, we took a strict rule of mixtures approach. By volume, this mixture is consists of 40% tar and 60% fines. The resulting effective viscoelastic properties for this mixture are listed in Table 5.8.

Table 5.8 Viscoelastic Stiffnesses for Tar with Fines.

Tar Properties with Fines								
q	C_{11}	η_{11}	q	C_{12}	η_{12}	q	C_{66}	η_{66}
(--)	(Pa)	(Pa-s)	(--)	(Pa)	(Pa-s)	(--)	(Pa)	(Pa-s)
∞	2.26E+10	--	∞	4.00E+09	--	∞	1.95E+10	--
1	3.73E+07	3.06E+04	1	3.06E+07	2.51E+04	1	3.40E+06	2.79E+03
2	5.59E+06	4.29E+04	2	4.57E+06	3.51E+04	2	5.08E+05	3.91E+03
3	9.07E+05	5.24E+04	3	7.42E+05	4.29E+04	3	8.25E+04	4.76E+03
4	1.28E+05	6.88E+04	4	1.05E+05	5.63E+04	4	1.17E+04	6.25E+03
5	1.89E+04	9.99E+04	5	1.55E+04	8.17E+04	5	1.72E+03	9.08E+03
6	2.82E+03	1.49E+04	6	2.31E+03	1.21E+05	6	2.56E+02	1.35E+04
7	4.20E+02	2.21E+05	7	3.44E+02	1.81E+05	7	3.82E+01	2.01E+04
8	6.64E+01	3.67E+05	8	5.44E+01	3.00E+05	8	6.04E+00	3.34E+04
9	1.33E+01	9.90E+05	9	1.09E+01	8.10E+05	9	1.21E+00	9.00E+04

Table 5.9 Composite-Level Stiffnesses for Asphalt.

Asphalt Composite Properties*								
q	C_{11}	η_{11}	q	C_{12}	η_{12}	q	C_{66}	η_{66}
(--)	(Pa)	(Pa-s)	(--)	(Pa)	(Pa-s)	(--)	(Pa)	(Pa-s)
∞	3.38E+10	--	∞	5.97E+09	--	∞	2.91E+10	--
1	9.81E+06	8.04E+03	1	8.02E+06	6.58E+03	1	8.92E+05	7.31E+02
2	1.47E+06	1.13E+04	2	1.20E+06	9.23E+03	2	1.33E+05	1.03E+03
3	2.38E+05	1.38E+04	3	1.95E+05	1.13E+04	3	2.17E+04	1.25E+03
4	3.36E+04	1.81E+04	4	2.75E+04	1.48E+04	4	3.06E+03	1.64E+03
5	4.96E+03	2.62E+04	5	4.06E+03	2.15E+04	5	4.51E+02	2.38E+03
6	7.40E+02	3.89E+04	6	6.06E+02	3.19E+04	6	6.73E+01	3.54E+03
7	1.10E+02	5.81E+04	7	9.03E+01	4.75E+04	7	1.00E+01	5.28E+03
8	1.74E+01	9.64E+04	8	1.43E+01	7.89E+04	8	1.59E+00	8.76E+03
9	3.48E+00	2.60E+05	9	2.85E+00	2.13E+05	9	3.17E-01	2.36E+04

* Asphalt composite properties are necessary for first time step only

Overall effective viscoelastic properties for the asphalt composite were also calculated using a rule of mixtures approach. These properties, which are listed in Table 5.9, are assigned to and used by all regions of the asphalt layer during the first time step. After the initial time step, these properties continue to be used by those regions of the asphalt layer where no multiscale analysis is performed. Regions where multiscale analysis is performed receive updated mechanical properties from the local scale analyses.

The load applied to the surface of the asphalt pavement represents the single wheel load imposed by a standard 8-axle trailer truck used in the transport of agricultural or manufactured goods. When the truck is parked on the pavement, this single wheel transfers a 22 kN static load to the pavement at a tire pressure of 550 kPa over a footprint of about 0.2 m × 0.2 m. For this analysis, we chose to calculate the pavement response to the cyclic loading caused by heavy truck traffic. Figure 5.31 illustrates the sinusoidal loading cycle imposed in our analysis. This loading represents the passing in rapid succession of five identical tire loads. The period of each cycle is 1.0 second; the length of each analysis is 5.0 seconds. Although the duration of each road analysis is relatively short when compared to the lifetime of a road structure, five load cycles will be enough to demonstrate permenant deformation caused by local scale internal boundary movement and the growth of local scale cracks.

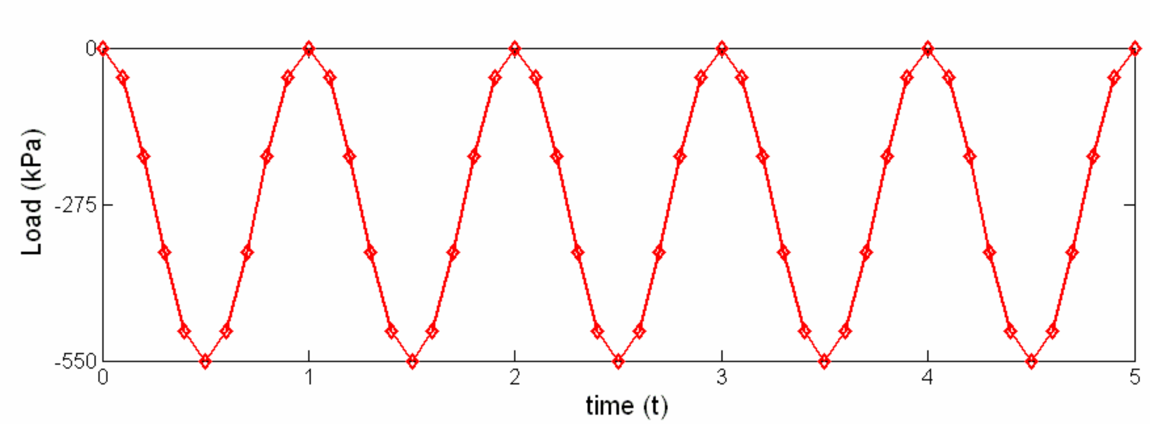

Figure 5.31 Single Tire Load vs. Time.

Three plane strain analyses were performed for this road model. The maximum surface displacement of the asphaltic pavement for all three of these analyses is recorded in Figure 5.32.

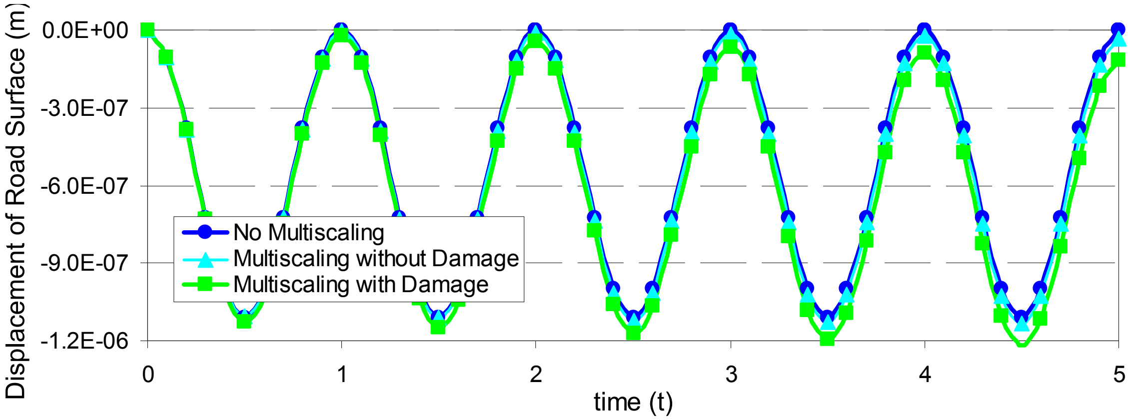

Figure 5.32 Displacement of Road Surface vs. Time.

The first analysis involves no multiscaling. In this analysis the pavement responds elastically; no permanent deformation that would lead to the creation of a rut is detectable at this timescale. This response is understandable in light of the material model used for the effective properties of the asphalt. With a rule of mixtures approach the constituent with the largest stiffness dominates the response of the entire medium. Because the stiffness and volume fraction of the elastic aggregate is so much greater than that of the viscoelastic matrix, the global displacements behave elastically during the first five cycles.

The second analysis does include multiscale effects. In this case no cracks are permitted to initiate and grow. Instead, we consider the effects that are caused by the movement of fully cohesive internal boundaries. Previously we discussed a similar analysis that was performed on the tapered bar geometry. In this analysis we were able to show that by preventing crack growth at the local scale we could recover the non-multiscaling response of the tapered bar (as shown in Figure 5.4). This was because the material constitution was the same on both sides of the potential crack path. In effect, the second term on the right-hand side of our multiscale constitutive equation (2.38) is zero. In this example, however, a material mismatch exists along the internal boundaries formed by the aggregate/matrix interfaces. Even if these interfaces were to remain fully cohesive, this mismatch means that the second term on the right-hand side of our multiscale constitutive equation is not zero. Thus, a local scale contribution to the global scale stress exists. Under these circumstances we can see that this material mistmatch contributes towards a 3.2×10^{-8}-meter permanent deformation of the asphalt pavement.

The third analysis includes multiscale effects in the form of local scale crack growth. Since the tire loading is compressive, most of the local scale damage contributions come from sliding of the aggregate/matrix interfaces. After five cycles, we record a permanent deformation of 1.2×10^{-8} meters.

Together, the first two analyses illustrate that a single scale model of the asphalt pavement neglects a potentially significant source of energy dissipation caused by the movement of internal boundaries. Including the third analysis, we see that without the dissipative effects of local scale crack growth, we can easily over estimate the service life of the pavement.

6. CONCLUSION

A new multiscale method has been developed for the performance of stress analyses on viscoelastic composites which exhibit structure on two length scales. The primary motivation for the development of this method is so that we can model the damaging effects of local scale time-dependent crack growth on the mechanical performance of the global structure. This particular modeling capability should prove to be a very powerful technique in the life prediction of a wide range of polymeric composite structures.

The code developed from this multiscale method is a versatile, easy to use, tool for modeling many interesting multiscale initial boundary value problems. Because this method has been formulated into a finite element program, there are few limitations to its modeling capabilities with respect to morphological details, such as: the number of constituents; the number of constituent types; constituent geometry; etc. Furthermore, within a well defined unit cell structure or representative volume, all damage attributed to the initiation and growth of discrete cracks can be modeled discretely. This feature provides a considerable advantage over those models which are based on continuum damage mechanics and other phenomenological schemes. As a result, this model can potentially minimize the need for extensive laboratory experimentation since it will rely strictly upon the fundamental structural properties of each of the composite’s constituents.

In terms of finite elements, there are many techniques that can be implemented to improve our finite element program. Most of these techniques are the standard fare found in any good finite element textbook. Therefore, we will refrain from focusing on these potential improvements. Instead, we would like to focus on two particular areas in which vast gains in the modeling capabilities of our multiscale program could be made. First, the code should be expanded to three dimensions. This would be a daunting, but necessary, task. While there are many instances when planar analyses are sufficient in modeling structural behavior, for the class of problems which we endeavor to solve this is often not the case. It is difficult to assess *a priori* the loss in accuracy we incur by choosing to model certain structures (which have randomly-oriented, randomly-distributed inclusions) with a planar analysis. Therefore, expanding the modeling capabilities of the code to three dimensions should be a considerable improvement. Second, multiscale finite element programs are prime candidates for parallel processing. After each global scale analysis, a single processor computer must then labor over one local scale analysis to completion before moving on to the next local scale analysis. If the number of local scale analyses is large, the solution process for this multiscale problem could be unacceptably slow. But if we can take advantage of the fact that each local scale analysis is completely independent of all the other local scale analyses, we can efficiently solve the same multiscale problem on a computer equipped with multiple processors. With multiple processors, a computer can apportion a fraction of the local scale analyses to each processor. Then, a single processor can work on its set of local scale analyses, while at the same time, the other processors work on there respective sets of local scale analyses. Thus, a computer can post a significant reduction in the overall computational time of the problem.

REFERENCES

Allen, D. H. and Searcy, C. R., 2000. Numerical aspects of a micromechanical model of a cohesive zone. Journal of Reinforced Plastics and Composites 19, 240-248.

Allen, D. H., Searcy, C. R., 2001a. A micromechanical model for a viscoelastic cohesive zone. International Journal of Fracture 107, 159-176.

Allen, D. H. and Searcy, C. R., 2001b. A micromechanically-based model for predicting dynamic damage evolution in ductile polymers. Mechanics of Materials 33, 177-184.

Allen, D. H., Yoon, C., 1998. Homogenization techniques for thermoviscoelastic solids containing cracks, International Journal of Solids and Structures 35, 4035-4053.

Barenblatt, G. I., 1962. The mathematical theory of equilibrium cracks in brittle fracture, Advances in Applied Mechanics 7, 55-129.

Bensoussan, A., Lions, J. L., Papanicolaou, G., 1978. Asymptotic analysis for periodic structures, Studies in Mathematics and Its Applications 5, North-Holland, Amsterdam.

Carrere, N., Feyel, F., Kruch, S., 2003. Multi-scale modelling of silicon carbide reinforced titanium MMCs: Application to advanced compressor design. Aerospace Science and Technology 7, 307-315.

Chaboche, J.-L., Kruch, S, Maire, J.-F., Pottier, T., 2001. Towards a micromechanics based inelastic and damage modeling of composites. International Journal of Plasticity 17, 411-439.

Christensen, R. M., 1979. Mechanics of Composite Materials, Wiley, New York.

Christoffersen, J. 1983. Bonded granulates. Journal of the Mechanics and Physics of Solids 29, 143-150.

Chung, P. W., Tamma, K. K., Namburu, R. R., 2000. A finite element thermo-viscoelastic creep approach for heterogeneous structures with dissipative correctors. Finite Elements in Analysis and Design 36, 279-313.

Dugdale, D. S., 1960. Yielding of steel sheets containing slits, Journal of the Mechanics and Physics of Solids 8, 100-104.

Dvorak, G., 1992. Transformation field analysis of inelastic composite materials. Proceedings of the Royal Society of London A437, 311-327.

Feyel, F., 1999. Multiscale FE^2 elastoviscoplastic analysis of composite structures. Computational Materials Science 16, 344-354.

Feyel, F., Chaboche, J.-L., 2000. FE^2 multiscale approach for modeling the elastoviscoplastic behavior of long fibre SiC/Ti composite materials. Computer Methods in Applied Mechanics and Engineering 183, 309-330.

Fish, J., Belsky, V., 1995. Multigrid method for periodic heterogeneous media, part II: multiscale modeling and quality control in multidimensional cases. Computer Methods in Applied Mechanics and Engineering 126, 17-38.

Fish, J., Shek, K., 2000. Multiscale analysis of composite materials and structures. Composites Science and Technology 60, 2547-2556.

Fish, J., Shek, K., Pandheeradi, M., Shephard, M. S., 1997. Computational plasticity for composite structures based on mathematical homogenization: Theory and practice. Computer Methods in Applied Mechanics and Engineering 148, 53-73.

Fish, J., Wagiman, A., 1993. Multiscale finite element method for a locally non-periodic heterogeneous medium. Computational Mechanics 12, 164-180.

Foulk, J. W., Allen, D. H., Helms, K. L. E., 2000. Formulation of a three-dimensional cohesive zone model for application to a finite element algorithm. Computer Methods in Applied Mechanics and Engineering, 183, 51-60.

Ghosh, S., Lee, K., Raghavan, P., 2001. A multi-level computational model for multi-scale damage analysis in composite and porous materials, International Journal of Solids and Structures 38, 2335-2385.

Griffith, A.A., 1920, The phenomena of rupture and flow in solids, Philosophical Transactions of the Royal Society of London A221, 163-197.

Irwin, G. R., 1958. Fracture. In: Flugge, S. (Ed.), Handbuch der Physik 6, Springer-Verlag, Berlin, 551-590.

Jansson, S., 1992. Homogenized nonlinear constitutive properties and local stress concentrations for composites with periodic internal structure, International Journal of Solids and Structures 29, 2181-2200.

Kim, Y.-R., 2003. Mechanistic fatigue characterization and damage modeling of asphalt mixtures. Ph.D. Dissertation, Texas A&M University.

Lee, K., Moorthy, S, Ghosh, S., 1999. Multiple scale computational model for damage in composite materials. Computer Methods in Applied Mechanics and Engineering 172, 175-201.

Lene, F., 1986. Damage constitutive relations for composite materials, Engineering Fracture Mechanics 25, 713-728.

Lene, F., Leguillon, D., 1982. Homogenized constitutive law for a partially cohesive composite model, International Journal of Solids and Structures 18, 443-458.

Maghous, S., Creus, G. J., 2003. Periodic homogenization in thermoviscoelasticity: case of multilayered media with ageing. International Journal of Solids and Structures 40, 851-870.

Mura, T., 1987. Micromechanics of Defects in Solids, 2nd Ed., Martinus Nijhoff Publishers, Dordrecht.

Nadot-Martin, C., Trumel, H., Dragon, A., 2002. Morphology-based homogenization for viscoelastic particulate composites: Part I: Viscoelasticity sole, European Journal of Mechanics A/Solids 22, 89-106.

Nemat-Nasser, S., Hori, M., 1993. Micromechanics: Overall Properties of Heterogeneous Materials, North Holland, New York.

Oden, J. T., Vemaganti, K., Möes, N., 1999. Hierarchical modeling of heterogeneous solids. Computational Methods in Applied Mechanics and Engineering 172, 3-25.

Oden, J. T., and Zohdi, T. I., 1997. Analysis and adapative modeling of highly heterogeneous elastic structures, Computer Methods in Applied Mechanics and Engineering 148, 367-391.

Raghavan, P., Moorthy, S., Ghosh, S., and Pagano, N. J., 2001. Revisiting the composite laminate problem with an adaptive multi-level computational model. Composites Science and Technology 61, 1017-1040.

Sanchez-Palencia, E., 1980. Non-homogeneous media and vibration theory. Lecture Notes in Physics 127. Springer-Verlag, Berlin.

Seidel, G. D., 2002. A model for predicting the evolution of damage in the plastic bonded explosive LX17. Master’s Thesis, Texas A&M University.

Suquet, P. M., 1987. Elements of homogenization for inelastic solid mechanics. In: Sanchez-Palencia, E., Zaoui, A. (Eds.), Homogenization techniques for composite media, Lecture Notes in Physics 272, Springer-Verlag, Berlin, 193-278.

Tvergaard, V., 1990. Effect of fibre debonding in a whisker-reinforced metal. Materials Science & Engineering A: Structural Materials: Properties, Microstructure, and Processing A125, 203-213.

Williams, J. J., 2002. Two experiments for measuring specific viscoelastic cohesive zone parameters. Master's Thesis, Texas A&M University.

Yi, Y.-M., Park, S.-H., Youn, S.-K., 1998. Asymptotic homogenization of viscoelastic composites with periodic microstructures. International Journal of Solids and Structures 35, 2039-2055.

Yu, Q., Fish, J. 2002. Multiscale asymptotic homogenization for multiphysics problems with multiple spatial and temporal scales: a coupled thermo-viscoelastic example problem. International Journal of Solids and Structures 39, 6429-6452.

Zocher, M. A., Groves, S. E., Allen, D. H., 1997. A three-dimensional finite element formulation for thermoviscoelastic orthotropic media. International Journal for Numerical Methods in Engineering 40, 2267-2288.

APPENDIX A

VISCOELASTIC COHESIVE ZONE MODEL

Although linear elastic fracture mechanics (Griffith, 1920; Irwin 1958) has been enormously successful in predicting the onset of brittle fracture, this success is remarkable in light of the physically unfeasible stress singularity that is inherent to the theory. Efforts have been made to amend this theory in order to make it suitable for the prediction of ductile fracture. These efforts have focused primarily on the removal of the stress singularity through the introduction of a layer, or zone, of cohesive surfaces near the crack tip. Dugdale (1960) and Barenblatt (1962) were among the first to advance this idea more than forty years ago. Since that time numerous cohesive zone models have been developed to address crack growth in a variety of media.

In our multiscale theory, we employ a micromechanically-based viscoelastic cohesive zone model to calculate the opening and advancement of local scale cracks. This cohesive zone model was developed by Allen and Searcy (2000; 2001a; 2001b) and has since been utilized for various applications including plastic bonded explosives (Seidel, 2002) and asphalt-concrete mixtures (Kim, 2003). In this section we provide an overview of this model, highlighting its more important features. The traction-displacement relationship that governs cohesive bonding and decohesion is derived in closed form using a mean-field homogenization approach. No asymptotic expansions are used in this derivation.

A.1 Cohesive Zone Boundary Value Problem

Consider a local scale crack where, near the tip, there exists a region of damaged polymeric material. This damaged region consists of numerous polymeric fibrils that span the gap between the upper and lower crack faces. A damaged region of this type is depicted in Figure A.1a. The fibrils in this region are load bearing and provide resistance to any crack opening displacements. When the applied loading is sufficiently large or sustained, the load bearing characteristics of this region can become severely compromised. Molecular level mechanisms such as reptation, void formation, and polymer chain breakage all contribute to the mechanical failure of this region. Constructing a model that adequately captures these failure characteristics will require a detailed examination of this damaged region. To begin, we extract a representative volume from this fibrillated region. A conceptualized drawing of such a volume is shown in Figure A.1b.

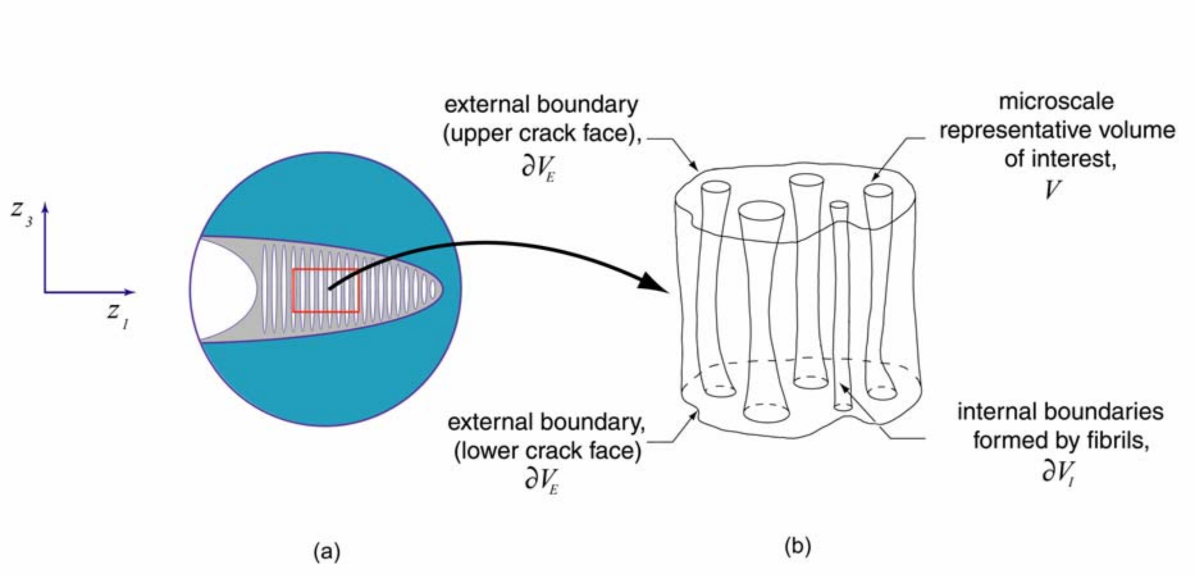

Figure A.1. Local Scale Crack.
(a) Fibrillated Region Ahead of Crack Tip;
(b) Representative Volume from Damaged Region.

The representative body of interest has an interior V, an external boundary ∂V_E, and many internal boundaries ∂V_I. This body is endowed with a three-dimensional orthonormal basis from which the position of each material point z_i may be expressed. The interior may be partitioned into two components: the first represents the volume occupied by the fibrillated material V_{fibril}; and second represents the voided volume which surrounds the fibrils V_{void}. Thus,

$$V = V_{fibril} + V_{void} \tag{A.1}$$

For this cohesive zone model, it is assumed that the voided volume is occupied by a substance which has a negligible effect on the structural stiffness of the microscale body. The set of material points which define the external boundary consists of two separate and distinct subsets: ∂V_{E_u}, which defines that portion of the external boundary where displacements are applied; and ∂V_{E_T}, which defines that portion of the external boundary where tractions are prescribed. In this analysis, ∂V_{E_T} is tractionless. No intersection exists between these two subsets, and the union of ∂V_{E_u} and ∂V_{E_T} defines the external boundary of the global body, ∂V_E.

$$\partial V_E = \partial V_{E_u} + \partial V_{E_T} \tag{A.2}$$

The internal boundaries of the representative volume are defined by the outer surfaces of the fibrils. These internal boundaries ∂V_I are time dependent and assumed to be free from any surface tractions; thus

$$\partial V_I = \partial V_{fibril} \tag{A.3}$$

The variables of state for this analysis are the microscale displacement vector $u_i(\mathbf{z}, t)$, the microscale strain tensor $\varepsilon_{ij}(\mathbf{z}, t)$, and the microscale stress tensor $\sigma_{ij}(\mathbf{z}, t)$.

In the absence of microscale body forces and inertial effects, the conservation of linear momentum for small motions may be expressed by

$$\frac{\partial \sigma_{ji}(\mathbf{z}, t)}{\partial z_j} = 0 \qquad \text{on } V + \partial V_I \tag{A.4}$$

where $\sigma_{ji}(\mathbf{z},t)$ is the microscale Cauchy stress tensor; and z_j is the position vector

Assuming that the materials of interest undergo small displacements, higher order terms in the strain tensor may be neglected. The linearized form of the microscale strain tensor is:

$$\varepsilon_{ij}(\mathbf{z},t) = \frac{1}{2}\left(\frac{\partial u_i(\mathbf{z},t)}{\partial z_j} + \frac{\partial u_j(\mathbf{z},t)}{\partial z_i}\right) \qquad \text{on } V + \partial V_I \qquad (A.5)$$

where the microscale strain tensor is also symmetric.

In addition to conservation laws and kinematic constraints, constitutive equations are needed to characterize the stress-strain relationship of the body. These constitutive equations must reflect the strain history dependence of the fibrils. To address these needs, we pose the following set of stress-strain relations:

$$\sigma_{ij}(\mathbf{z},t) = \int_0^t C_{ijkl}(\mathbf{z},t-\tau)\frac{\partial \varepsilon_{km}(\mathbf{z},t)}{\partial \tau}d\tau \qquad \text{on } V + \partial V_I \qquad (A.6)$$

These equations feature a linear hereditary-type integral which captures the strain history dependence of the viscoelastic medium. In this integral C_{ijkl} represents the stress relaxation modulus tensor on the microscale, t is the time of interest, and τ is the variable of integration. Displacements, which are specified on the upper and lower surfaces of the microscale body, are given by

$$u_i(\mathbf{z},t) = \hat{u}_i(\mathbf{z},t) \qquad \text{on } \partial V_{E_u} \qquad (A.7)$$

where $\hat{u}_i(\mathbf{z},t)$ represent imposed displacement values.

The remaining sides of the external boundary represent ∂V_{E_T} which are assumed to be traction-free. Thus,

$$T_i\left(\mathbf{z},t\right) = \hat{T}_i\left(\mathbf{z},t\right) = 0 \qquad \text{on } \partial V_{E_T} \tag{A.8}$$

The initial values for all the state variables are assumed to be zero.

With relationships (A.4) through (A.8), the microscale boundary value problem is considered to be well-posed. Unfortunately, the geometric complexity of the fibrils, as shown in Figure A.1b, makes it difficult to solve this problem in closed form. To remedy this difficulty, the representative volume has been idealized in the manner shown in Figure A.2. In this figure, the fibrils are represented by right circular cylinders which exhibit the same linear viscoelastic properties as that of the surrounding bulk material. Furthermore, the fibrils are assumed only to carry spatially homogeneous uniaxial loads.

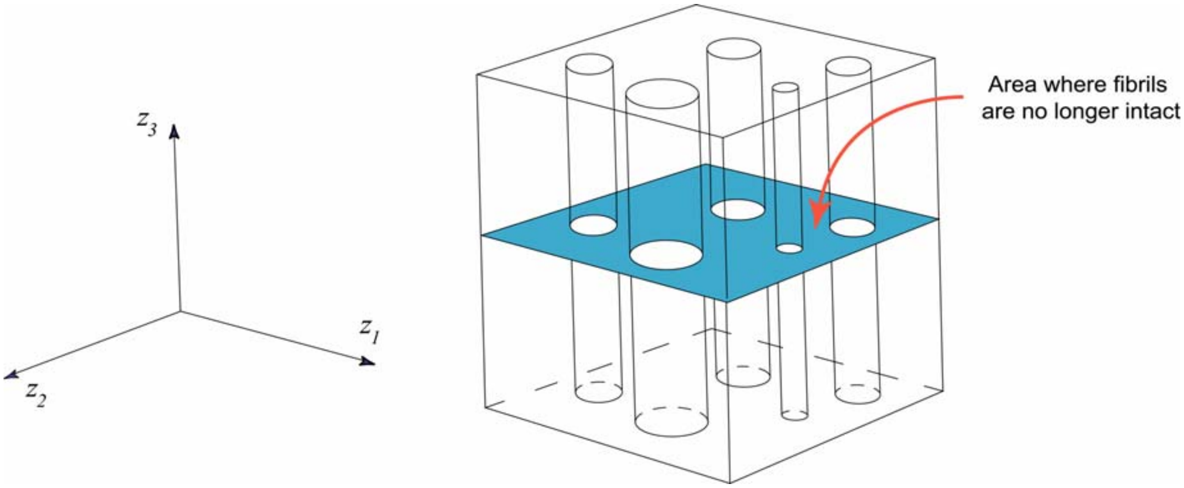

Figure A.2 Idealized Representative Volume from the Damage Zone.

With this idealized geometry, the above boundary value problem can be solved in closed form. This problem is statically determinate for the case of imposed boundary displacements. In the limit as the representative volume's height approaches zero, we achieve our cohesive surface. The resulting homogenized traction-displacement relation given by the following:

$$T_i\left(\mathbf{z},t\right)=\frac{\left[u_i\left(\mathbf{z},t\right)\right]}{\delta_i\lambda\left(\mathbf{z},t\right)}\left(1-\alpha\left(\mathbf{z},t\right)\right)\int_0^t E^{cz}\left(\mathbf{z},t-\tau\right)\frac{\partial\lambda\left(\mathbf{z},\tau\right)}{\partial\tau}d\tau \tag{A.9}$$

where $\alpha\left(\mathbf{z},t\right)$ is a damage parameter that is equivalent to the cross-section of voided material divided by the total cross-sectional area, as indicated by the shaded region in Figure A.2; $E^{cz}\left(\mathbf{z},t\right)$ is the uniaxial relaxation modulus of the fibrils; and $\lambda\left(\mathbf{z},t\right)$ is the Euclidean norm of the damaged zone opening displacements as given by

$$\lambda\left(\mathbf{z},t\right)=\left[\left(\frac{\left[u_1\left(\mathbf{z},t\right)\right]}{\delta_1}\right)^2+\left(\frac{\left[u_2\left(\mathbf{z},t\right)\right]}{\delta_2}\right)^2+\left(\frac{\left[u_3\left(\mathbf{z},t\right)\right]}{\delta_3}\right)^2\right]^{\frac{1}{2}} \tag{A.10}$$

where the bracketed terms are the jump displacements across the crack faces, and δ_1, δ_2, and δ_3 are empirical material length parameters that typically reflect the dimensions of the damaged zone.

In its initial state, the cohesive zone is undamaged, and $\alpha\left(\mathbf{z},0\right)=0$. However, as the load increases, damage begins to accumulate inside the cohesive zone. Ultimately, at some critical time t_{cr} damage will have reached its maximal value: $\alpha\left(\mathbf{z},t_{cr}\right)=1$. At this critical time, the cohesive traction will be zero, and the crack tip will advance.

A.2 Cohesive Zone Damage Evolution Law

Equation (A.9) represents the constitutive behavior of a homogenized damage zone in which there are no longer any internal boundaries. The dissipation due to microstructural damage evolution is retained in the form of the damage parameter, $\alpha\left(\mathbf{z}, t\right)$. This damage parameter must be modeled by an ancillary constitutive equation. Although original efforts to model this equation have relied solely on phenomenology, we have chosen to take a micromechanical approach. This approach will require us to perform microscale experiments on the damaged material to determine details regarding the fibril strength and morphological charcateristics within the representative volume.

To construct a general form of the damage evolution law, we first assume that within the representative volume that the *p*th fibril fractures when its radius $r_p^f\left(\mathbf{z},t\right)$ reaches a critical value, r_{cr}^f, i.e.,

$$r_p^f\left(\mathbf{z}, t\right) \le r_{cr}^f \qquad \text{where } r_{cr}^f = constant \tag{A.11}$$

Furthermore, it is assumed that the Poisson's ratio for the fibrils is time independent. This is a fairly accurate approximation for some viscoelastic materials (Schapery, 1962). Thus, the radius of the *p*th fibril evolves according to the following relationship

$$r_p^f\left(\mathbf{z}, t\right) \cong r_p^f\left(\mathbf{z}, 0\right)\cdot\left(1-\nu\,\lambda\left(\mathbf{z}, t\right)\right) \tag{A.12}$$

where ν is the Poisson's ratio, and $r_p^f\left(\mathbf{z}, 0\right)$ is the initial radius of the *p*th fibril. Finally, it is assumed that the distribution of fibril radii within the damaged zone, $r_p^f\left(\mathbf{z}, t\right)$, is governed by a Gaussian distribution function given by the following:

$$f\left(m(t),s\right)=\frac{1}{s\sqrt{2\pi}}\exp\left(\frac{-\left(r^{f}-m(t)\right)^{2}}{2s^{2}}\right) \tag{A.13}$$

where $m(t)$ is mean fibril radius for the representative volume and s is the standard deviation for the fibril distribution. Although both the mean and standard deviation could potentially be time-varying, for this model only the mean fibril radius is time dependent. A graphical depiction of the normalized fibril distribution used in this study is offered in Figure A.4. The total area under the curve is unity. The area under the curve and to the left of the critical fibril radius represents the measure of fibril breakage within the damage zone. This area corresponds with the shaded region depicted in Figure A.2. The resulting expression for the damage parameter $\alpha(\mathbf{z},t)$ is

$$\alpha(\mathbf{z},t)=1-\int_{r_{cr}^{f}}^{\infty} f\left(m(t),s\right)\,dr \tag{A.14}$$

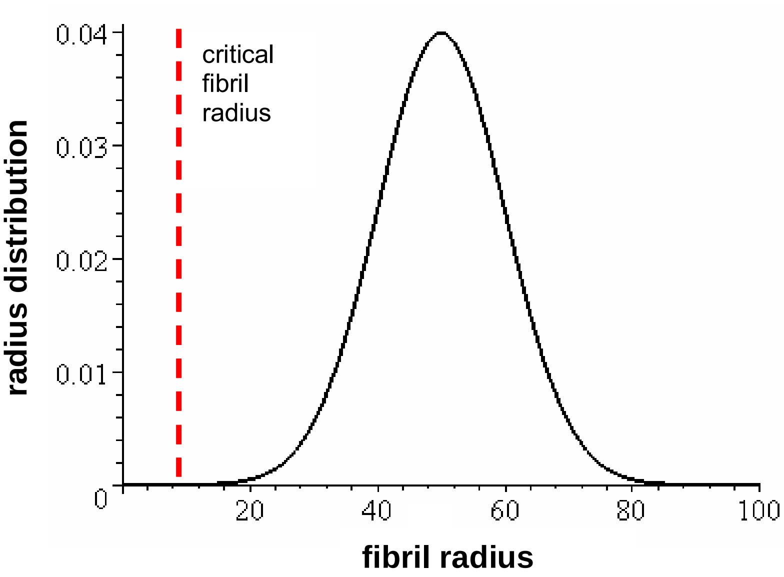

Figure A.3. Normalized Gaussian Distribution of Fibril Radii.

Mean fibril damage is assumed to evolve according to Poisson effects. Thus,

$$m(t) = m(0) \cdot \left(1 - \nu\,\lambda(\mathbf{z}, t)\right) \tag{A.15}$$

where $m(0)$ is the mean fibril radius at $t = 0$; ν is the Poisson's ratio, and $\lambda(\mathbf{z}, t)$ is the aforementioned Euclidian norm of the opening displacements. Restrictions have been placed on (A.15) to prevent the possibility of crack healing.

Numerical simulations of this model were performed for a single material point within the cohesive zone. A ramp displacement was imposed where *c* is the constant-valued crack opening displacement rate. Assuming all other parameters are equal, the damage accumulation for three different rates of loading is shown in Figure A.4. The figure demonstrates the direct relationship between loading rate and damage evolution rate: as the rate of loading increases, so does the rate of damage.

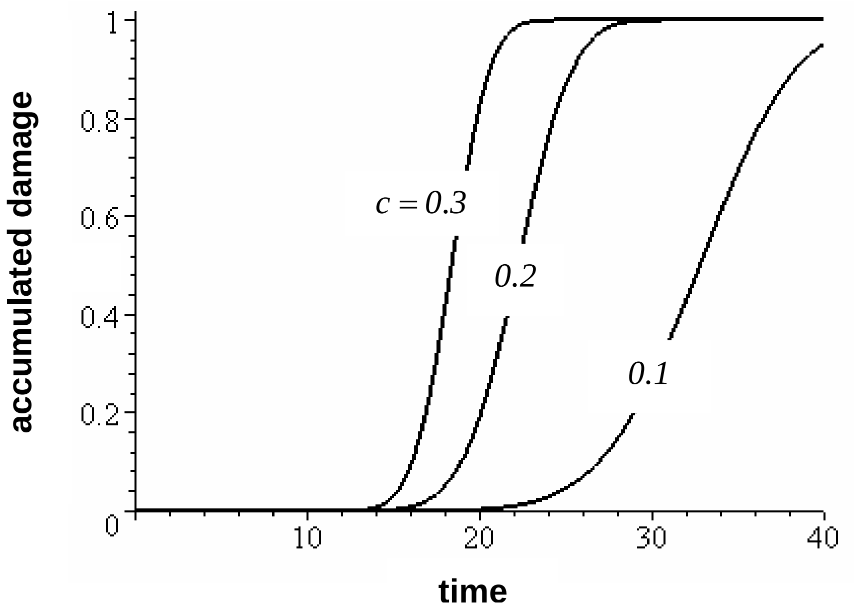

Figure A.4. Accumulated Damage vs. Time for Cohesive Zone Model.

The corresponding traction-displacement curves are shown in Figure A.5. In each of the three cases, the cohesive tractions begin to grow unimpeded by damage. Any initial strain-softening is the result of viscoelastic relaxation. However, once enough damage accumulates, and the cohesive traction quickly decays.

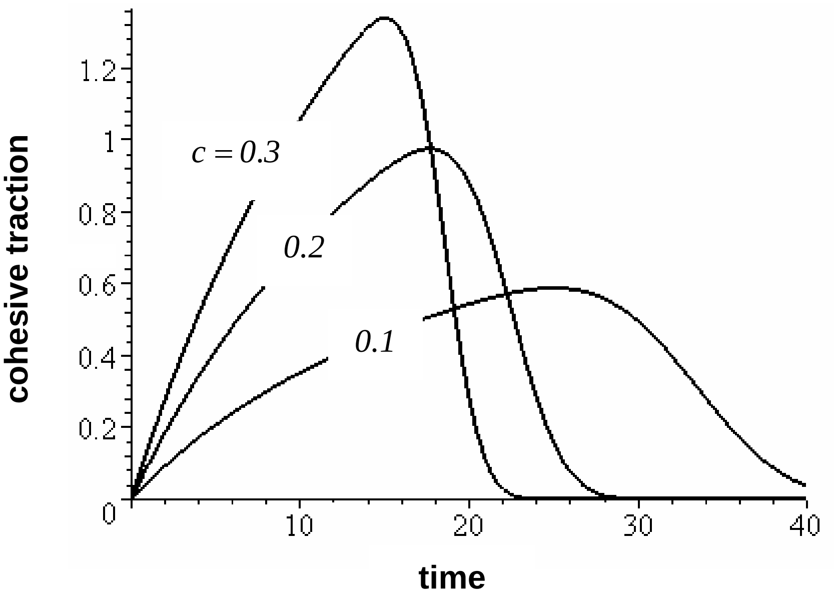

Figure A.5. Cohesive Traction vs. Time for Cohesive Zone Model.

The traction-displacement law (A.9) has been discretized by Allen and Searcy (2000) and implemented into the multiscale finite element program according to the procedure developed by Foulk, et al. (2000).

VITA

Chad Randall Searcy was born in Garland, Texas, on March 22, 1972. He received his B.S. in engineering from Baylor University in 1995. He enrolled in the graduate program in aerospace engineering at Texas A&M University in the fall of 1995 and studied under the direction of Dr. David H. Allen. He received an M.S. degree in aerospace engineering in December 1998. He earned his Ph.D. in aerospace engineering from Texas A&M University in August 2004. His research interests include multiscale modeling, fracture mechanics, and viscoelasticity.

Mr. Searcy can be reached at his permanent address: 2620 Rolling Meadows Dr., Rockwall, TX 75087.